MODELING GUIDED HEAT PIPE DESIGN METHODOLOGY AND
EXPERIMENTAL VALIDATION FOR FLAT GROOVED HEAT PIPES

A THESIS SUBMITTED TO
THE GRADUATE SCHOOL OF NATURAL AND APPLIED SCIENCES
OF
MIDDLE EAST TECHNICAL UNIVERSITY

BY

SAMET SAYGAN

IN PARTIAL FULFILLMENT OF THE REQUIREMENTS
FOR
THE DEGREE OF DOCTOR OF PHILOSOPHY
IN
MECHANICAL ENGINEERING

FEBRUARY 2021

Approval of the thesis:

MODELING GUIDED HEAT PIPE DESIGN METHODOLOGY AND EXPERIMENTAL VALIDATION FOR FLAT GROOVED HEAT PIPES

submitted by **SAMET SAYGAN** in partial fulfillment of the requirements for the degree of **Doctor of Philosophy in Mechanical Engineering Department, Middle East Technical University** by,

Prof. Dr. Halil Kalıpçılar
Dean, Graduate School of **Natural and Applied Sciences** _____

Prof. Dr. M. A. Sahir Arıkan
Head of Department, **Mechanical Engineering** _____

Prof. Dr. Zafer Dursunkaya
Supervisor, **Mechanical Engineering, METU** _____

Assoc. Prof. Dr. Barbaros Çetin
Co-supervisor, **Mech. Eng., Bilkent University** _____

Examining Committee Members:

Prof. Dr. İlker Tarı
Mechanical Engineering Dept., METU _____

Prof. Dr. Zafer Dursunkaya
Mechanical Engineering Dept., METU _____

Prof. Dr. Almıla Güvenç Yazıcıoğlu
Mechanical Engineering Dept., METU _____

Prof. Dr. Selin Aradağ Çelebioğlu
Mechanical Engineering Dept., TED University _____

Assoc. Prof. Dr. Özgür Ekici
Mechanical Engineering Dept., Hacettepe University _____

Date:

I hereby declare that all information in this document has been obtained and presented in accordance with academic rules and ethical conduct. I also declare that, as required by these rules and conduct, I have fully cited and referenced all material and results that are not original to this work.

Name, Surname: Samet Saygan

Signature   :

ABSTRACT

MODELING GUIDED HEAT PIPE DESIGN METHODOLOGY AND EXPERIMENTAL VALIDATION FOR FLAT GROOVED HEAT PIPES

Saygan, Samet

Ph.D., Department of Mechanical Engineering

Supervisor: Prof. Dr. Zafer Dursunkaya

Co-Supervisor: Assoc. Prof. Dr. Barbaros Çetin

February 2021, 129 pages

Heat pipes are commonly preferred thermal management devices due to their rapid heat transfer characteristics, small size and reliability. It is crucial to design heat pipes that accurately match the requirements of the system to be thermally managed. In the present study, a numerical design and diagnosis simulation tool for heat pipes is developed and verified for grooved heat pipes. A modular heat pipe experimental setup is designed and manufactured. In order to decide on the geometric parameters of the heat pipe to be tested, the setup is designed by the newly developed simulation tool. Predictions of the tool are validated by both the studies existing in the literature and the experiments conducted in the scope of this thesis. Finally, an innovative groove structure, namely *Hierarchical Groove Architecture*, is proposed for boosting the capillary pumping and improving evaporation performance, two functions the enhancement of which are important in operating heat pipes with higher performance. The simulations for proving these improvements are modeled and run and the boosting of the capillary pumping is validated with the experiments.

The design and diagnosis tool for heat pipes developed in the scope of this thesis will allow researchers/designers to simulate the performance of grooved heat pipes rapidly and accurately and utilization of hierarchical groove architecture will improve both capillary pumping and evaporation performance of heat pipes.

Keywords: Heat pipe modeling, modular experimental design, grooved heat pipe, capillary pumping and evaporation enhancement, hierarchical groove architecture

ÖZ

MODELLEME İLE YÖNLENDİRİLEN ISI BORUSU TASARIM METODOLOJİSİ VE DÜZ OLUKLU ISI BORULARI İÇİN DENEYSEL DOĞRULANMASI

Saygan, Samet

Doktora, Makina Mühendisliği Bölümü

Tez Yöneticisi: Prof. Dr. Zafer Dursunkaya

Ortak Tez Yöneticisi: Doç. Dr. Barbaros Çetin

Şubat 2021 , 129 sayfa

Isı boruları hızlı ısı transferi karakteristikleri, küçük boyutları ve güvenilirlikleri nedeniyle sıklıkla tercih edilen ısıl yönetim araçlarıdır. Isıl yönetim gereksinimi olan sistemde kullanılacak ısı borusunun tasarımının doğruluğu hayati önem taşır. Bu çalışmada, ısı boruları için sayısal bir tasarım ve teşhis simülasyon aracı oluklu ısı boruları için geliştirilmiş ve doğrulanmıştır. Bu tez kapsamında, modüler bir ısı borusu deney düzeneği tasarlanmış ve üretilmiştir. Bu deney düzeneğinde test edilecek ısı borusunun geometrik parametrelerine karar vermek için ise yeni geliştirilen tasarım ve teşhis aracı kullanılmıştır. Bu araç kullanılarak yapılan benzetimlemelerin sonuçları hem literatürde bulunan çalışmaların hem de bu tez kapsamında yapılan deneylerin sonuçları ile doğrulanmıştır. Son olarak *Hiyerarşik Oluk Mimarisi* olarak adlandırılan yeni bir oluk yapısı, kılcal pompalama gücünü ve buharlaştırmayı arttırmak amaçlarıyla ısı borusu performansını geliştirmek için önerilmiştir. Hedeflenen her iki gelişimi de kanıtlamak için analizler yapılmıştır ve beklenen gelişim analiz sonuçları tarafından desteklenmiştir.

Kılcal pompalama gücünün artışı, simülasyon sonuçlarının yanı sıra deneysel olarak da bu tez kapsamında kanıtlanmıştır. Bu çalışma kapsamında ısı boruları için geliştirilen analitik tasarım ve teşhis aracından yararlanarak, araştırmacı/-tasarımcıların oluklu ısı borularını hızlı ve doğru bir şekilde benzetimlemelerini sağlayacaktır. Ek olarak, hiyerarşik oluk mimarisi, hem kılcal pompalama hem de buharlaşma açısından ısı borusunun performansını artıracaktır.

Anahtar Kelimeler: Isı borusu modellemesi, modüler deney tasarımı, oluklu ısı boruları, kapiler pompalama ve buharlaştırma iyileştirmesi, hiyerarşik oluk mimarisi

To my wife...

ACKNOWLEDGMENTS

TABLE OF CONTENTS

LIST OF TABLES

TABLES

LIST OF FIGURES

FIGURES

xvii

xviii

LIST OF ABBREVIATIONS

ABBREVIATIONS

g	Gravity, m/s^2
$\mathbb{G}(z)$	Geometric Function
h	Height, m
h_{fg}	Latent heat of evaporation, J/kg
k	Thermal conductivity, W/m $\cdot$ K
L	Length, m
M	Molar mass of liquid, kg/mol
$\dot{m}$	Mass flow rate, kg/s
P	Pressure, Pa
$\dot{q}$	Heat transfer rate, W
r	Meniscus radius of curvature, m
R	Thermal resistance, K/W
R_u	Universal gas constant, J/mol $\cdot$ K
T	Temperature, K
U	Velocity, m/s
V	Volume, m^3
w	Width, m

Greek Symbols

$\widehat{\sigma}$	Accommodation coefficient
δ	Liquid film thickness, m
ϵ	Convergence criterion
μ	Dynamic viscosity, Pa $\cdot$ s

ν	Kinematic viscosity, m^2/s
ρ	Density, kg/m^3
σ	Surface tension, N/m
Δ	Delta
θ	Liquid/solid contact angle, radian
ψ	Filling Ratio

Subscripts

a	Adiabatic
ax	Axial
b	Base
c	Condenser
$cond$	Conduction
e	Evaporation
f	Fin
ft	Fin top
g	Groove
gf	Groove film
l	Liquid
m	Mean
$p.c.$	Phase change
s	Solid
tf	Thin film
tot	Total
v	Vapor

Superscript

a	Adiabatic
c	Condenser
$conv$	Convective
e	Evaporator
eff	Effective

CHAPTER 1

INTRODUCTION

The density and number of transistors inside the microchips have been increasing rapidly over the years. Gordon E. Moore, co-founder of Intel, had foreseen that the number of components inside the chip would double in every two years. The number of components, which was 20 in 1962, was 60 by 1965 [1]. Today, the number of transistors inside the microchips reaches 11.8 billion. With the increase of transistors in microchips and their shrinkage, the problem of cooling of high heat fluxes has arisen. For example, the heat loads encountered in 2007 were in the order of 300 W/cm^2 and maximum temperature had to be kept below 85°C [2]. Therefore, for electronics, thermal management is vital for reliable and long-lasting devices' design without any performance degradation. In addition to secure operation of electronic devices, modern chip technology is limited by the heat removal rate from electronic components because of their high heat dissipation.

Several cooling mechanisms have been implemented, for example free convection of gases and liquids, forced convection of gases and liquids, liquid evaporation, which are traditional cooling techniques, and there are also emerging cooling devices to remove excess heat from the heat source such as, heat pipes, heat pumps, microchannels, spray cooling, and phase change materials. Specifically, in cooling by natural convection using air, the heat transfer coefficient varies between 5 W/m$^2 \cdot$ K and 10 W/m$^2 \cdot$ K but in the case of water, it goes up to 1,200 W/m$^2 \cdot$ K. On the other hand, in forced convection, the heat transfer coefficient is between 10 W/m$^2 \cdot$ K and 350 W/m$^2 \cdot$ K for air and reaches 3,000 W/m$^2 \cdot$ K when water is employed. In fact, when water evaporation is

utilized as a cooling method, this value goes above 3,000 W/m² · K and reaches up to 100,000 W/m² · K [3]. However, traditional cooling techniques are insufficient for modern chips due to low heat transfer coefficients. Instead, heat pipes appear as an advantageous alternative and have been used in both terrestrial and space applications [4, 5] for more than 50 years [6].

Heat pipes are sealed containers and transport heat from a hot source to a cold exterior rapidly with small temperature differences between the two ends. With the heat coming from an external heat source, the liquid in the heat pipe evaporates and transforms into gas phase. The region where evaporation occurs is called the evaporator. Vapor moves along the heat pipe and comes to the region where temperature is low, and then releases its thermal energy and transforms back to the liquid phase. The phase change occurs in the region named the condenser. In addition, the adiabatic region is the area between the evaporator and condenser where no or little heat transfer with the environment occurs, but it may not be present in all applications. The condensed liquid, on the other hand, comes back to the evaporator region owing to the capillary action created by the wick structures on the heat pipe walls, and this cycle continues as long as there is a temperature difference between the two ends of the heat pipe. The working principle of a heat pipe is given in Figure 1.1.
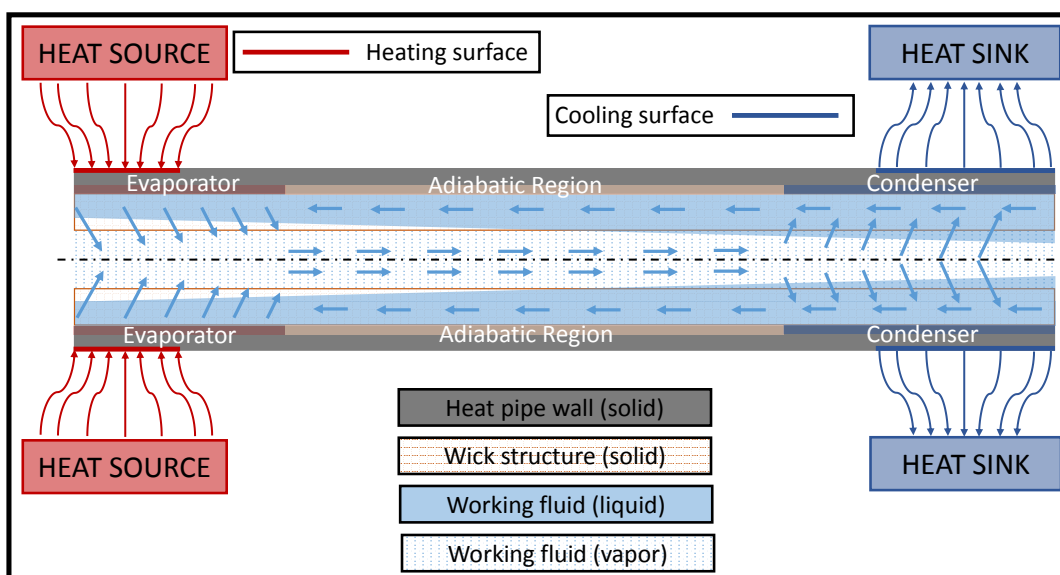
Figure 1.1: Heat pipe working principle

The purpose of the wick structure is to provide liquid to flow without any external force such as gravity or a mechanical pump. Therefore, heat pipes are passive and reliable devices. The most common wick structures used in heat pipes can be listed as follows: groove, sinter, and mesh (Figure 1.2). The decision for which wick structure will be chosen is made according to the application of the heat pipe. For instance, sintered wick provides higher thermal conductivity and works against gravity; nevertheless, pressure drop is higher, and permeability is lower in sintered wicks compared to grooved and mesh wicks. On the other hand, although permeability is high for grooved wicks, they are not preferable in conditions operating against gravity and have relatively low capillary pumping. Finally, although the mesh wick structure has a moderate capillary action, it is suitable for complex geometries [5, 7–9].
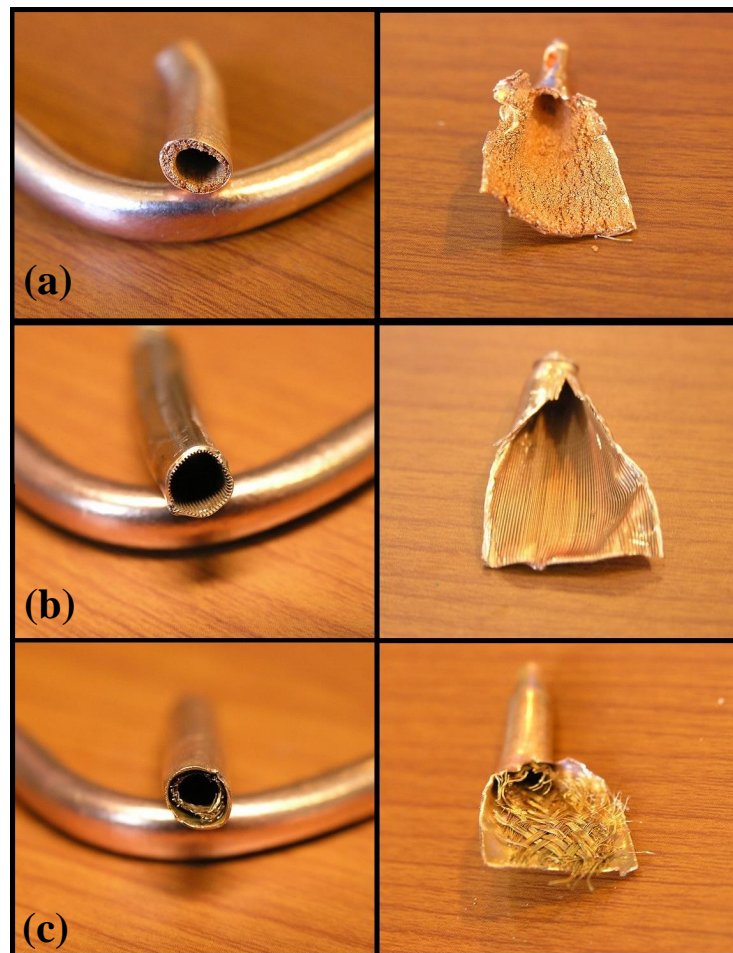
Figure 1.2: Wick structure types: **(a)** sintered **(b)** grooved **(c)** mesh screen [10]

3

Moreover, working fluid and wall material are important design parameters that affect the performance of the heat pipe in terms of its operating temperature, transferred heat flux and dimensions. The compatibility of the working fluid with the wall material at the operating temperature is especially important for obtaining a high-performance heat pipe and there are many of studies in the literature on this issue as listed below:

- Methane and stainless steel at -140°C [11]
- Ammonia and aluminum at 25°C [12]
- Copper and water
    - at 50°C ([13])
    - between 50°C and 80°C [14]
    - between 60°C and 95°C [15]
    - at 75°C [16]
    - around 100°C [17–20]
    - at 160°C [21]
- stainless steel and Therminol VP-1 between 300°C and 400°C [22]
- Stainless steel and sodium
    - between 430°C and 790°C [23]
    - at 650°C [24]
    - at 800°C [25]
- Stainless steel and mercury at 630°C [26]
- Stainless steel and NaK (with Argon as NCG) at 700°C [27]
- Molybdenum and lithium at 1227°C [28].

There are several types of heat pipes that are used in industry. One of the most common heat pipes is the conventional *capillary driven heat pipe* as shown in Figure 1.3. These type of heat pipes are generally cylinder in shape. Working fluid evaporates in the evaporator and the vapor flows through the condenser to condense there. Capillary limit, which will be explained in the following sections, is the most critical limitation of these type of heat pipes.
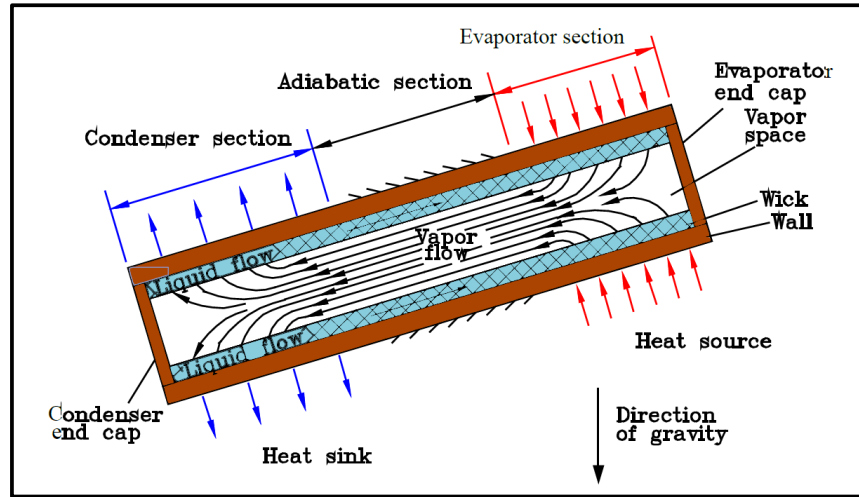
Figure 1.3: Capillary driven heat pipe [8]

The second type of heat pipe is the *loop heat pipe*. Schematic representation of the loop heat pipe is shown in Figure 1.4. This type of heat pipe is used when the distance between the heat source and the heat sink is long. In addition, loop heat pipes can work against gravity. The vapor pipe and the liquid pipe which are included in the loop heat pipe are different from each other (Figure 1.4). This is one of the major differences between the loop and capillary driven heat pipes. Another important difference between them is the compensation chamber, which cannot exist in conventional capillary heat pipes, but provides liquid reservoir to loop heat pipes.
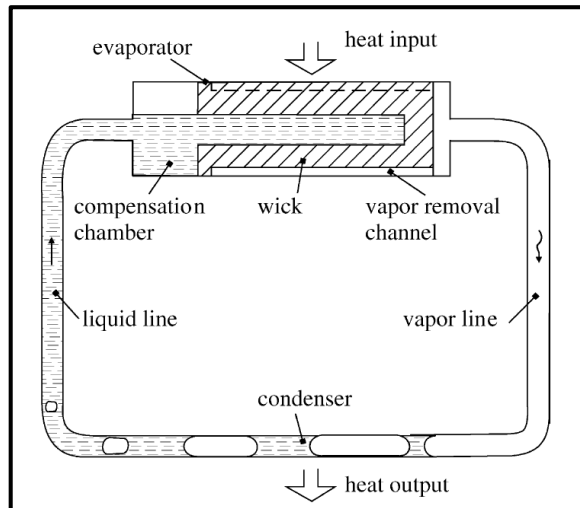
Figure 1.4: Working principle of loop heat pipe ([29])

5

The third type of the heat pipe is the *flat heat pipe*. The cross-section of the flat heat pipe is rectangular unlike the cylinder-shaped capillary driven heat pipe (see Figure 1.5). However, these two heat pipes have the same wick structures and working principle. In addition, it was reported that the thermal and hydrodynamic performance of the flat heat pipe increases under the high heat loads [30].
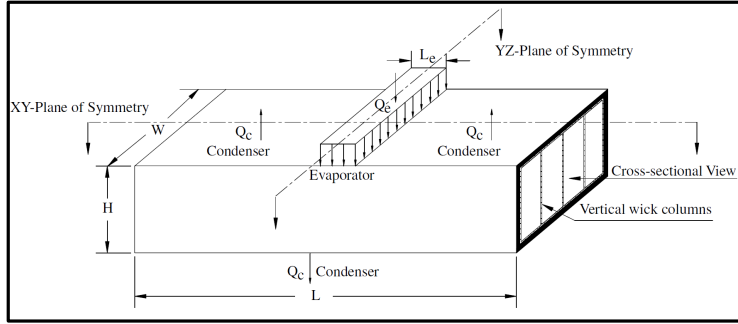
Figure 1.5: Flat heat pipe [30]

The last heat pipe type is the *micro heat pipe*. Different from both capillary driven heat pipes and flat heat pipes, micro heat pipes have only one non-circular channel (see Figure 1.6). Micro heat pipe, which was initially introduced by Cotter in [31], works on triangular cross-section. Additionally, the sharp corners of the micro heat pipe creates a capillary force which provides the liquid flow.
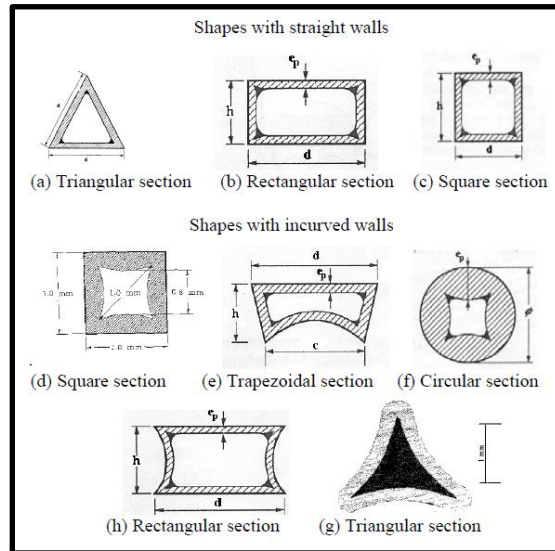
Figure 1.6: Micro groove cross-section types [32]

6

In a heat pipe, design parameters such as shape, size, working fluid, wick structure, and operating temperature affect the heat pipe thermal and hydraulic performance. In addition to these parameters, there are some physical phenomena that affect the heat transfer rate in the heat pipe, namely capillary, boiling, entrainment, condenser, vapor pressure, and sonic limits, which will be explained in the following paragraphs.

- Capillary pressure, which is created due to the wick structure, provides liquid flow from the condenser region to the evaporator region. If the total pressure drop along the heat pipe is higher than the capillary pressure difference along the heat pipe, the liquid flow from the condenser region to the evaporator region becomes insufficient. It causes dryout of the heat pipe. This phenomenon is called capillary limit.

- At the beginning of this section, the working principle of the capillary driven heat pipe was reviewed. The liquid evaporates due to the heat input from the heat source(s) at the evaporator region. If the heat input is large enough to cause nucleate boiling, then the liquid flow is blocked and dryout occurs. This phenomenon is called the boiling limit.

- Heat pipes are two-phase heat spreaders and contain both liquid and vapor flows inside (see Figure 1.1). Therefore, shear occurs between liquid and vapor interface. When shear increases, vapor entrains liquid droplets from the wick structure and carries them to the condenser without any evaporation at the evaporator region. It causes lack of liquid in the evaporator region and dryout occurs. This phenomenon is called the entrainment limit.

- In order for the heat pipe to work effectively, heat transferred to the condenser region must be removed quickly from the system. Therefore, a proper cooling is required at the condenser. If the cooling ability of the heat sink is not enough to remove the heat input at the evaporator region, then the capacity of the heat pipe decreases. This phenomenon is called the condenser limit.

- If the heat pipe operates at temperatures lower than its normal working temperature, then the effect of viscous forces may become stronger restricting vapor flow. This phenomenon also causes a capacity reduction of the heat pipe, and is called the vapor pressure limit or viscous limit.

- Finally, if the velocity of the vapor reaches the sonic speed, then a choked flow condition occurs in the vapor flow region due to the supersonic flow. This situation results in a temperature drop in the axial direction of the heat pipe. Therefore, isothermal condition of the heat pipe cannot be established under the choked flow condition. This phenomenon is called the sonic limit.

1.1 Literature Review

One of the most important parameters determining the capacity of energy transfer *via* phase change of a heat pipe is the wick structure. Therefore, ensuring the maximum mass transfer throughout the wick structure plays a critical role in heat pipe design. A flow model predicts the performance of the wick structure and requires a complex solution of the nonlinear flow equations. In addition to the flow model, a heat transfer model is also needed to find the temperature distribution. In cases where complex modeling is required, making use of simplifying assumptions is inevitable. Over the years, researchers have proposed different strategies of modeling heat pipes for both porous and grooved wick structures. In addition to modeling, experiments for different wick structures guided researchers in the characterization of heat pipes. In this part of the current study, both numerical and experimental studies in the literature will be presented under three sections. Specifically, modeling of porous and grooved wick structures will be explained in the first and second sections, respectively. Finally, experimental studies will be introduced in the third section.

1.1.1 Modeling of porous wick structured heat pipes

In case of a porous wick, two common approaches were studied for flow model in the literature. One of them is solving the flow by applying Darcy's law [33–37]. However, applying Darcy's law neglects the effects of the boundary, inertial, and variable porosity [38]. Another common approach that considers boundary and inertial effects is solving the conservation of mass and momentum equations in the flow region [30, 39–44]. Apart from these two approaches, another modeling method that is less frequently encountered in the literature is the application of the lattice Boltzman method [45].

In the modeling of heat transfer, solving energy conservation equation [30, 34, 35, 42–44] or establishing a thermal resistance network [36, 37, 40, 46, 47] are common approaches in the literature.

A flat plate heat pipe with asymmetric heating (in which the heater was placed at the center of the top surface) was analyzed by Vafai and Wang [33] in 1992. Darcy's law and a pseudo-three dimensional approach were applied for fluid and vapor flows, respectively. The authors reported that the velocity distribution of the steam was not symmetrical in the regions close to the heater, but started to become symmetrical away from the heater. The same heat pipe configuration was analyzed in [40]; but, three-dimensional, steady, incompressible, and laminar flow was assumed for both liquid and vapor flow. The results showed that vapor velocity distributions were similar in [33] and [40].

Wang and Vafai [48] took modeling one step further by adding the effect of conduction heat transfer in the solid to the same geometry [33, 40]. Transient behavior of the heat pipe was investigated during startup and shutdown. The results indicated that the effect of the heat transfer coefficient on the time constant of the heat pipe is significant, which directly affects the duration to reach steady state. In addition, it was found that the temperature variation through the walls is small, and the major part of the total thermal resistance is due to the evaporator and condenser regions.

A complete solution of the vapor, the wick, and the solid regions was investi-

gated by Xiao and Faghri [30] for the same flat plate heat pipe in [33, 40, 48] solving three-dimensional conservation equations for both fluid and vapor flow without using empirical relations. In addition, three-dimensional heat conduction equation was solved in the wall, the fluid flow region, and the porous wick structure. Moreover, liquid-vapor interface was modeled with a coupled solution of heat and mass transfer. As a result, the model was capable of finding capillary limit and thermal resistance of the heat pipe, and it was reported that higher heat input resulted in higher surface temperatures, pressure drop, and fluid velocities.

Flat plate heat pipe with different heating and cooling regions or configurations was studied in [34, 35]. Liquid flow was modeled with Darcy's law, and temperature distribution in the solid was calculated with conduction equation in both studies. Vapor flow was modeled with assuming analytical solution of parallel flow between the plates and a parabolic velocity profile in [34] and [35], respectively. Lefèvre and Lallemand [34] simulated the experimental study of [49] in terms of maximum heat transport capability, and the results were close to each other. After the model was verified, a heat pipe with multiple heat sources and sinks was modeled; and, temperature and liquid/vapor velocity distributions were reported. Aghvami and Faghri [35] validated their model with the heat pipe experiments conducted in [50] with a good agreement, and also repeated simulations for different heating and cooling configurations. It was reported that the smaller the heat source size, the lower the performance of the heat pipe because of high temperatures occur in the heat pipe wall.

Sonan et al. [42] combined coupled transient two-dimensional flow model with the transient three-dimensional thermal model to solve flat plate heat pipe with multiple heating and cooling regions, and compared their results with that of [34]. Similar results were obtained, and transient behavior of electronic components' temperatures, vapor/liquid pressure distributions, maximum vapor velocity, and vapor/liquid velocity fields were reported.

In case of cylindrical heat pipes, Zhu and Vafai [41] assumed parabolic velocity profiles for flow model and solved energy equation for vapor and wall temper-

atures including effects of both non-Darcian transport and liquid-vapor interfacial hydrodynamic coupling. The results were validated with [51] for both vapor and wall temperatures found experimentally and [52] for calculated pressures. Authors reported that interfacial shear effects can be ignored because of its negligible results.

Ferrandi et al. [36] modeled a cylindrical heat pipe by assuming Darcy's law for liquid flow and defining vapor with ideal gas equations. Both liquid and vapor flows were assumed laminar along the heat pipe, and fluidic electrical scheme was introduced. Kolliyil et al. [37] conducted a similar modeling approach for the similar heat pipe in [36]; but additionally, Marangoni effect (i.e., mass transfer of fluid motion due to the gradient of surface tension) was included into the model. Both [36] and [37] were verified with both experimental [51] and numerical [52] results in the literature. Ferrandi et al. [36] reported that wick thickness can be optimized in which it minimizes the temperature variation along the heat pipe. Yet, no connection was found between the optimum wick thickness and the amount of heat input. In addition, relation between the heat pipe diameter and heating power limit was studied and it was found that there is a direct relation between them. Moreover, it was seen that although the grain radius had no effect on the thermal resistance, it affected the working limit of the heat pipe by affecting the dryout at the same wick thickness. Kolliyil et al. [37] also reported the same conclusions with [36] that larger diameter heat pipes resulted in higher heat carrying capacity without occurring dryout, and there should be an optimum wick thickness that minimizes the thermal resistance. In addition, it was stated that as heat input increases, thermal resistance decreases up to a limit, after which an excessive amount of heat input causes nucleate boiling that decreases the thermal performance of the heat pipe.

Liquid/vapor regions, wick structure, and the heat pipe wall were modeled using two-dimensional conservation equations in [43, 44]. ANSYS-Floatran software and standard Galerkin method were applied to solve conservation equations in relevant regions in [43] and [44], respectively. Elnaggar et al. [43] validated the model with their own experiments. On the other hand, Thuchayapong et al. [44] compared their results with the available experimental [51] and numerical [52]

results in the literature. Findings of both studies showed that the vapor pressure remained constant along the heat pipe. In addition, it was reported that liquid velocity varied linearly in the condenser and the evaporator regions, and remained constant in the adiabatic region [43].

Another approach for modeling heat pipes is establishing a thermal resistance network [47, 53] or thermal resistance-capacitance network [46] without solving the fluid flow. System analysis theories and capacitance definitions were applied to model to simulate the transient behavior in [53] and [46], respectively. Unlike [47, 53], Gholami et al. [46] modeled multiple heat sources and heat sinks similar with [34]. Zuo and Faghri [53] validated the model with the experimental results of [18], whereas [46, 47] validated it by conducting their own experiments. The results showed that the heat pipe can be modeled simply by using thermal network approach. However, heat carrying capacity could not be determined in [46, 47, 53] due to lack of fluid model.

The only coupled thermal and flow modeling for porous wicked heat pipes including non-Darcian effects in the literature was done by Huang and Chen [45] using lattice Boltzman method. Validation of the model was performed by comparing with experimental results [51] and theoretical calculations [41, 52] in the literature. Similar results in [43] for both constant vapor pressure and linear variation of liquid velocity were also reported in [45].

1.1.2   Modeling of grooved wick structured heat pipes

Studies related to grooved and micro heat pipes have been conducted extensively in the literature because of its relatively easy fabrication and available numerical and analytical solutions [54–57]. Previous models of fluid flow and energy transport in heat pipes with grooved wicks and micro heat pipes with sharp-angled corners serving as liquid arteries were revisited to demonstrate the existing approaches in the modeling.

Cotter [31] in 1984 and Babin et al. [54] in 1990 offered an analytical model to calculate the maximum heat transfer capacity and the dryout limit of a micro

heat pipe. For both liquid and vapor regions; one-dimensional, steady and incompressible flow assumptions were used to solve momentum equation. Besides, the variation of radius between liquid and vapor along the heat pipe was calculated by using Young-Laplace equation. Conduction through the heat pipe solid material was ignored and assumed that heat was transferred with phase change only. Babin et al. [54] compared numerical results with their own experiments and noticed inconsistency for dryout phenomenon. The onset of dryout was defined where the contact angle between the liquid and the solid was 60° in [54], and according to authors, the inconsistency between the experimental and the numerical results was due to the definition of the dryout. It was suggested that dryout phenomenon should be understood and defined more clearly in order for better modeling.

One-dimensional thermal model and hydrodynamic model were used to model flat miniature heat pipes with rectangular grooves [15], and axially grooved heat pipes with trapezoidal grooves [58]. The effect of liquid-vapor interfacial shear stress, liquid meniscus variation and the amount of working fluid in heat pipes were taken into account in the model that were used to estimate the maximum heat transfer rate analytically. Hopkins et al. [15] compared the model results with three different heat pipe experiments and validated for trapezoidal grooves. However, the predictions for rectangular grooves were not as good as those of trapezoidal grooves. Anand et al. [58] also validated the model with their own experiments specifically at lower operating temperatures. In addition, it was reported that variation of the vapor pressure was negligible compared to liquid pressure.

Thermal resistances of the heat pipe solid material in both longitudinal and transverse direction, thin film region in evaporator and condenser, condensed working fluid on fin top and working fluid inside the grooves affect heat pipe performance directly. Thermal network model was implemented into one-dimensional hydrodynamic model based on Young-Laplace equation for miniature heat pipes with trapezoidal grooves [55] and axially grooved heat pipes with trapezoidal and rectangular grooves [59]. Their models included the effect of liquid-vapor interfacial shear stress, liquid meniscus variation and the amount of working fluid.

13

The maximum heat transferred through the heat pipe was predicted analytically and validated experimentally in both [55] and [59]. Kim et al. [58] suggested that thermal optimization of grooved wick structure can be analyzed with the model for groove width and height. Desai et al. [59] showed that with an increase in the number of grooves in the heat pipe, thermal resistance decreased and the maximum amount of transferred heat increased. However, after a certain point, as the pressure drop due to the friction exceeded the capillary pumping power, the maximum transferred heat decreased. Trapezoidal grooves with different inclination angles and rectangular grooves were analyzed in [59], and it was found that the heat carrying capacity of trapezoidal grooved heat pipes was higher compared to the rectangular grooved ones.

Two-dimensional hydrodynamic models [60, 61] and one-dimensional hydrodynamic model [62] were studied numerically without using thermal models. Only evaporator and adiabatic regions were considered in [62] for V-shaped microgrooves, and the onset of dryout and its location were estimated numerically and determined experimentally. On the other hand, the maximum heat transfer capability of V-shaped microgrooves [60] and trapezoidal microgrooves [61] were predicted by solving two-dimensional hydrodynamic model along the heat pipe, and verified with experimental results of previous studies [63] and [64], respectively. Thomas et al. [61] reported that mean velocity and volumetric flow rate depend on shear stress linearly.

The majority of studies in the literature modeled the heat pipe using mass, momentum, and energy equations for both liquid and vapor regions together with Young-Laplace equation for the variation of radius between liquid and vapor, and then solved the governing non-linear equations numerically including the effect of liquid-vapor interfacial shear stress. Micro heat pipes with triangular grooves [65–74] and triangular grooves with varying cross-sectional areas [75], axially grooved heat pipes with rectangular grooves [76], Ω-shaped grooves [77], trapezoidal grooves [78], and flat plate heat pipes with rectangular grooves [32, 56, 79] were investigated by using this method. One-dimensional, steady and incompressible flow was assumed while modeling flow in both liquid and vapor regions in [32, 56, 65–68, 70–79] and a transient model was developed in [68] by

14

using a similar approach. Heat transfer at the evaporators was assumed to be due to phase change mechanism only in [65–69, 75–79] and one-dimensional conduction in solid was added to energy balance in [32, 56, 70–74]. Those modeling strategies predicted the maximum heat transport capability of heat pipe except [32, 56, 65–67, 70, 72, 75–77, 79], and temperature distribution were reported in [56, 67, 74]. Numerical models were compared with previous studies in the literature to be verified. Numerical and experimental studies that were used in the validation were as follows:

- Longtin et al. [66], Hung and Tio et al. [70], Chang and Hung et al. [72], Tio and Hung et al. [73] are verified using Babin et al. [54]
- Khrustalev and Faghri [65] is verified using Wu and Peterson [80]
- Suman et al. [68] is verified using Anand et al. [62]
- Jung and Boo [74] is verified using Moon et al. [81]
- Do et al. [56] is verified using Hopkins et al. [15] and Lin et al. [82]

Experimental setups were constructed in [32, 77–79] to verify numeric models. Liquid block (pool) region occurs at the condenser due to excess amount of liquid inside the heat pipe, and increases the thermal resistance. It was reported that [55, 56, 65] were able to determine pool condition. Hung and Tio [71] analyzed the effect of gravity on the heat pipe performance, and showed that the heat pipe carried more heat when the effect of gravity is favorable. Furthermore, liquid velocity variation was reported to be similar with [32, 43, 45, 71, 77, 79] for both positive and negative inclination angles. Singh [75] introduced a new approach by analyzing a micro heat pipe with varying cross-sectional area, and claimed that the increased apex angle from the evaporator to the condenser increased the maximum amount of heat that could be carried.

In addition to steady state one-dimensional modeling of heat pipes using mass, momentum, and energy equations for both liquid and vapor regions together with Young-Laplace equation, thermal resistance network which was used in the analytical model [55, 59] was implemented to a numerical model [83, 84] to obtain a more comprehensive heat pipe model to predict the maximum heat transfer rate [83], temperature distribution [83], and the variation of capillary

pressure [84]. Numerical estimations for both the maximum heat transport capacity and the temperature distribution were validated with the results of experiments conducted in [83]. Radius of curvatures were measured by [79] using confocal microscopy and the results of [84] were in line with those measurements. Lefèvre et al. [83] examined the effect of groove width and height on the maximum amount of heat transferred along the heat pipe. The amount of heat carried increased first with the increase of both width and height, and then decreased. Accordingly, it was reported that there is an optimum design point for both the groove width and the groove height. Lips et al. [84] concluded that the only reason for dryout is the capillary limit, and the effect of interfacial shear stress is negligible.

A resistance network model for an axially grooved heat pipe with rectangular grooves was developed and tested in [85]. Neither fluid nor vapor flow regions were modeled in this study. In the resistance network model, wall and wick conduction in both evaporator and condenser, condensation and evaporation resistances and frictional pressure losses were added as resistances using Fourier's law and correlations from [5, 86]. The modeled heat pipe was tested in four different orientations, and the predictions of the model were compared with the results at 30° inclination angle. However, the findings of the model underestimated the findings of the experiment for all heat loads used in [85].

In [87], which its modeling approach is different from all the studies mentioned above, a flat micro heat pipe including liquid/vapor/solid regions was modeled by using a coupled pore-scale three-dimensional pseudopotential lattice Boltzman model with a thermal model to analyze transient behavior without using any empirical equations. Rectangular, trapezoidal, and inverse trapezoidal grooves were studied. The authors found that the capillary pumping power ranged from high to low according to trapezoidal, rectangular, and inverse trapezoidal groove shapes. In addition, liquid and vapor pressure variations along the heat pipe for three different groove types were calculated, and vapor pressure variation was reported to be negligible.

16

1.1.3 Experimental studies

Experimental studies in the literature have an important role in terms of both verifying the numerical models and determining the operating limits of the heat pipe. In 1996, Cao et al. [88] conducted experiments with an 82 mm long (19 mm evaporator, 43 mm adiabatic region and 20 mm condenser) miniature heat pipe. Grooves that were produced from copper were rectangular in which groove width was 0.1 mm (100 μm) and groove height was 0.25 mm (250 μm). Authors reported that tilt angle had a positive effect on the heat pipe performance. For example, exactly the same heat pipe carried 10% more heat at 20° tilt compared to its horizontal position at the same temperature difference. Cao et al. [88] found that 18.3 W/cm² was the highest heat input for the heat pipe when it was placed 20° inclined with respect to the ground.

Peterson et al. [89] used silicon wafers to produce micro heat pipes. Two heat pipes with rectangular and triangular grooves were manufactured. Rectangular grooves were 45 μm wide and 80 μm depth, triangular grooves were 120 μm wide and 80 μm depth. Both heat pipes had 39 grooves and 14.1°C and 24.9°C temperature decreases were obtained at the chip for rectangular and triangular heat pipes, respectively. According to the authors, there were two reasons for the increased performance in the triangular grooved micro heat pipe; one of which was the reduction of the remaining space in the micro channels, and the other was the improvement in the corners. Corners of the triangular heat pipes were sharper compared to the rectangular heat pipes. Therefore, meniscus recession in the triangular heat pipes was larger than the rectangular heat pipes, and it was resulted in higher capillary pumping pressures.

Badran et al. [90] worked on the effect of the filling ratio on silicon micro heat pipes with methanol and water as working fluids. Two different arrays of micro heat pipes were produced with triangular cross-section. In the first array, there were 73 micro channels 260 μm wide and 185.54 μm deep. In the second array, there were 127 micro channels 100 μm in width and 70.72 μm in depth. Six different filling ratios (5%, 10%, 20%, 30%, 50% and 80%) were investigated by the researchers, and they found that 5% filling ratio gave the best result

for both heat pipes with methanol and water. Another experimental study was conducted by Chen and Chou [91] to find the optimum filling ratio, yet by using flat plate heat pipes with rectangular grooves this time. The heat pipe was made of aluminum with acetone as working fluid. Ten different filling ratios were tested between 5% and 50% with 5% increments and heat input was varied between 5 W to 60 W with 5 W increments. Grooves were rectangle with 0.2 mm wide and 0.4 mm deep. The best performance of the flat heat pipe was obtained at 25% filling ratio. 47 W heat load was carried at that filling ratio, and thermal resistance was 0.254 K/W while effective thermal conductivity was 3,150 W/m · K. In addition, the optimum filling ratio was also investigated in [92] for rectangular flat plate heat pipes. The material of the heat pipe was aluminum, and the working fluid was methanol. Six different filling ratios were tested between 10% and 60% with 10% increment. The optimum filling ratio was found to be 20%, and this result was in line with [91]. Those three studies [90–92] showed that the optimum filling ratios were different for micro and flat plate heat pipes. Chen and Chou [91] also reported that inappropriate vacuum and/or leakage had negative effects on cooling performance of the heat pipe. Thermal conductivity under inappropriate vacuum condition and leakage were measured as 200–306 W/m · K and 164 W/m · K, respectively.

Hopkins et al. [15] conducted an experimental study with flat heat pipes made of copper in 1999. Working fluid was water in all their experiments. Three different heat pipes were studied in both horizontal and vertical orientations. Two different groove structures were used in the heat pipes which were trapezoidal and rectangular grooves. Trapezoidal grooves had 0.24 mm and 0.20 mm groove depth, 0.20 mm and 0.45 mm groove top width, 0.15 mm and 0.30 mm groove bottom width and 0.16 mm and 0.20 mm fin top width. Rectangular grooves had 0.42 mm groove depth, 0.20 mm groove top width, 0.20 mm groove bottom width and 0.10 mm fin top width. The trapezoidal heat pipe, which had 0.24 mm groove depth, was filled with 20 ml liquid. The other trapezoidal heat pipe was filled with liquid which was 20% of its existing volume. Rectangular grooved heat pipe was filled with 0.84 ml of liquid. Hopkins et al. [15] tried to find the maximum heat loads for five different operating temperatures which

18

were 60°C, 70°C, 80°C, 90°C and 95°C for both horizontal and vertical orientations. The maximum heat transfer rate was obtained from the rectangular heat pipe for both vertical and horizontal orientations. Heat flux was found to be 141.8 W/cm² for the vertical orientation and as 92.8 W/cm² for the horizontal one. The maximum heat flux values for vertical and horizontal oriented trapezoidal heat pipes were approximately 70 W/cm² and 20 W/cm², respectively. It was concluded that deep grooves can carry more heat compared to shallow ones, and heat transport capacity usually depended on capillary limit directly. Among numerous experiments, only two of them were limited by boiling limit.

In 2008, Lim et al. [93] proposed a study about the effects of adverse-gravity on copper-water flat heat pipe with novel fan-shaped grooves. Width of the fan-shaped grooves was 150 μm and depth of them was 300 μm. The heat pipe was tested between $-90°$ and $90°$. Three different filling ratios (0 μL, 53.9 μL, and 189 μL) and eight different heat inputs between 1 W and 8 W with 1 W increments were applied to the flat heat pipe in the experiments. Lim et al. [93] suggested that small temperature difference means that the flat heat pipe works properly. They also reported that the flat heat pipe with a fan-shaped groove can be operated under adverse-gravity condition because of its high capillary pumping power. Finally, dryout point of the heat pipe was determined as 12 W where a sudden jump in the resistance occurs.

Lips et al. [94] worked on the effects of nucleate boiling for three different filling ratios of copper flat heat pipe. Grooves of the heat pipe were in square cross-section with 0.4 mm. Lips et al. [94] placed a transparent cover at the top of the heat pipe, so that they could easily observe what was happening in the flat heat pipe. It was reported that nucleate boiling did not stop the operation of the heat pipe. Conversely, nucleate boiling increased the heat transfer especially in the relatively large grooves. According to the authors, to generalize the effect of nucleate boiling, micro grooved heat pipes should also be investigated under nucleate boiling condition.

Peterson and Ma [63] investigated the effects of channel angle, contact angle of liquid, heat pipe length and tilt angle on the amount of heat transferred

through the heat pipe, and found that these four parameters have a direct effect on the heat pipe performance. In addition, Chen and Chou [95] investigated the effects of the length and bending angle on cooling performance of aluminum flat plate heat pipes with acetone. Four different lengths (80 mm, 150 mm, 200 mm, and 300 mm) and four different bending angles (0°, 30°, 60°, and 90°) were studied. Bending angles were examined only for 200 mm heat pipe. The minimum thermal resistance for 80 mm length heat pipe was found as 0.103 K/W and increased by a factor of 2.4, 6.0, and 17.9 for 150 mm, 200 mm, and 300 mm heat pipes, respectively. It was noticed that at around 150 mm, there was a sudden jump in the minimum thermal resistance of the flat heat pipe. Contrary to expectations, thermal resistance decreased as the bending angle increased.

Alijani et al. [57] were conducted an experimental study to determine the effect of design parameters on flat plate heat pipes. Four heat pipes with different groove densities were tested at different heat loads and filling ratios. The results showed that there was not a single optimum point for heat pipes; instead, the heat pipe worked at an optimum level in a certain range especially at low heat fluxes. However, as the heat flux increased, this range shrank to a single optimum point. In addition, effectiveness of the heat pipe increased with increasing groove density, but narrower and shallower grooves (i.e., high groove density) encountered dryout at lower heat fluxes. According to the results of the study, heat pipe performance depends on many parameters, so the heat pipe should be designed according to the requirements of the particular application.

All the studies mentioned above were done under steady state condition. However, transient behavior of the heat pipes was also studied [96–98] in the literature. The heat pipes with porous [96, 97] and groove [98] wick structures were tested under different heat loads. The results showed that the heat pipe with porous wick structure reached steady state in approximately five minutes [96, 97], whereas it became ten minutes for grooved heat pipes [98].

1.2 Objective and Outline of the Current Study

As explained in the previous section, many studies have been conducted to understand the working principle of the heat pipe, to see its limits, and to model it correctly. Experimental studies require long processes with design, production, construction, and commissioning. Tested parameters and measurement aims should be determined before the manufacturing, and then applied to design. The machining of micro channels which is needed especially in grooved heat pipes is a time consuming production process due to the necessity of precise production. Since heat pipes are operated under vacuum, the vacuum environment must be provided during the commissioning phase. Providing the vacuum environment is a difficult process due to the fact that the design and construction of the heat pipe must be airtight which directly affects the heat pipe performance. As a result, experimental work requires a long and expensive process.

Numerical studies, on the other hand, provide rapid information about the heat pipe performance. However, simplified models incorrectly predict heat transfer because they cannot accurately simulate the flow region. Comprehensive models that accurately model the heat pipe require long computation times and high computing power.

There are three objectives of the current study. The first objective is to design and manufacture a modular heat pipe experimental setup for determining the heat pipe performance. The second objective of the current study is to propose a novel wick designs for improved heat pipe performance. Since a capillary limit is one of the most critical phenomena that affects the heat pipe performance directly, increasing the capillary limit was aimed via better wick design to enhance the heat carrying capacity. Not only for increasing the capillary limit, but also decreasing the maximum temperature in the evaporator especially at high heat fluxes as well as carrying more heat compared to the same size heat pipes were among the aims for improved heat pipe design. The third and final objective of the current study is to develop a fast and accurate numerical model for designing the heat pipes, and to adapt it for grooved wick structures for simulating the experiments in the first place. Numerical model is both a design and diagnosis

tool for heat pipes, and predicts temperature and pressure distribution along the heat pipe up to the onset of dryout. In addition, liquid pool —when present— can be predicted *via* this numerical model. Designers or researchers can decide on the heat pipe design or specify the operating limits of an existing heat pipe by using this tool. The numerical model is validated by both the experimental setup of the current study and previous studies in the literature for grooved wicked heat pipes with constant and variable cross-sections.

This thesis is organized as follows: in Chapter 1, definition and types the of heat pipes are introduced. Previous studies for both experimental and numerical methods are examined, and the objective of the current study is presented. In Chapter 2, first the modeling of fluid flow and thermal resistances in the numerical model are explained. Then, the validation of the numerical model is given through previous studies in the literature are explained. In Chapter 3, design, construction, and commissioning of the experimental setup are introduced. Then, results of both experiments and numerical model are compared. In Chapter 4, proposed innovative groove geometries are explained, and their performance improvements are validated by using numerical model. Finally, experiments using viable innovative geometries are introduced. Finally, the results of the current study are discussed and concluding remarks are presented in Chapter 5.

CHAPTER 2

NUMERICAL MODELING

The modeling of the heat pipes has been studied over the years ranging from simple capillary limit analyses [4, 5, 7] to extensive 3-D models [56, 83]. Simple models are fast in terms of computing time but the flow field prediction may not be sufficiently accurate. On the other hand, extensive models predict the flow domain accurately but require long computing time. In this chapter, modeling framework of the numerical model, which is both a diagnosis and design tool, including coupled fluid flow and thermal resistance models are introduced.

The reason of mentioning the tool as the diagnosis tool is its ability to analyze an existing (i.e., for specific geometric parameters) heat pipe for different heat loads and cooling strategies. On the other hand, the numerical model is also a design tool, as well, in which a heat pipe can be designed by using the numerical model for different geometric parameters, heat loads, and cooling strategies depending on the constraints in the cooling problem where the heat pipe is planned to be used. Therefore, in general, the numerical model helps us to determine the geometric parameters, heat input and cooling requirements in the experimental setup which will be introduced in Section 3.

This chapter includes the thermal resistance networks, fluid flow model, solution procedure, detailed calculations of those models for rectangular grooved heat pipes, and validation of the numerical model through previous studies in the literature.

2.1 Thermal Resistance Networks

In the present model two thermal resistance networks are established to simulate the heat transfer through a 3-D conduction in the solid and liquid. One of them is the two-node thermal resistance network, and the other one is the multi-slice thermal resistance network.

2.1.1 Two-node thermal resistance network

In this network evaporator and condenser regions are represented by single thermal resistances (R^e and R^c); and, evaporation or condensation along the adiabatic region is neglected. In other words, it is assumed that all evaporation occurs in the evaporator region, and all condensation in the condenser region. Conduction heat transfer that occurs in the axial direction of the heat pipe is also represented by one thermal resistance (R_{ax}). The last resistance in the two-node thermal resistance network is the resistance that is between the condenser region and the ambient (R^{conv}). The schematic representation of the two-node thermal resistance network is given in Figure 2.1.
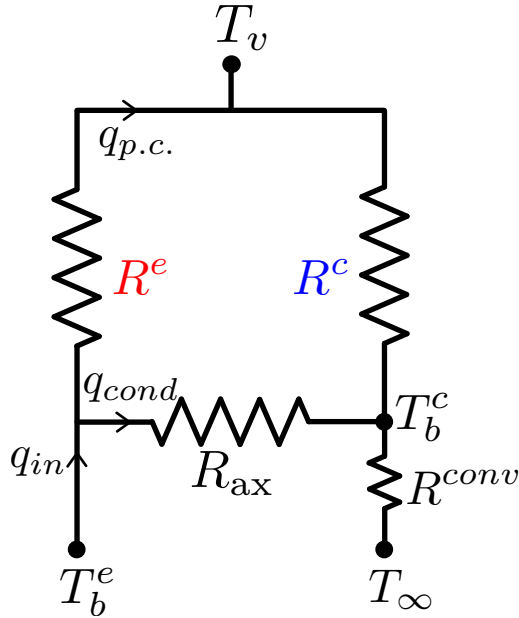
Figure 2.1: The two-node thermal resistance network model of the heat pipe

The two-node thermal resistance network calculates the maximum temperature at the evaporator (T_b^e), phase change $(q_{p.c.})$, and conduction (q_{cond}) heat transfers for the heat pipe for given geometric parameters, wick details, and cooling conditions. In this model, specifying either base temperature of the condenser (T_b^c) or ambient temperature (T_∞) with the corresponding heat transfer coefficient is required for the calculation. Then, knowing the total heat to be transported (q_{tot}) and the thermal resistances, the maximum temperature at the evaporator, the amount of heat transferred by phase change and conduction can be calculated. However, because of the limited number of nodes, this model did not enable a detailed calculation of the temperature variation along the heat pipe.

2.1.2 Multi-slice thermal resistance network

To achieve a better resolution of heat pipe performance, the heat pipe is divided into a large number of slices including the adiabatic region in the multi-slice thermal resistance network. Therefore, the network allows either condensation or evaporation in the adiabatic region as well. Thus, the effect of axial transfer heat in the adiabatic region on the heat pipe performance is also simulated.
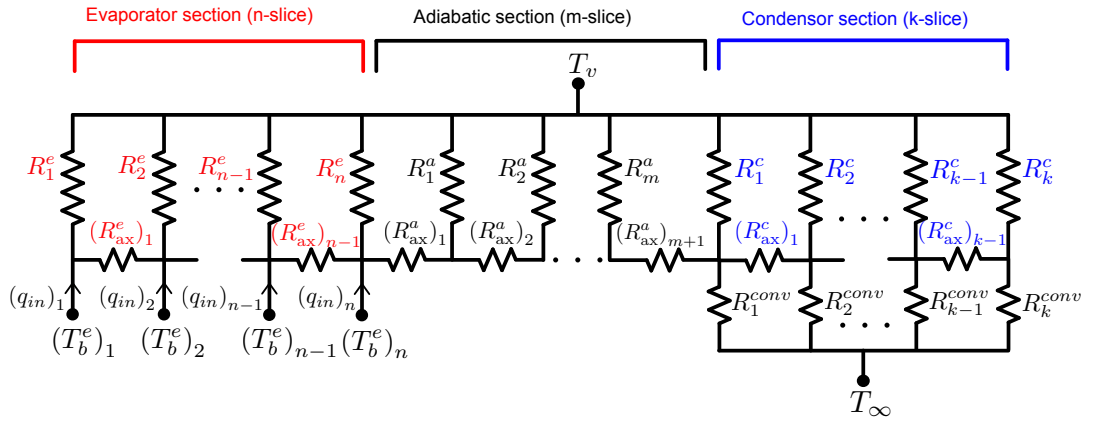
Figure 2.2: The multi-slice thermal resistance network model of the heat pipe

Resistances in the evaporator (R_i^e), adiabatic (R_i^a) and condenser (R_i^c) regions are calculated with the same approach that is employed in the two-node thermal resistance network. However, different from two-node, in the multi-slice each resistance is calculated by using the geometrical parameters in the particular slice.

25

These slices are connected to each other via axial resistances in the evaporator ($R_{ax,i}^e$), adiabatic ($R_{ax,i}^a$) and condenser ($R_{ax,i}^c$) regions in the multi-slice thermal resistance network, and temperatures at each slice can be calculated by this network. The schematic representation of the multi-slice thermal resistance network is given in Figure 2.2.

Finally, there are two thermal resistance networks to calculate the heat transfer along the heat pipe. One of them has only four resistance which is computationally easy; however, it cannot resolve the temperature variation along the heat pipe. On the other hand, the other one includes multiple resistance, and it is computationally more complex compared to the first one. Nevertheless, it estimates the temperature variation along the heat pipe with a finer resolution, and accounts for phase change in the adiabatic region.

2.2 The Fluid Flow Model

In the current study, the proposed fluid flow model is defined and solved using the developed model according to the type of the wick structure with high accuracy and low computational demand. The vapor flow is not solved; instead, the pressure of the vapor is assumed to be constant and equal to saturation pressure along the heat pipe according to the results of [32, 43–45, 55, 58, 76–79, 87, 99].

The liquid flow inside the heat pipe is solved in the fluid flow model. Since the variation of the mass flow rate of the liquid increases almost linearly in condenser region, reaching its maximum value in adiabatic region, and decreasing linearly in evaporator region ([32, 43, 45, 71, 77, 79, 99]), in the present model liquid mass flow rate is defined as in Eq. 2.1, and mass flow rate in the groove converges when the thermal resistance network converges.

$$\dot{m}_l(z_i) = d_{0,i}z_i + d_{1,i}, \quad 0 \leq z \leq L \tag{2.1}$$

In the liquid flow model, an available analytical solution of flow is used in the calculation of pressure distribution in the fluid. The mass flow rate of the liquid

and the pressure variation along the heat pipe are interrelated and a geometrical function, $\mathbb{G}(z)$, is defined. The geometrical function, $\mathbb{G}(z)$, depends on the wick geometry and is defined according to it. For example, The geometrical function, $\mathbb{G}(z)$, for rectangular groove is defined as follows and derivation of it will be explained in Section 2.4.1.

$$\mathbb{G}(z) = \frac{256}{\nu\pi^6} \frac{w^3(z) \ h^3(z)}{[w^2(z) + 4h^2(z)]} \tag{2.2}$$

Liquid flow along the heat pipe is assumed as one-directional in this study, and liquid flow is sustained by pressure gradient along the heat pipe. Since variation of the pressure at an arbitrary cross section is considerably small over the axial variation, it is assumed to be constant over the slice element in the numerical model developed in this thesis. Therefore, integration in Eq. (2.3) can be performed under the assumption of constant pressure gradient at a certain cross section.

$$\dot{m}_l(z) = \int (\rho\mathbf{u}) \cdot \mathbf{n} \ dA \tag{2.3}$$

Consequently, the mass flow rate along the heat pipe can be expressed as the product of the pressure gradient and a corresponding function obtained after integration, which is designated as $\mathbb{G}(z)$. The final form of the relation between the mass flow rate and the pressure gradient is shown in Eq. (2.4).

$$\dot{m}_l(z) = \mathbb{G}(z) \left(\frac{dp}{dz} + f_b \right) \tag{2.4}$$

where f_b is the constant associated with a constant body force.

The liquid pressure variation along the heat pipe is found by combining mass flow rate prediction along the heat pipe which is given in Eq. 2.1 with the liquid pressure variation which is given in Eq. 2.4. The final form of the pressure

distribution equation along the heat pipe is as follows:

$$p(z_i) = \int \left(\frac{d_{0,i} z_i + d_{1,i}}{\mathbb{G}(z)} - f_b \right) dz, \quad 0 \leq z \leq L \tag{2.5}$$

To calculate the pressure distribution along the heat pipe, boundary conditions need to be defined for the Eq. 2.5. These boundary conditions are directly related to the operational characteristic of the heat pipe; and in a desirable operation of the heat pipe, dryout should not exist at the evaporator. Therefore, an onset of the dryout needs to be determined first, and the material contact angle, θ_{ca}, which is a characteristic property of a liquid in contact with a certain solid surface, should be known for that. The lowest value of the angle at the contact line or triple line, where three phases (i.e., solid walls of the wick, liquid, and vapor phases of the working fluid) meet, can be at least as the material contact angle and the more the fluid is stretched beyond the contact angle, the dryout may occur suddenly. Therefore, Young-Laplace relation using contact angle is one of the boundary conditions to calculate the pressure value at $z = 0$ (Eq. 2.6).

$$p|_{z=0} = p_v - \frac{2\sigma \cos(\theta_{ca})}{r_{eff}} \tag{2.6}$$

where r_{eff} is the effective capillary radius of the wick and σ is the surface tension of the liquid. The mass flow rate of the liquid at the end of the condenser region of the heat pipe is zero. Therefore, another boundary condition comes from the vanishing pressure gradient at the $z = L_e + L_a + L_c = L$.

$$\left. \frac{dp}{dz} \right|_{z=L} = 0 \tag{2.7}$$

The final boundary condition comes from the mass flow rate of the liquid inside the heat pipe at a particular location. The mass flow rate in each slice is calculated by dividing of the rate of phase change heat transfer to latent heat of vaporization (i.e., $\dot{m}_i = q_{p.c.,i}/h_{fg}$). Therefore, the final boundary condition

28

becomes:

$$\frac{dp}{dz}\bigg|_i = \frac{\dot{m}_i}{\mathbb{G}(z)} \tag{2.8}$$

Equations so far are in general form and can be used with multi-slice thermal resistance network. In the case of two-node thermal resistance network, the variation of the mass flow rate of the liquid is initially taken to be linearly increasing in the condenser, constant in the adiabatic region, and linearly decreasing in the evaporator since it is assumed that neither evaporation nor condensation occurs in the adiabatic region. Therefore, liquid mass flow rate equations in the evaporator, adiabatic, and condenser regions are written as Eqs. (2.9a), (2.9b), and (2.9c), respectively.

$$\dot{m}_l(z) = E_0 z + E_1, \quad 0 \leq z \leq L_e \tag{2.9a}$$

$$\dot{m}_l(z) = D_0, \quad L_e \leq z \leq L_e + L_a \tag{2.9b}$$

$$\dot{m}_l(z) = F_0 z + F_1, \quad L_e + L_a \leq z \leq L_e + L_a + L_c \tag{2.9c}$$

The liquid pressure variation along the heat pipe is found by combining mass flow rate predictions along the heat pipe (i.e., Eqs. (2.9a–2.9c)) with the liquid pressure variation which is given in Eq. 2.4. The final form of the pressure distribution equations for the evaporator, adiabatic, and condenser regions are as follows:

$$p(z) = \int \left(\frac{E_0 z + E_1}{\mathbb{G}(z)} - f_b \right) dz, \quad 0 \leq z \leq L_e \tag{2.10a}$$

$$p(z) = \int \left(\frac{D_0}{\mathbb{G}(z)} - f_b \right) dz, \quad L_e \leq z \leq L_e + L_a \tag{2.10b}$$

$$p(z) = \int \left(\frac{F_0 z + F_1}{\mathbb{G}(z)} - f_b \right) dz, \quad L_e + L_a \leq z L_e + L_a + L_c \tag{2.10c}$$

Phase change is assumed to be zero in the adiabatic region. Therefore, the amount of the liquid mass that is carried throughout the wick along the adiabatic region is taken as constant, and this constant mass flow rate ($\dot{m}_a$) is calculated by using latent heat of vaporization (i.e., $\dot{m}_a = q_{p.c.}/h_{fg}$). By using this assumption, in addition to boundary conditions that are defined in Eqs. (2.6 and 2.7), the last boundary condition is calculated as:

$$\left.\frac{dp}{dz}\right|_{adibatic} = \frac{\dot{m}_a}{\mathbb{G}(z)} \tag{2.11}$$

Eqs. (2.10a–2.10c) indicate that functions that define the pressure distribution are piecewise continuous. Therefore, in addition to boundary conditions, appropriate matching conditions should be defined at the overlapping points of the adiabatic region with the evaporator ($z = L_e$) and condenser ($z = L_e + L_a$) regions. Because of the continuity of both pressure and pressure gradient at these points, the following equations (Eqs. (2.12a and 2.12b)) are obtained for these conditions.

$$\left[\int\left(\frac{E_0 z + E_1}{\mathbb{G}(z)} - f_b\right)dz\right]_{z=Le} = \left[\int\left(\frac{D_0 z}{\mathbb{G}(z)} - f_b\right)dz\right]_{z=Le} \tag{2.12a}$$

$$\left[\int\left(\frac{D_0 z}{\mathbb{G}(z)} - f_b\right)dz\right]_{z=Le+La} = \left[\int\left(\frac{F_0 z + F_1}{\mathbb{G}(z)} - f_b\right)dz\right]_{z=Le+La} \tag{2.12b}$$

2.3 The Solution Procedure

While analyzing the heat pipe, the numerical model developed in this thesis solves the coupled fluid flow and thermal resistance network. The solution procedure of the numerical model is given in Figure 2.3. The numerical model requires geometric parameters of the heat pipe which are the evaporator length (L_e), adiabatic length (L_a), condenser length (L_c) and wick geometry. In addition to these parameters, cooling method should be specified. This can be a specified surface temperature of the condenser base (T_c^b) which is valid for only two-node thermal resistance network, or convection heat transfer to the ambient

at temperature (T_{amb}). Finally, the total amount of heat (q_{tot}) which is aimed to be transported by the heat pipe is specified.

The solution procedure starts with guessing both phase change heat transfer, q_{pc}, and the vapor temperature, T_v. Then, the fluid flow model is explained in detail in Section 2.2 is run by using initial guesses, and the vapor temperature is used for property evaluation of the working fluid. The contact angle variation along the heat pipe, $\theta(z)$, and thus the variation of the radius of curvature, $R(z)$, are calculated in the fluid flow model.
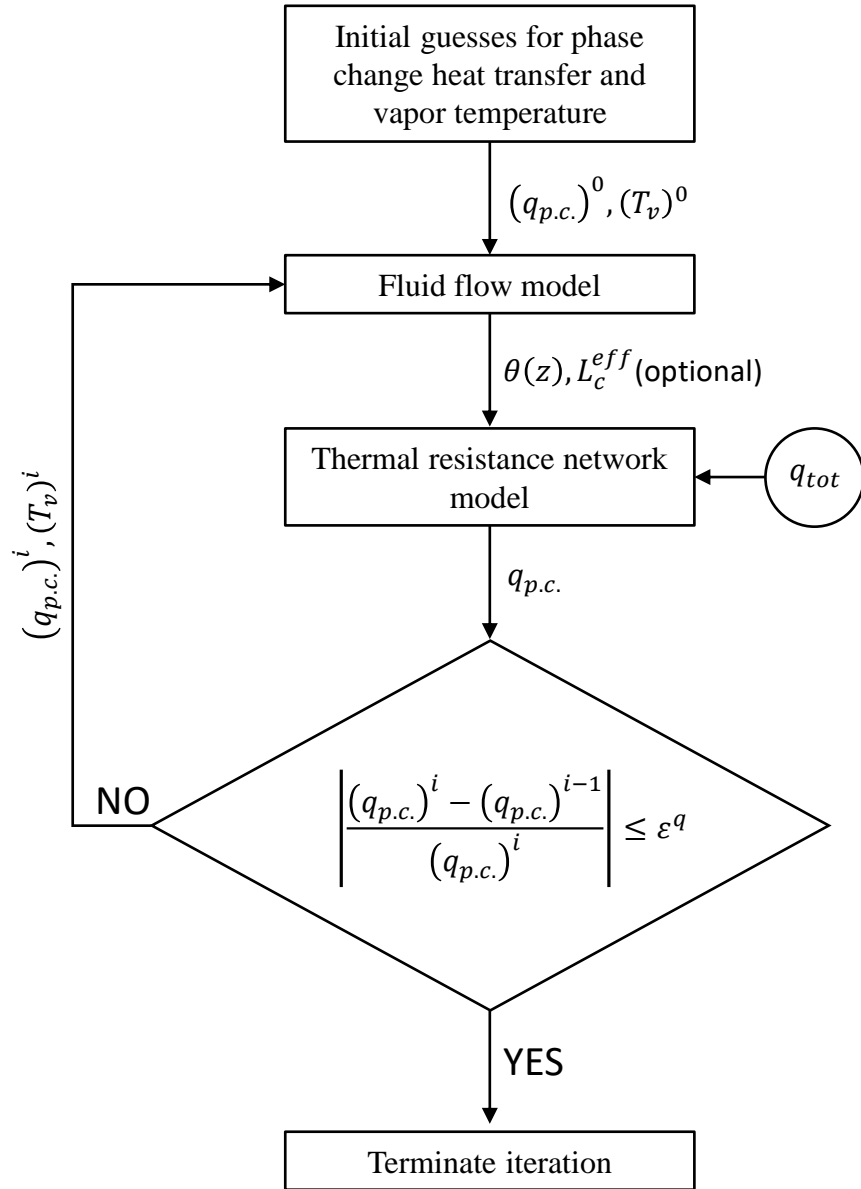
Figure 2.3: Solution procedure of the numerical model

The thermal resistance model uses the results of the fluid flow model and geometric parameters, in which a thermal resistance network including resistances in the evaporator, the adiabatic, and the condenser regions is constructed (see Section 2.1). In addition to these resistances, axial conduction along the heat pipe is also added to the network which enables the calculation of a conductive heat transfer (q_{cond}). As a result of the thermal resistance model, q_{pc}, T_v, the maximum evaporator temperature (T_e^{max}), temperature distribution along the heat pipe, and q_{cond} are found. Then, convergence criteria are checked by using calculated and guessed values of q_{pc}. If these conditions are satisfied, calculation is terminated. Otherwise, q_{pc} and T_v are updated. The solution procedure is repeated until convergence criteria are satisfied. Patent application for this algorithm has been started.

The fluid flow model calculates the contact angle variation along the heat pipe by using geometric parameters of the heat pipe, phase change heat transfer and vapor temperature as mentioned above. In the case of high heat input, heat pipe cannot provide sufficient capillary pumping. Under this circumstance, dryout or pool region formation is observed in the heat pipe, and these phenomena are explained in Section 4.2.1 in detail. The numerical model developed in this thesis is able to determine the pool region formation. In this case, the contact angle, θ_{ca}, is at its minimum value — equal to material contact angle— at the beginning of the evaporator, and approaches 90° before reaching the end of the condenser. Therefore, the remaining section of the condenser becomes ineffective, and the effective condenser length, L_c^{eff}, can also be calculated in the numerical model developed in this thesis.

2.4 Submodeling for Rectangular Grooved Heat Pipes

2.4.1 Liquid Flow for Rectangular Grooved Heat Pipes

When modeling the liquid flow along the rectangular channel, it is assumed that the liquid flow is hydrodynamically fully developed, laminar and incompressible since the Reynolds number (Re) is low in the rectangular channels of the grooved

heat pipes. Calculation for the rectangular channel is started with the analytic solution of the rectangular duct where the width and height of the rectangular duct are a and b, respectively. Then, the conservation equations are solved for the rectangular duct by using separation of variables and the mean velocity, U_m, is found as follows:

$$U_m = \frac{4}{a^2 b^2} \frac{1}{\mu} \frac{\Delta P}{L} \sum_{m=1}^{\infty} \sum_{n=1}^{\infty} \frac{[1-(-1)^n]^2 [1-(-1)^m]^2}{(\beta_m^2 + \lambda_n^2) \lambda_n^2 \beta_m^2} \tag{2.13}$$

where $\lambda_n = n\pi/b$ and $\beta_m = m\pi/b$

The effect of the higher order terms (i.e., where m and n are different from 1) in the Eq. 2.13 is small. Therefore, the higher order terms can be ignored and the mean velocity for the rectangular duct is obtained as follows:

$$U_m = \frac{64}{\mu \pi^6} \frac{a^2 b^2}{(a^2 + b^2)} \frac{\Delta P}{L} \tag{2.14}$$

Note that the rectangular channel in the grooved heat pipe is half of the rectangular duct. Therefore, to calculate the mean velocity in the rectangular groove in which w is width and h is height, a and b in Eq. 2.14 are replaced with w and $2h$, respectively. Finally, after this modification, mean velocity for the rectangular groove is calculated as,

$$U_m = \frac{256}{\mu \pi^6} \frac{w^2 h^2}{(w^2 + h^2)} \frac{\Delta P}{L} \tag{2.15}$$

The mass flow rate in the rectangular groove is calculated by the product of the mean velocity, the cross sectional area, and the density. Finally, the geometrical function, $\mathbb{G}(z)$, for the rectangular groove is calculated as follows:

$$\mathbb{G}(z) = \frac{256}{\nu \pi^6} \frac{w^3(z) \; h^3(z)}{(w^2(z) + 4h^2(z))} \tag{2.16}$$

By means of the geometric function of the rectangular groove (Eq. 2.16), pressure variation in both constant and variable cross sections in the rectangular

grooved heat pipes can be calculated. The final forms of the pressure distribution equation are obtained by inserting the Eq. 2.16 into Eq. 2.5 and it is found as follows:

$$p(z_i) = \int \left((d_{0,i}z_i + d_{1,i}) \frac{\pi^6 \nu}{256} \frac{(w^2(z) + 4h^2(z))}{w^3(z) \; h^3(z)} \right) dz, \quad 0 \leq z \leq L \qquad (2.17)$$

In the case of two-node thermal resistance network, the final forms of the pressure distribution equations are obtained by inserting the Eq. 2.16 into Eqs. (2.10a–2.10c), and these equations are found as follows:

$$p(z) = \int \left[(E_0 z + E_1) \frac{\pi^6 \nu}{256} \frac{(w^2(z) + 4h^2(z))}{w^3(z) \; h^3(z)} \right] dz \qquad (2.18a)$$

where $0 \leq z \leq L_e$

$$p(z) = \int \left[D_0 \frac{\pi^6 \nu}{256} \frac{(w^2(z) + 4h^2(z))}{w^3(z) \; h^3(z)} \right] dz \qquad (2.18b)$$

where $L_e \leq z \leq L_e + L_a$

$$p(z) = \int \left[(F_0 z + F_1) \frac{\pi^6 \nu}{256} \frac{(w^2(z) + 4h^2(z))}{w^3(z) \; h^3(z)} \right] dz \qquad (2.18c)$$

where $L_e + L_a \leq z \leq L_e + L_a + L_c$

2.4.2   Thermal Model for Rectangular Grooved Heat Pipes

For the rectangular grooved heat pipes, three different types of resistances occur due to evaporation, condensation and axial conduction. To establish a thermal resistance network model for the grooved heat pipes, these different types of resistance should be calculated. In this section, details of these resistances are explained in detail.

2.4.2.1   Thermal Resistance Model for Evaporating Section

To calculate the overall equivalent resistance at the evaporating cross section (R^e), a one-dimensional thermal resistance network is established between the base temperature at the evaporating region (T_b^e) and the vapor temperature, T_v.

This model includes resistances due to the conduction in both solid and liquid, and phase change on the liquid-vapor interface. The schematic representation of these resistances is illustrated in Figure 2.4.
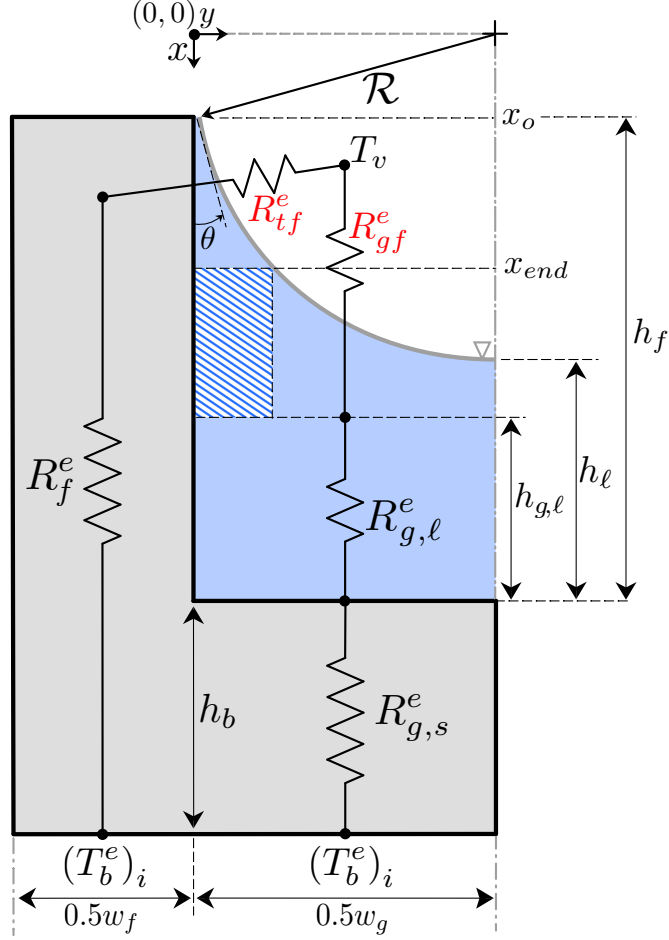
Figure 2.4: Schematic representation of the thermal resistance network at an evaporating section

Fin side resistance (R_f^e), groove side solid $(R_{g,s}^e)$ and groove liquid $(R_{g,l}^e)$ resistances at the evaporating region occur due to conduction throughout the solid and the liquid that compose the heat pipe. To calculate these resistances, Fourier's law of conduction is used, and the resistances per unit length are found as follows:

$$R_f^e = \frac{h_b + h_f - 0.5(x_m - x_0)}{k_s(0.5w_f)} \tag{2.19}$$

$$R^e_{g,s} = \frac{h_b}{k_s(0.5w_g)} \qquad (2.20)$$

$$R^e_{g,l} = \frac{h_{g,l}}{k_l(0.5w_g)} \qquad (2.21)$$

At the top of the fin where the triple line occurs, there is a thin liquid film, and most of the heat evaporates from this region [100]. Therefore, the thin film resistance (R^e_{tf}) should be modeled accurately to obtain the correct equivalent resistance in an evaporating section. Figure 2.5 illustrates the schematic representation of the thin film resistance network at the evaporating region. To calculate the thin film resistance (R^e_{tf}), thin film region is divided into discrete finite sections, and each discrete section has two resistances, namely the resistance due to liquid in the thin film ($R^e_{tf,l}$) and phase change resistance at the liquid surface ($R^e_{tf,pc}$).
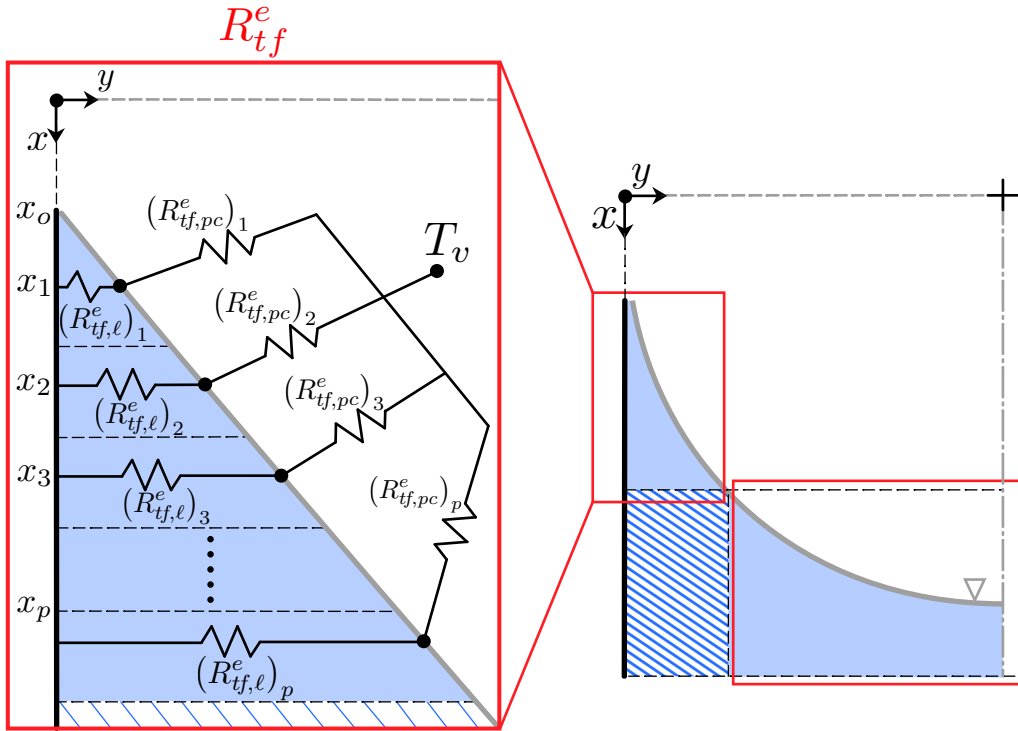
Figure 2.5: Schematic representation of the thin film resistance network at an evaporating section

To calculate the thin film liquid resistance ($R^e_{tf,l}$), an average thickness, (δ_n), is

required for each discrete finite sections and this is calculated using the area of each region via Eq. 2.22. Then, the resistance due to the conduction through the liquid per unit length is calculated using Eq. 2.23 since it is so thin that there is no convection in the film.

$$\bar{\delta}_n = \frac{\int_{x_{n-1}}^{x_n} \left(w_g - \sqrt{R^2 - x^2}\right) dx}{(x_n - x_{n-1})} \tag{2.22}$$

$$(R^e_{tf,l})_n = \frac{\bar{\delta}_n}{k_l(x_n - x_{n-1})} \tag{2.23}$$

Another resistance in the thin film region occurs on the liquid-vapor interface due to phase change and this resistance will be named as the thin film phase change resistance $(R^e_{tf,pc})$ in the current study. While calculating the resistance, the evaporating mass flow rate from the thin film region that can be calculated with the formula that was derived by Sujanani and Wayner [101], Eq. 2.24, is used.

$$\dot{m}''_{evap} = a(T_{lv} - T_v) \tag{2.24}$$

where

$$a = \frac{2\hat{\sigma}}{2 - \hat{\sigma}} \left(\frac{M}{2\pi R_u T_{lv}}\right)^{1/2} \left(\frac{M p_v h_{lv}}{R_u T_v T_{lv}}\right) \tag{2.25}$$

Evaporating mass flow rate, $(\dot{m}''_{evap})$, can also be calculated using the enthalpy of evaporation and the evaporating area as showed in Eq. 2.26.

$$\dot{m}''_{evap} = \frac{Q}{h_{fg} s_n L_e} \tag{2.26}$$

By combining Eqs. 2.24 and 2.26, the thin film phase change resistance per unit

length $(R_{tf,pc}^e)$ is calculated as follows:

$$(R_{tf,pc}^e)_n = \frac{1}{ah_{fg}(s_n - s_{n-1})} \tag{2.27}$$

The overall resistance in the thin film region (R_{tf}^e) is calculated by the combination of series and parallel connections of $R_{tf,l}^e$ and $R_{tf,pc}^e$ as given in Figure 2.5. The overall resistance in the thin film region (R_{tf}^e) is calculated as follows:

$$R_{tf}^e = \sum_1^p \left[\frac{1}{(R_{tf,l}^e)_n + (R_{tf,pc}^e)_n} \right]^{-1} \tag{2.28}$$

The last resistance to be used in the calculation of the overall evaporating region resistance (R^e) is the film resistance on the groove side (R_{gf}^e). Figure 2.6 is the schematic representation of the thin film resistance network in an evaporating section. To calculate thin film resistance (R_{gf}^e), thin film region is divided into discrete finite sections, and each section has two resistances, namely the resistance due to liquid in the thin film $(R_{gf,l}^e)$ and phase change resistance at the liquid-vapor interface $(R_{gf,pc}^e)$.
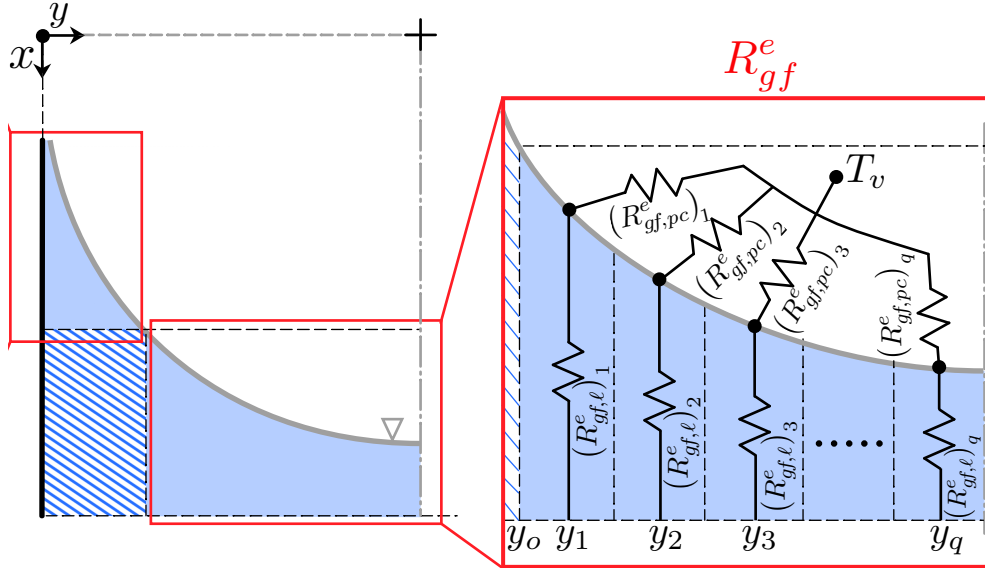
Figure 2.6: Schematic representation of the film resistance network on the groove side of an evaporating section

A procedure identical to the one used to calculate R_{tf}^e is applied in the calculation

38

of the film resistance on the groove side (R_{gf}^e). First, an average thickness, $(\delta_{n,g})$, is calculated for each discrete section, then the resistance due to the conduction through the liquid per unit length is calculated with Eq. 2.30.

$$\bar{\delta}_{n,g} = \frac{\int_{y_{n-1}}^{y_n} \left(h_f - h_{g,l} - \sqrt{R^2 - y^2} \right) dy}{(y_n - y_{n-1})} \tag{2.29}$$

$$(R_{gf,l}^e)_n = \frac{\bar{\delta}_{n,g}}{k_l(y_n - y_{n-1})} \tag{2.30}$$

and the phase change resistance is calculated as follows:

$$(R_{gf,pc}^e)_n = \frac{1}{ah_{fg}(s_n - s_{n-1})} \tag{2.31}$$

The overall resistance in the groove film region (R_{gf}^e) is calculated by the combination of series and parallel connections of $R_{gf,l}^e$ and $R_{gf,pc}^e$ as given in Figure 2.6. The overall resistance in the groove film region (R_{gf}^e) is calculated as follows:

$$R_{gf}^e = \sum_1^p \left(\frac{1}{(R_{gf,l}^e)_n + (R_{gf,pc}^e)_n} \right)^{-1} \tag{2.32}$$

Electrical analogy representation of the resistances that are introduced in Figures (2.4–2.5) in the thermal resistance network is shown in Figure 2.7.

Finally all those resistances which are calculated separately are brought together, and the overall resistance for the evaporating section (R^e) is found as follows:

$$R^e = \left[\frac{1}{R_{fb}^e + R_f^e + R_{tf}^e} + \frac{1}{R_{gb}^e + R_{g,l}^e + R_{gf}^e} \right]^{-1} \tag{2.33}$$

Figure 2.7: Electrical analogy of the thermal resistance network at an evaporating section

2.4.2.2 Thermal Resistance Model for Condensing Section

To calculate the overall equivalent resistance at an evaporating cross sectional slice (R^c), a one-dimensional thermal resistance network similar to the one established in Section 2.4.2.1 is generated for the condensing cross section between the base temperature at the condensing region (T_b^c) and the vapor temperature (T_v). In addition to resistances that are introduced in the Section 2.4.2.1, resistance due to condensation of the working fluid at the fin top (R_{ft}^c) is added to thermal resistance network. Figure 2.8 shows locations and relations of the resistances that occur in the condensing cross section.
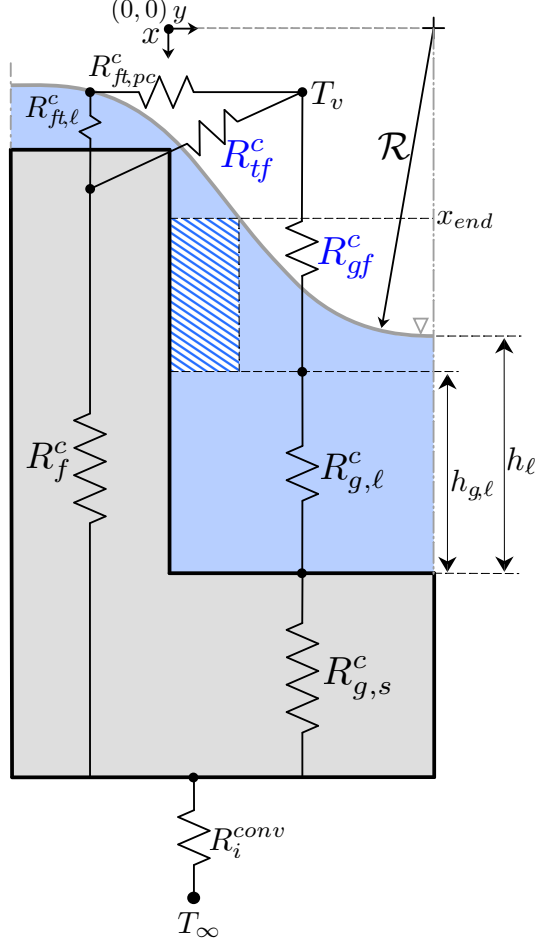
Figure 2.8: Schematic representation of the thermal resistance network at an condensing section

While calculating the resistances at the fin (R_f^c), the solid ($R_{g,s}^c$), and the liquid in the groove ($R_{g,l}^c$), an approach identical to the one used in Eqs. (2.19–2.21) is applied, and resistances per unit length are calculated as follows:

$$R_f^c = \frac{h_b + h_f - 0.5(x_m - x_0)}{k_s(0.5w_f)} \tag{2.34}$$

$$R_{g,s}^c = \frac{h_b}{k_s(0.5w_g)} \tag{2.35}$$

$$R_{g,l}^c = \frac{h_{g,l}}{k_l(0.5w_g)} \tag{2.36}$$

The additional resistance at the fin top (R_{ft}^c) due to condensation of liquid is calculated by using film thickness that occurs at the top of the fin. To calculate the variation of the film thickness on the top of the fins at condenser, a 4th order polynomial approach (Eqn. 2.37) that was proposed in [76] is adopted to this model.

$$\delta(u) = c_0 + c_1 \left(u - \frac{w_f}{2}\right) + c_2 \left(u - \frac{w_f}{2}\right)^2 + c_3 \left(u - \frac{w_f}{2}\right)^3 + c_4 \left(u - \frac{w_f}{2}\right)^4 \quad (2.37)$$

The coordinate system that is defined for the film thickness variation on the fin top is introduced in Figure 2.8, and the constants (c_1, c_2, c_3, and c_4) are calculated subject to the following boundary conditions:

$$\frac{d\delta}{du} = 0 \quad \text{at} \quad u = 0 \quad (2.38a)$$

$$\frac{d^3\delta}{du^3} = 0 \quad \text{at} \quad u = 0 \quad (2.38b)$$

$$\frac{d\delta}{du} = -\tan(\pi/2 - \Theta) \quad \text{at} \quad u = \frac{w_f}{2} \quad (2.38c)$$

$$\frac{d^2\delta}{du^2} = 0 \quad \text{at} \quad u = \frac{w_f}{2} \quad (2.38d)$$

Then, the 4th order polynomial (Eqn. 2.37) is solved subject to the boundary conditions (Eqns 2.38a–2.38d), and the coefficients (c_1–c_4) are calculated as follows:

$$c_1 = -\tan(\pi/2 - \Theta) \quad (2.39a)$$

$$c_2 = 0 \quad (2.39b)$$

$$c_3 = \frac{2c_1}{w_f^2} \quad (2.39c)$$

$$c_4 = \frac{4c_1}{w_f^3} \tag{2.39d}$$

The remaining constant c_0 is the minimum value of the film thickness that occurs at the corner of the fin top, and the total mass flow from this region is equal to the total condensation mass at the fin top. To calculate c_0, condensation mass flux calculation from kinetic theory that is introduced in Eqn. 2.40 is used.

$$\frac{\sigma}{3\nu}\frac{d}{du}\left(\delta^3\frac{d^3\delta}{du^3}\right) = -\frac{a(T_w - T_v) + b(P_l - P_v)}{1 + a\delta h_{lv}/k_l} \tag{2.40}$$

where h_{lv} is the latent heat of vaporization and k_l is the thermal conductivity of the liquid. Integration of the left hand side of the Eqn. 2.40 gives the total mass flow, and it is calculated as:

$$m'_{condensation} = \frac{\sigma}{3\nu}6c_0^3 c_3 \tag{2.41}$$

However, right hand side of the Eqn. 2.40 can not be calculated analytically. Therefore, an iterative procedure is applied the Eqn 2.42 to calculate the c_0.

$$f = \frac{\sigma}{3\nu}6c_0^3 c_3 + \int_0^{w_f/2}\frac{a(T_w - T_v) + b(P_l - P_v)}{1 + a\delta h_{lv}/k_l}du \tag{2.42}$$

Condensation resistance that is occurred at the fin top of the condensation region (R_{ft}^c) is connected to the resistance at the thin film region (R_{tf}^c) in parallel. Therefore, fin top resistance (R_{ft}^c) reduces the overall resistance in the condensing region, and it should be calculated accurately. Thus, dividing the fin top region into discrete finite sections that is applied in the thin film and the groove film regions for the thermal resistance calculation of the evaporating region is also applied to the calculation of the fin top resistance (R_{ft}^c). Figure 2.9 illustrates the schematic representation of the fin top resistance network at the condensing region. To calculate fin top resistance (R_{ft}^c), thin film region is divided discrete finite sections, and each section has two resistances that are resistance due to liquid ($R_{ft,l}^c$) and phase change resistance at the liquid surface ($R_{ft,pc}^c$).
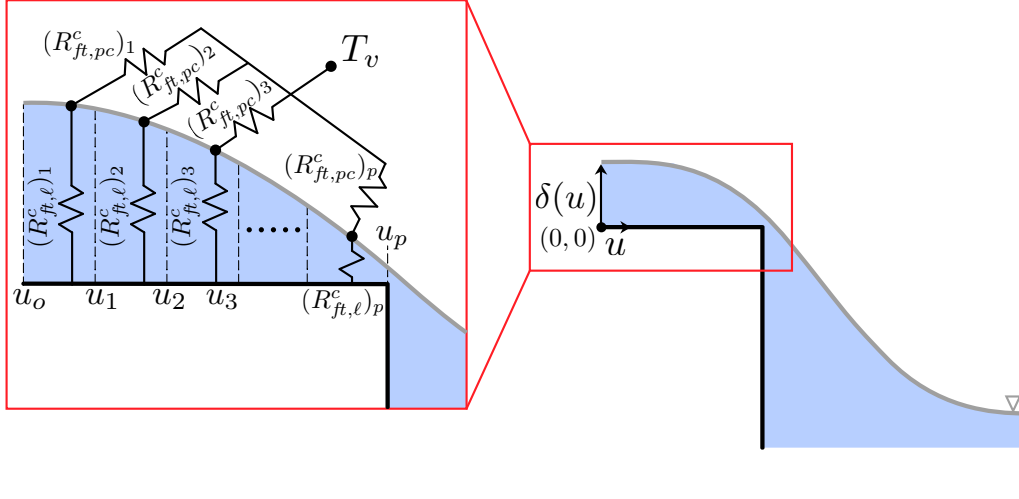
Figure 2.9: Schematic representation of the thermal resistance network at the fin top of a condensing section

Then, the resistances $R^c_{ft,l}$ and $R^c_{ft,pc}$ are calculated by using an approach similar to the one used to calculate R^e_{tf} and R^e_{gf} in the Section 2.4.2.1.

$$(R^c_{ft,l})_n = \frac{\bar{\delta}_n}{k_l(u_n - u_{n-1})} \tag{2.43}$$

$$(R^c_{ft,pc})_n = \frac{1}{ah_{fg}(s_n - s_{n-1})} \tag{2.44}$$

$$R^c_{tf} = \sum_1^p \left(\frac{1}{(R^c_{ft,l})_n + (R^c_{ft,pc})_n} \right)^{-1} \tag{2.45}$$

The thin film (R^c_{tf}) and the groove film resistances (R^e_{gf}) also occur in the condensing sections (Figure 2.8), and as in the evaporating case, these resistances have both liquid and phase change components. These liquid and phase change resistances are designated by $R^c_{tf,l}$ and $R^c_{tf,pc}$ for the thin film region, and by $R^c_{gf,l}$ and $R^c_{gf,pc}$ for the groove film region. While calculating these film resistances, exactly the same approach that is explained in Figures (2.5 and 2.6) is applied,

and formulated as follows:

$$(R^c_{tf,l})_n = \frac{\bar{\delta}_n}{k_l(x_n - x_{n-1})} \tag{2.46}$$

$$(R^c_{tf,pc})_n = \frac{1}{ah_{fg}(s_n - s_{n-1})} \tag{2.47}$$

$$R^c_{tf} = \sum_1^p \left(\frac{1}{(R^c_{tf,l})_n + (R^c_{tf,pc})_n} \right)^{-1} \tag{2.48}$$

$$(R^c_{gf,l})_n = \frac{\bar{\delta}_{n,g}}{k_l(y_n - y_{n-1})} \tag{2.49}$$

$$(R^c_{gf,pc})_n = \frac{1}{ah_{fg}(s_n - s_{n-1})} \tag{2.50}$$

$$R^c_{gf} = \sum_1^p \left(\frac{1}{(R^c_{gf,l})_n + (R^c_{gf,pc})_n} \right)^{-1} \tag{2.51}$$

Finally, the electrical analogy of the thermal resistance network in the condensing sections is illustrated in Figure 2.10 and the overall resistance for the condensing section (R^c) is calculated as follows:

$$R^c = \left(\frac{1}{R^c_{fb} + R^c_f + (1/R^c_{tf} + 1/R^c_{ft})^{-1}} + \frac{1}{R^c_{gb} + R^c_{g,l} + R^c_{gf}} \right)^{-1} \tag{2.52}$$
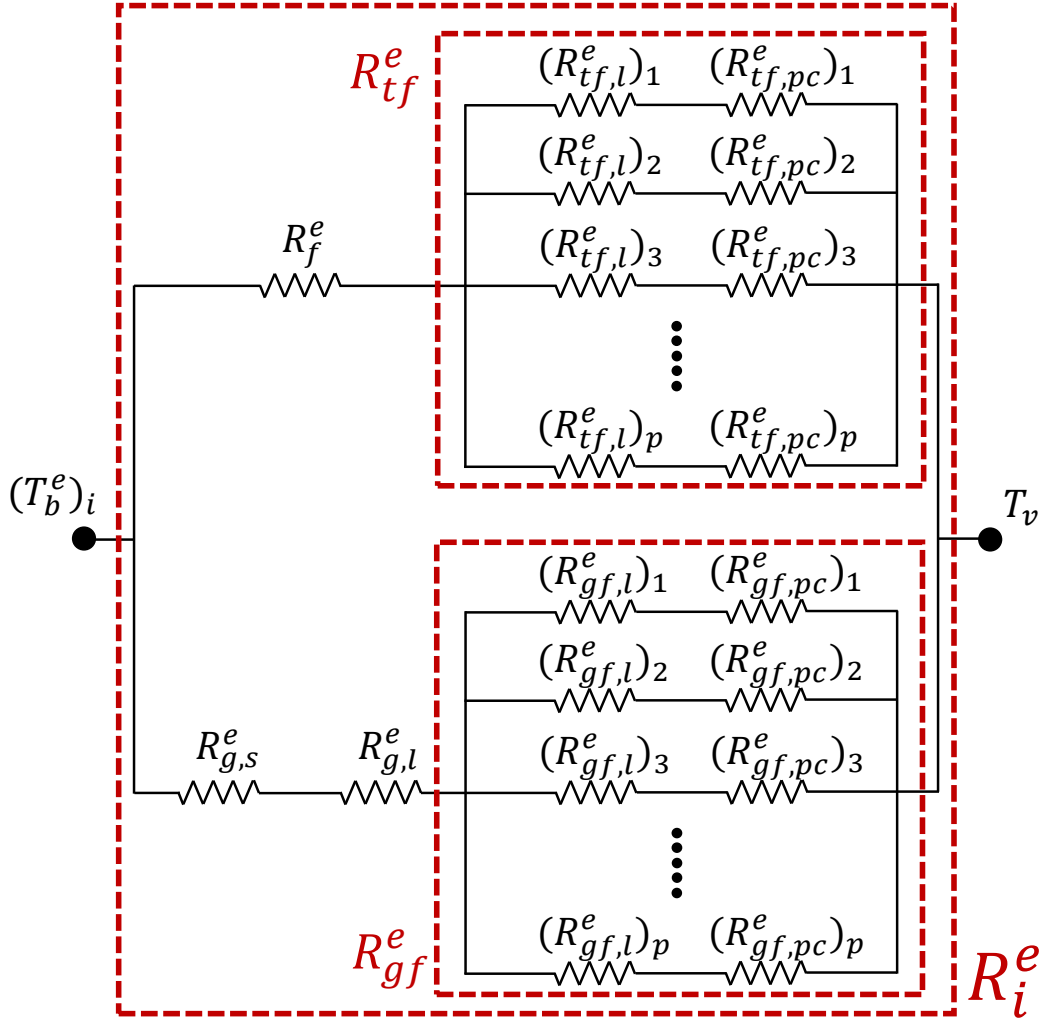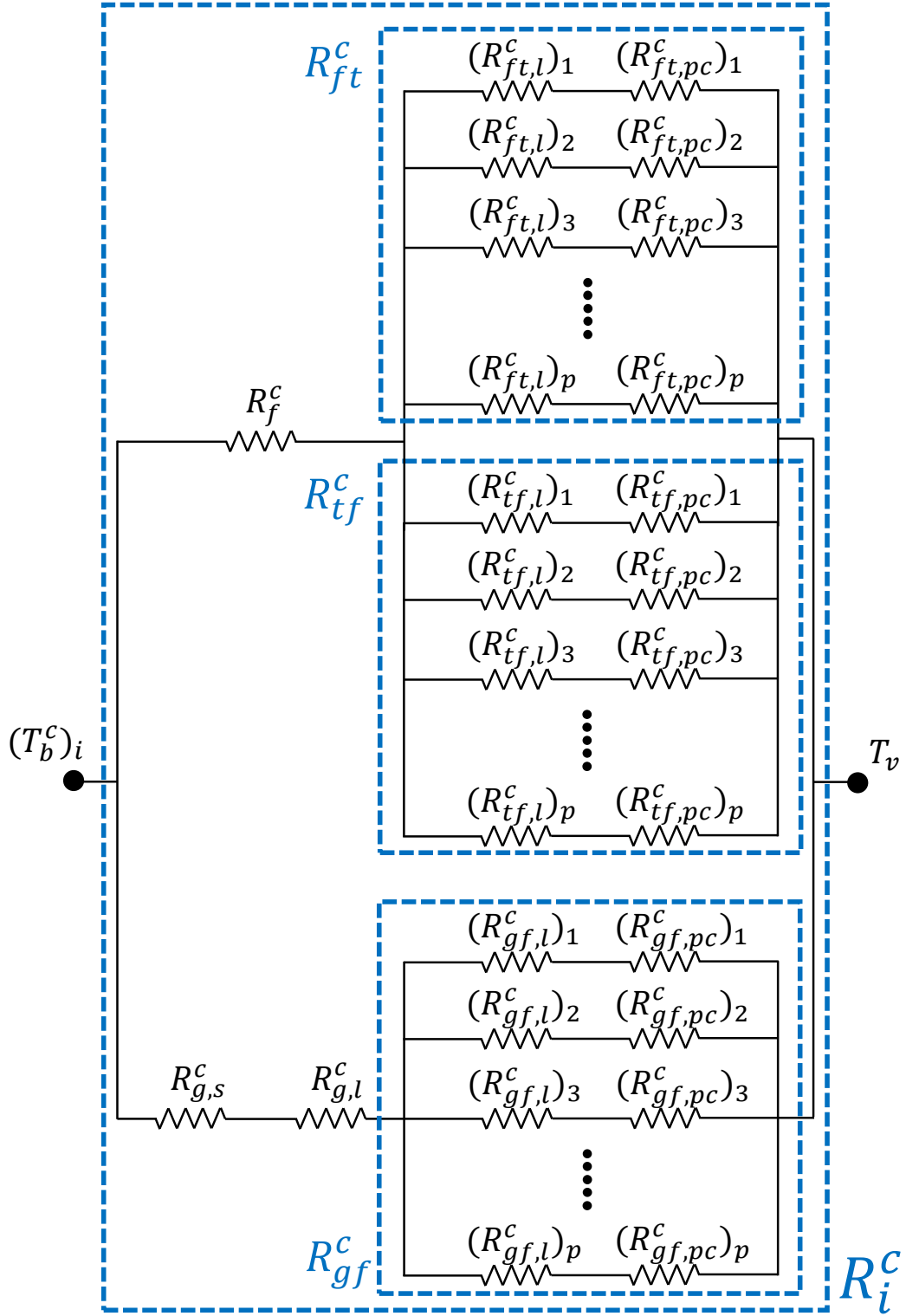
Figure 2.10: Electrical analogy of the thermal resistance network at a condensing section

2.4.2.3 Thermal Resistance Model of Axial Conduction

The only remaining resistance for the complete thermal model that is introduced in Figures (2.1 and 2.2) is the resistance that exists along the heat pipe, namely axial resistance (R_{ax}). While calculating the axial resistance, only the solid is accounted for in the resistance calculations since the thermal conductivity of the solid is much larger than the liquid. Higher conductivity means lower thermal resistance; therefore, the effect of thermal resistance due to the the liquid is not included.

Axial resistance is calculated based on the details of the geometric parameters of the groove (Figure 2.11). In addition to the groove details, if the heat pipe has structures such as side walls that would affect the conduction heat transfer, these structures are also included to the thermal resistance calculation.
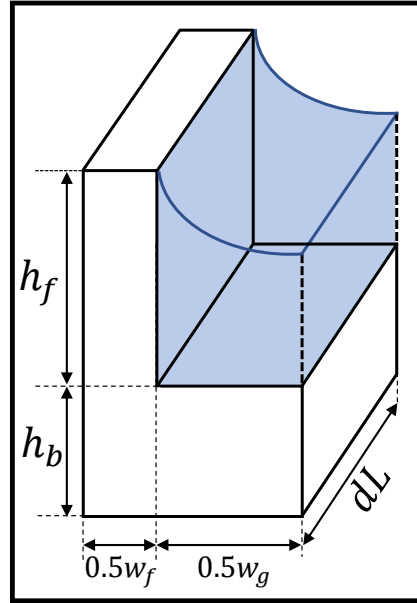
Figure 2.11: Dimensional parameters of an axial conduction thermal resistance

Finally, axial thermal conduction resistance per unit length is expressed as:

$$R_{ax} = \frac{1}{0.5k_s(w_f(h_b + h_f) + w_g h_b)} \tag{2.53}$$

47

2.5 Numerical Model Validation

In this section of the present study, the numerical model for grooved heat pipes will be compared to previous studies for validation. The numerical model that is developed in the present study calculates the radius of curvature along the heat pipe. The first study that is used for the validation is Lefèvre *et al.* [83] because of their ability to measure radius of curvature with confocal microscopy in a rectangular groove with constant cross section. The second study was also conducted by Lefèvre *et al.* [102], and unlike [83], a heat pipe with a rectangular groove with variable cross section was studied. Finally, experimental results of the overall thermal resistance for grooved heat pipes that were reported by Hopkins *et al.* [15] will be compared with the numerical model of the present study.

2.5.1 Results for straight grooves with constant cross section

Lefèvre *et al.* [83] conducted an experimental and numerical study for the flat plate heat pipe with rectangular grooves with constant cross sectional area throughout the heat pipe. The experimental component included measuring the radius of curvature and temperature distribution along the heat pipe for three different heat fluxes: 0.5 W/cm^2, 0.7 W/cm^2 and 0.9 W/cm^2. The numerical part included coupled solution of mass and momentum equations in both liquid and vapor domains together with Young-Laplace equation and a multi-directional thermal resistance network.

Physical properties in Table 2.1 are implemented to the numerical model and solved with the geometric function derived for the rectangular groove (Eqn. 2.16). Since groove width and groove height are constant along the heat pipe, $w(z)$ and $h(z)$ are, w and h as specified in Table 2.1, during the calculation of pressure variation based on the Eqns. 2.18a, 2.18b, and 2.18c. Simulations are conducted for both the two-node (see Figure 2.1) and the multi-slice (see Figure 2.2) thermal resistance models, and are repeated for all three heat fluxes (0.5 W/cm^2, 0.7 W/cm^2, and 0.9 W/cm^2) at 70°C vapor (working) temperature and com-

48

pared with both experimental and numerical results of [83].

Table 2.1: Physical dimensions of the heat pipe in the [83]

Heat pipe material	Copper
Working fluid	Methanol
Evaporator length (mm)	190
Adiabatic length (mm)	10
Condenser length (mm)	30
Total length (mm)	230
Groove height (mm)	0.38
Groove width (mm)	0.4
Fin width (mm)	0.4
Base thickness (mm)	2
Vapor (Working) temperature (°C)	70

Then, the numerical model calculates the pressure variation and the temperature distribution along the heat pipe by using the solution procedure that is introduced in Figure 2.3. According to this solution procedure, either the condenser or the ambient temperatures are specified at the beginning of the simulations to calculate temperature dependent thermo-physical properties. However, Lefèvre *et al.* [83] kept the vapor (working) temperature constant throughout their experimental and in the numerical studies for all heat fluxes. Therefore, the cooling conditions of the current numerical model are used to give the specified vapor (working) temperature of [83] which is 70°C.
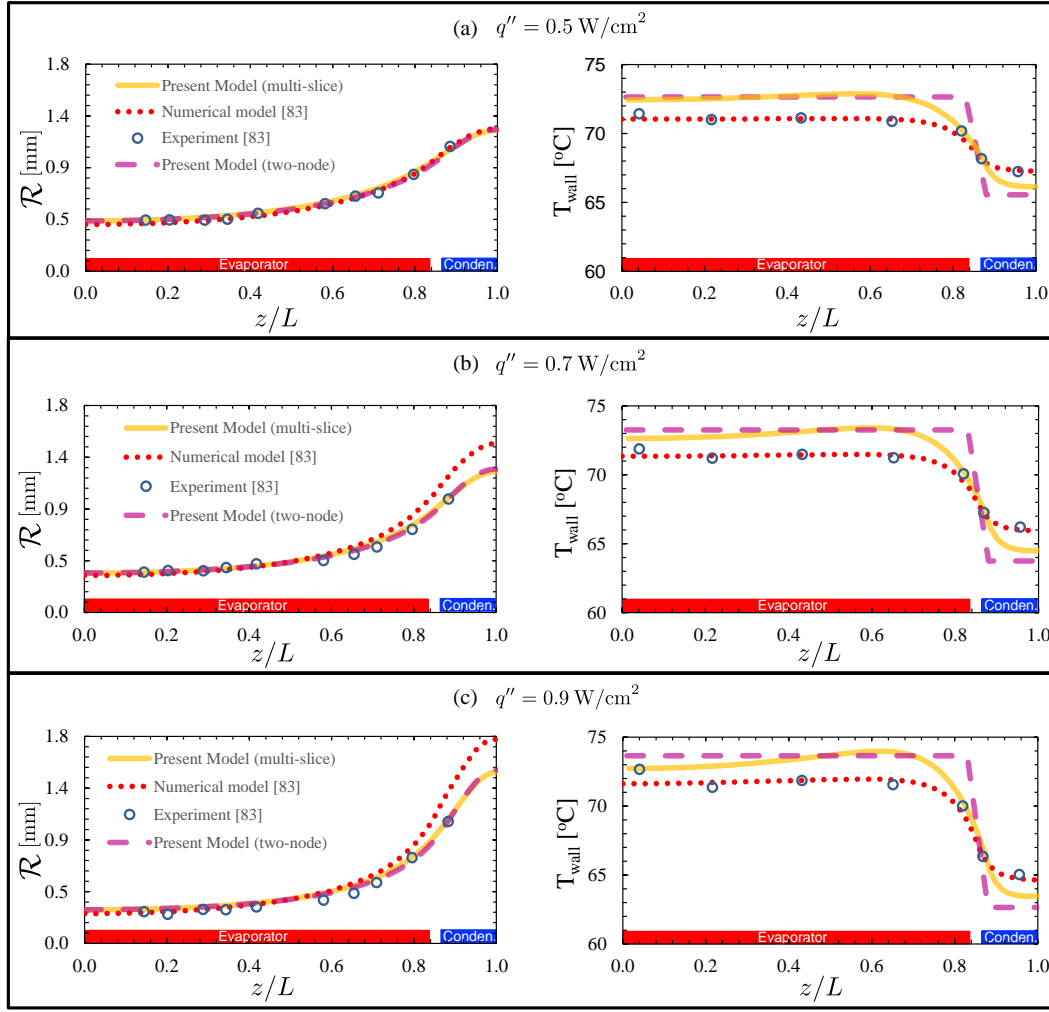
Figure 2.12: Radius of curvature and wall temperature as a function of non-dimensional axial distance: **(a)** $q'' = 0.5$ W/cm^2, **(b)** $q'' = 0.7$ W/cm^2, **(c)** $q'' = 0.9$ W/cm^2.

After calculating the pressure variation along the heat pipe, radius of curvatures are calculated via the Young-Laplace equation and pressure distributions for three different heat fluxes. Figure 2.12 shows the variation of the radius of curvature and the temperature distributions along the heat pipe. Blue dots show experimental results [83] measured with thermocouples and a confocal microscope, for the temperature distribution and the radius of curvature, respectively. Red dotted lines indicate numerical results of [83]. In addition, yellow lines and purple dots show the calculated results of the current study; in which yellow lines refer the results of multi-slices thermal model and purple dots re-

50

fer the results of two-node thermal model. Since the two-node thermal network model consists of only evaporator, condenser and vapor (working) temperatures, evaporator and condenser temperatures are assumed to be constant along their corresponding regions. At the adiabatic region, a linear temperature variation is assumed between evaporator and condenser temperatures. Left column indicates the variation of the radius of curvature, whereas right column indicates the variation of the wall temperature.

The variation of radius of curvature estimation of the current model along the heat pipe for all heat flux combinations are in good agreement with experiments. Moreover, Figure 2.12 shows that the numerical model simulates the experimental results of [83] more precisely for radii of curvature especially in the condenser and the adiabatic regions compared with the results of the numerical model of [83].

On the other hand, the numerical model estimates the results of the temperature distribution along the heat pipe approximately 1°C higher at the evaporator and 1°C lower at the condenser compared to both the experimental and the numerical results of [83] for all three heat fluxes at the 70°C vapor (working) temperature. The reason of the differences between the current study and the study of Lefèvre *et al.* [83] is attributed to the 4th order polynomial approximation to calculate film thickness that occurs at the top of the fin (see Eqn. 2.37), which will be discussed in Chapter 5.

2.5.2 Results for straight grooves with variable cross section

Lefèvre *et al.* [102] conducted an experimental study for the flat plate heat pipe with rectangular grooves with variable cross sectional area. The heat pipe was made of silicon wafer and the working fluid was methanol. The heat pipe was tested for five different heat fluxes; however, measurements for the radius of curvature along the heat pipe were obtained for 4.4 W/cm^2, 6.4 W/cm^2 and 8.4 W/cm^2 using confocal microscopy. Authors stated that there were no studies (either experimental or numerical) in the existing heat pipe literature to compare their results.

Table 2.2: Physical properties of heat pipe in [102]

Heat pipe material	Silicon
Working fluid	Methanol
Evaporator length (mm)	5.6
Adiabatic length (mm)	10
Condenser length (mm)	16.4
Total length (mm)	25
Groove height (mm)	0.2
Groove width variation (mm)	$0.11 \rightarrow 0.67$
Base thickness (mm)	0.325
Vapor (Working) temperature (°C)	30

The numerical model developed in this thesis has the ability to simulate straight rectangular grooves with variable cross sectional area by inserting correct relations for the variation of the width, $w(z)$, and height, $h(z)$, of the groove along the heat pipe axis. Since the height of the groove is constant along the heat pipe, $h(z)$ is replaced with h as specified in Table 2.2. However, the width varies linearly along the heat pipe. Therefore, the linear variation of the width is formulated as $w(z) = w_1 + w_2 z$ where w_1 and w_2 are constants. For the specific case of [102], $w_1 = 1.1 \times 10^{-4}$ m and $w_2 = 2.43 \times 10^{-2}$ m.

Lefèvre *et al.* [102] measured the vapor (working) temperature during experiments which was a constant at 30°C for all heat fluxes. Therefore, the cooling conditions of the current numerical model are used to give the specified vapor (working) temperature, 30°C, similar to the previous section, to simulate the heat pipe in [83].

Simulations are repeated using constant groove height, h, and the linear variation of width, $w(z)$, for three different heat fluxes (4.4 W/cm^2, 6.4 W/cm^2 and 8.4 W/cm^2). The thermophysical properties used in these simulations are presented in Table 2.2. The radius of curvature predictions of the current study along the heat pipe are compared with the experimental results of [102].

Figure 2.13 shows the variations of the radius of curvature along the heat pipe at vapor temperature 30°C for three different heat fluxes. Blue line shows the ratio of the cross sectional area along the groove of the heat pipe to the area at the beginning of the evaporator. Blue dots are the experimental results of [102] measured using confocal microscopy. Yellow lines indicate the calculated radius of curvatures along the heat pipe of the current approach. Results shows that the numerical model simulates the experimental results of [102] sufficiently accurate for the rectangular grooves with variable cross sectional area.
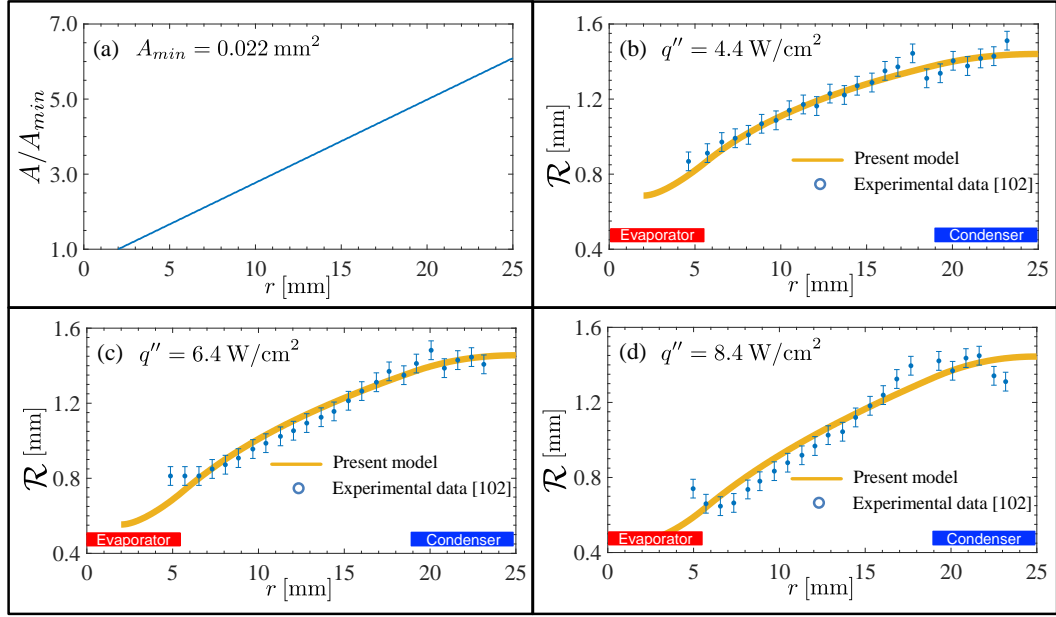
Figure 2.13: **(a)** cross sectional area variation in the grooves and radius of curvature variation along the non-dimensional axial distance: **(b)** $q'' = 4.4 \text{ W/cm}^2$, **(c)** $q'' = 6.4 \text{ W/cm}^2$, **(d)** $q'' = 8.4 \text{ W/cm}^2$.

2.5.3 Results for straight grooves for different heat loads

Hopkins *et al.* [15] conducted an experimental study for three different heat pipes. Two of them had trapezoidal grooves and the last one had rectangular grooves. These heat pipes were tested for 15 different heat loads between 3 W and 127 W, and overall thermal resistances were reported. The overall thermal resistance was calculated by dividing the temperature difference between the two ends of the heat pipe by the total heat input. Since the numerical model that is

developed in the present study simulates the thermal performance of heat pipes with rectangular grooves accurately, a comparison is presented with the thermal resistance results of the rectangular grooved heat pipe in [15]. Table 2.3 shows the physical properties of this rectangular grooved heat pipe.

Table 2.3: Physical properties of heat pipe in the [15]

Heat pipe material	Copper
Working fluid	Water
Evaporator length (mm)	15.6
Adiabatic length (mm)	70.0
Condenser length (mm)	34.4
Total length (mm)	120
Groove height (mm)	0.42
Groove width (mm)	0.12
Fin width (mm)	0.1
Base thickness (mm)	3.4
Vapor (Working) temperature (°C)	90

Hopkins *et al.* [15] reported that the thermal resistance of the heat pipe was high at low heat loads because of the thick liquid film at the evaporator. When the thickness of the liquid film decreased with increasing heat loads, the thermal resistance also decreased. After a certain heat load, the thermal resistance reached its minimum value, and remained constant afterwards.

Figure 2.14 shows the comparison between the experimental results of [15] and the present study. Results of the comparison shows that the predictions of the numerical model of the variation of the thermal resistance for different heat loads are highly accurate. In addition, it can be said that the numerical model of the current study has the ability of simulating the variation of the liquid film thickness for different heat loads.
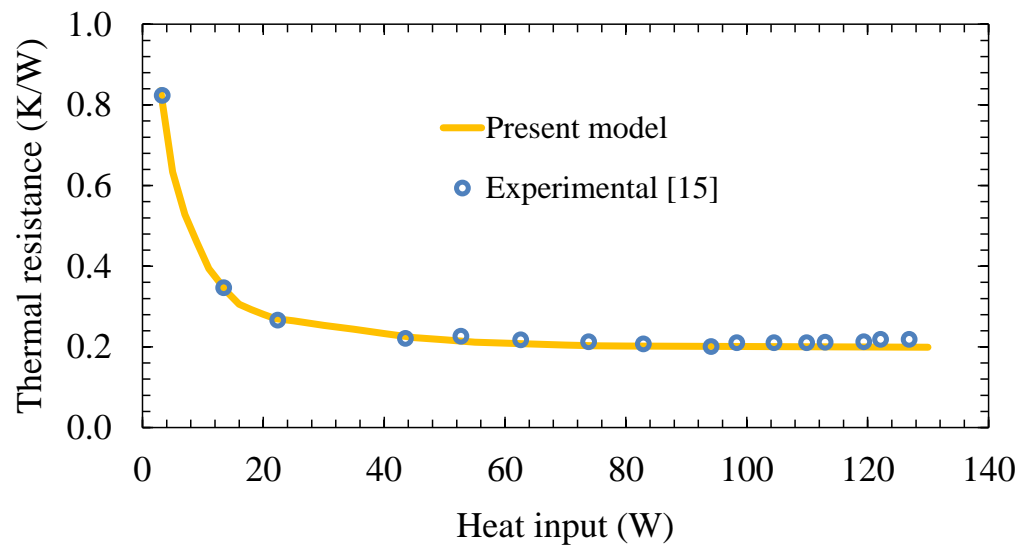
Figure 2.14: Comparison of the results of [15] and the present study for the variation of thermal resistances as a function of heat load.

CHAPTER 3

EXPERIMENTATION

3.1 Design of the Experimental Setup

The design of the experimental setup begins with the design of the heat pipe, and the requirements of the setup should be accurately defined at the beginning. In the current study, it is aimed to design a modular heat pipe which can test different configurations rapidly; enable the visualization of the inside of the heat pipe for observing the dryout, pool region, and boiling phenomena; and enable the inject of working fluid after vacuuming the heat pipe.

3.1.1 Overview of experimental heat pipes

The experimental heat pipe assembly consists of five parts, namely the main frame, the groove frame, the top frame, evaporator and condenser (Figure 3.1). The main frame constitutes the body of the heat pipe and other components are fastened to it. It is made of stainless steel because of its corrosion resistance, solidity, and low thermal conductivity. Two very thin holes (0.9 mm in diameter) are drilled at the two ends; one of which is used to evacuate the air in the heat pipe and the other one is used to fill the heat pipe with the working fluid. To enable accurate data acquisition, heat pipes need to be vacuumed properly before filling with the working fluid and leakage should not be allowed. Therefore, Viton o-rings for vacuum application are mounted on the main frame.
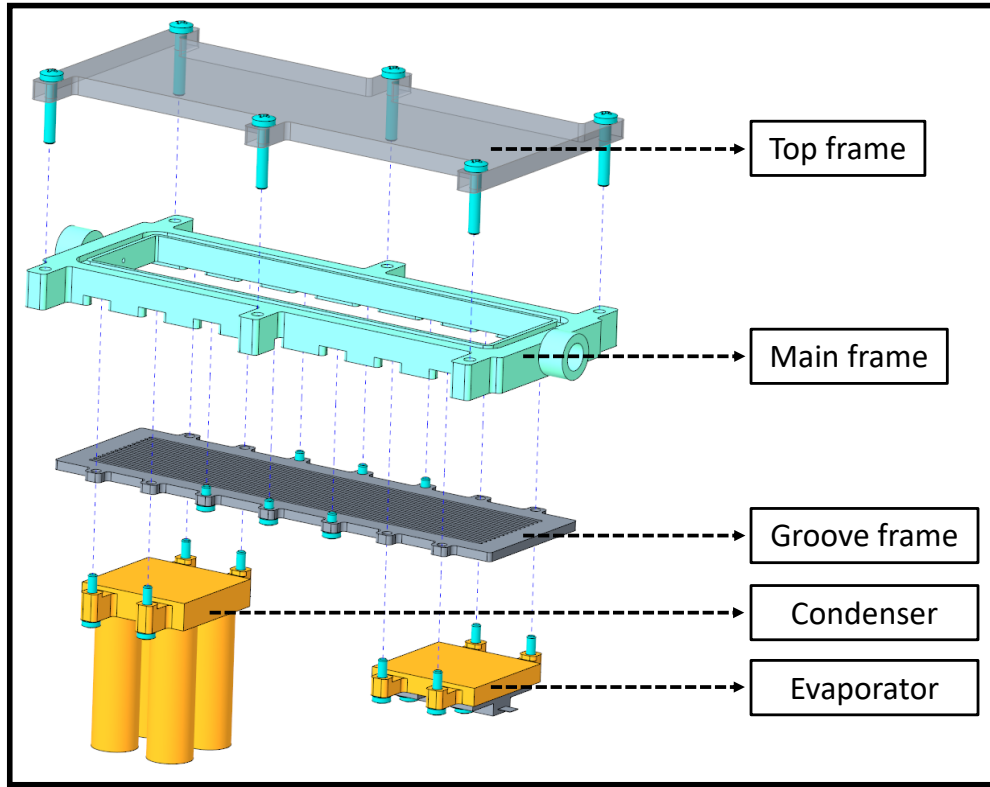
Figure 3.1: Components of the experimental heat pipe

The groove frame houses the wick structure of the heat pipe. Grooves with the desired geometry and density are machined on the heat pipe material (aluminum, copper etc.) to be tested. Thermocouple holes are machined at the bottom of the groove frame from the evaporator to condenser along the centerline of the groove frame. Details of the locations of the thermocouples will be later introduced.

One of the design criteria is that the inside of the heat pipe should be observable while in operation. Therefore, the top frame is made up of acrylic. In addition to being transparent, acrylic has good resistance to both high temperatures and chemicals with low outgassing under vacuum. These characteristics make acrylic the best material for the top frame. Finally, evaporator and condenser are made from copper. Details of the design will be explained in the following section.

All the parts mentioned above are assembled using screws and Figure 3.1 shows the exploded view of the heat pipe. Since all complex manufacturing in designed to be on the main frame which can be used repeatedly with different groove

frames, the modular design aim is achieved. Different heat pipe materials, groove size and groove density can be tested by changing only the groove frame that contains only grooves and thermocouples. Moreover, various sizes of evaporator and condenser lengths can be tested by replacing them with the desired length of evaporator and condenser parts. All this can be realized on a single main frame with ease of assembly of other interchangeable components.

3.1.2 Design of the evaporator and condenser

The heat carried in the heat pipe is discharged from the condenser with the circulating cooling water, and the thermal resistance between the condenser surface and the water is aimed to be kept at a minimum. To obtain a minimum resistance, a highly conductive material —copper— is machined at a desired length and the width of the condenser is equal to the width of the groove frame. The interface with the circulating cooling water is provided with cylinder copper blocks which is connected to the copper base with a highly conductive thermal paste in between (Figure 3.2). Each cylinder block is 5 mm in diameter and 25 mm long.

Evaporator consists of RF resistors that convert the current from the DC power supply to heat without any loss and fluctuations. As the current increases, the losses in the cables used between the power supply and the resistor will increase, so relatively high resistors (with 25 Ω internal resistance) are used in the design. When a longer evaporator length is needed, the desired length is obtained by connecting the resistors in series (Figure 3.2). In order the heat generated in the resistors to be loaded to the heat pipe with a minimum loss, copper selected as the chassis material because of its high thermal conductivity.
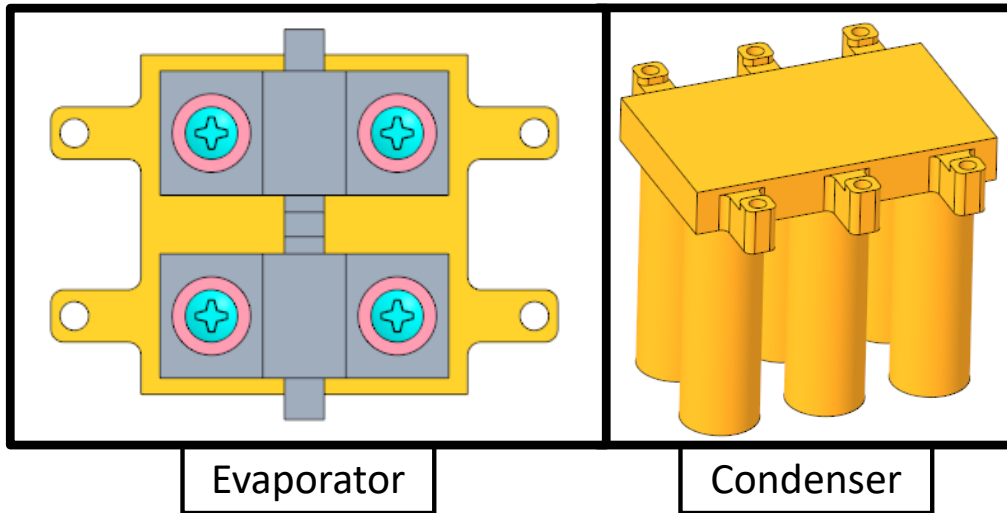
Figure 3.2: Evaporator and condenser units

The numerical model for grooved wicked heat pipes assumes a constant surface flux heat input at the evaporator and convective heat transfer with the constant ambient temperature at the condenser. To simulate the experimental results with the numerical results correctly, the experimental setup should be designed as close to the assumptions. Therefore, several analyses are conducted by a commercial FE code (NX Space System Thermal) to optimize the thickness of the copper base plate for both the evaporator and condenser.

For the evaporator, four different copper thicknesses, namely 1, 2, 3 and 4 mm are analyzed. Heat input is assumed to be 10 W/cm² which is higher than the heat fluxes that can be carried with the configured heat pipe based to the prediction of the numerical code developed in this thesis. The differences between the maximum and the minimum points on the copper base are 2.1 W/cm², 1.1 W/cm², 0.70 W/cm², and 0.49 W/cm² for 1 mm, 2 mm, 3 mm and 4 mm copper thicknesses, respectively (Figure 3.3). The difference between the maximum and the minimum points on the copper base decreases when the thickness of the copper plate increases. However, the more base thickness means the larger heat loses from sides of the copper base. Therefore, 4 mm copper thickness is proper for the evaporator.
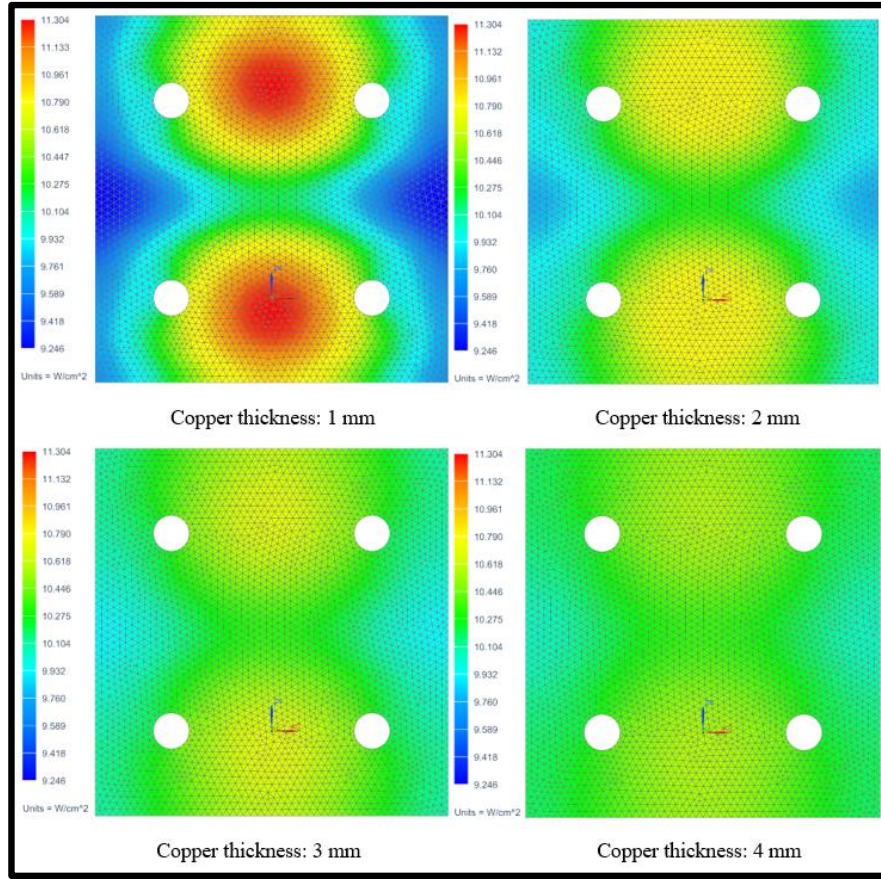
Figure 3.3: Heat flux variations at the evaporator for 1 mm, 2 mm, 3 mm and 4 mm thick copper base plates

For condenser, on the other hand, six base plates with copper thicknesses of 1, 2, 3, 4, 5 and 6 mm are analyzed. Heat input is again taken as 10 W/cm². The differences between the maximum and the minimum points on the copper base are 5.3°C, 2.8°C, 1.8°C, 1.2°C, 0.90°C and 0.68°C for 1 mm, 2 mm, 3 mm, 4 mm, 5 mm and 6 mm copper thicknesses, respectively (Figure 3.4). Thickness of the copper plate directly affects the temperature difference between the maximum and the minimum points on the copper base. Since heat loss from the sides of the copper plate is negligible at the condenser, 6 mm is chosen as a proper base plate thickness for the uniformity of the temperature distribution.
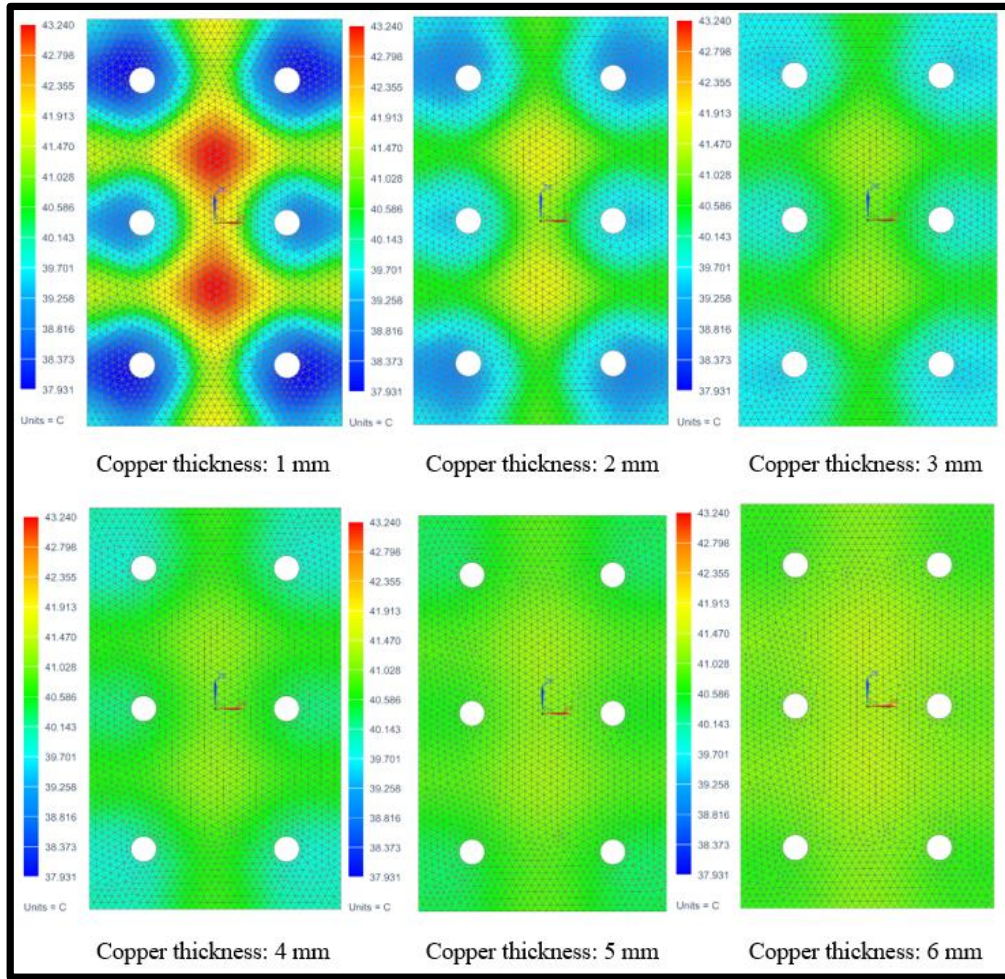
Figure 3.4: Temperature vatiations at the condenser for 1 mm, 2 mm, 3 mm, 4 mm, 5 mm and 6 mm thick copper base plates

3.2 Design and Construction of the Auxiliary Components

3.2.1 Vacuum chambers

Trapped or dissolved gas is released under vacuum conditions, and this phenomenon is called *outgassing* that increases the system pressure and renders the working fluid a mixture. Inappropriate vacuum which is one of the consequences of outgassing which has negative effects on heat pipe performance [91].

To overcome the outgassing problem, two vacuum chambers are designed and produced from stainless steel. One of them is for solid materials and the other

one is for working fluids. The aim is exposing all individual components of the experimental setup and working fluid to vacuum a priori. Thus, components and working fluid are expected to release the dissolved gases before the experiments, so that lower and sustainable vacuum levels can be consistently obtained. Figure 3.5 shows the vacuum chambers for fluids and solids. The vacuum chamber for solids is 28 cm in width, 28 cm in length and 20 cm in height. For liquid vacuum chamber, its diameter is 5 cm and its height is 11 cm.

Figure 3.5: Vacuum chambers (a) for fluids and (b) for solids

3.2.2 Thermocouple assembly

Heat pipes transport heat between evaporator and condenser with small temperature differences, and the measurement of temperatures along the heat pipe is necessary to calculate thermal performance. In the current study, nine grooves are machined on the lower surface of the groove frame which are suitable for the thermocouple to fit into. T-type 36 AWG thermocouples are mounted by using 2-component metal epoxy and located along the heat pipe including evaporator and condenser regions (Figure 3.6). The residual epoxy is cleaned after curing is completed and smoothed, so that the level of the lower surface of the groove frame and thermocouple locations would be the same. To read the temperatures from the heat pipe a Keysight 34972A data acquisition system is used.
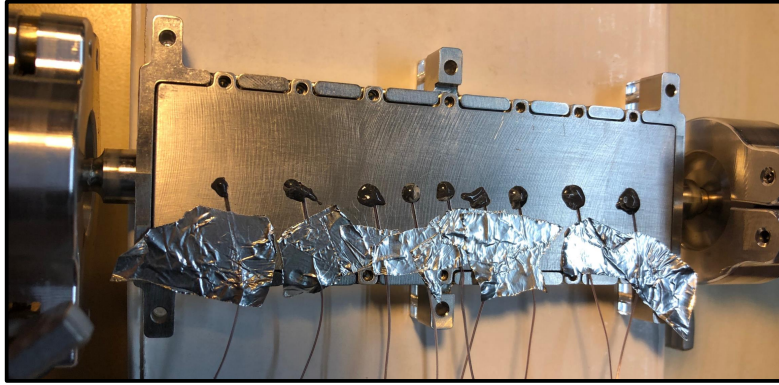
Figure 3.6: Thermocouples under the groove frame of the experimental heat pipe

3.2.3 Evaporator and condenser integration

The last part of the construction for the heat pipe itself is mounting the evaporator and condenser. The interface between the groove frame and copper blocks of evaporator and condenser is solid-to-solid. Therefore, a high thermal resistance exists between them due to surface roughness. To overcome this problem, a thermal interface material is applied while integrating evaporator and condenser (Figure 3.7).
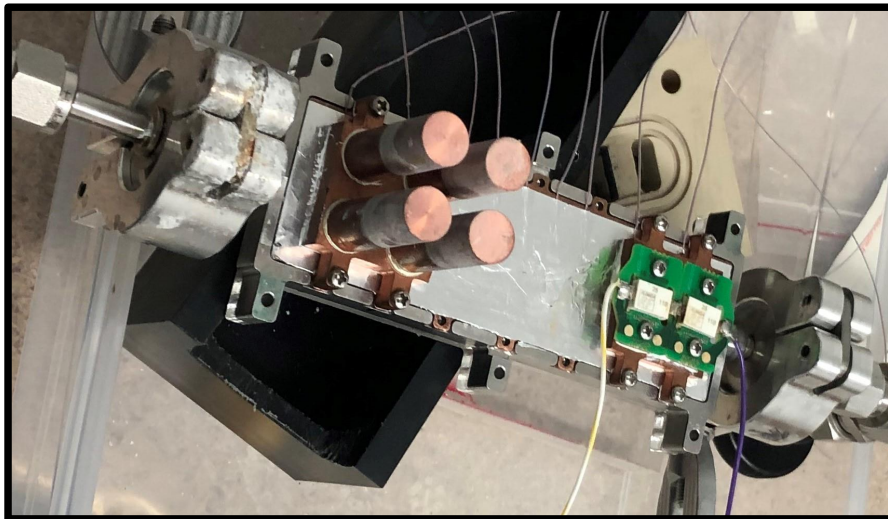
Figure 3.7: Evaporator, condenser and groove frame after integration to the main frame

3.2.4 Heat pipe vacuum system integration

After the heat pipe assembly is completed, it is connected to the vacuum system and the connections between all the test setup elements are completed. All the connections are made with KF16 Viton gaskets and flex pipes which are specifically manufactured for vacuum environment. The flex pipe is bonded to the vacuum pump; and at the other end of this flex pipe, there is a 4-way cross fitting. At one of the ends of this 4-way cross fitting, there is a pressure sensor placed for continuous pressure data acquisition during and after vacuum. The other two ends are connected to the heat pipe and vacuum chambers. Since there are two vacuum chambers, a tee fitting is placed for splitting one flex into two. Figure 3.8 shows the schematic description of the complete experimental setup.
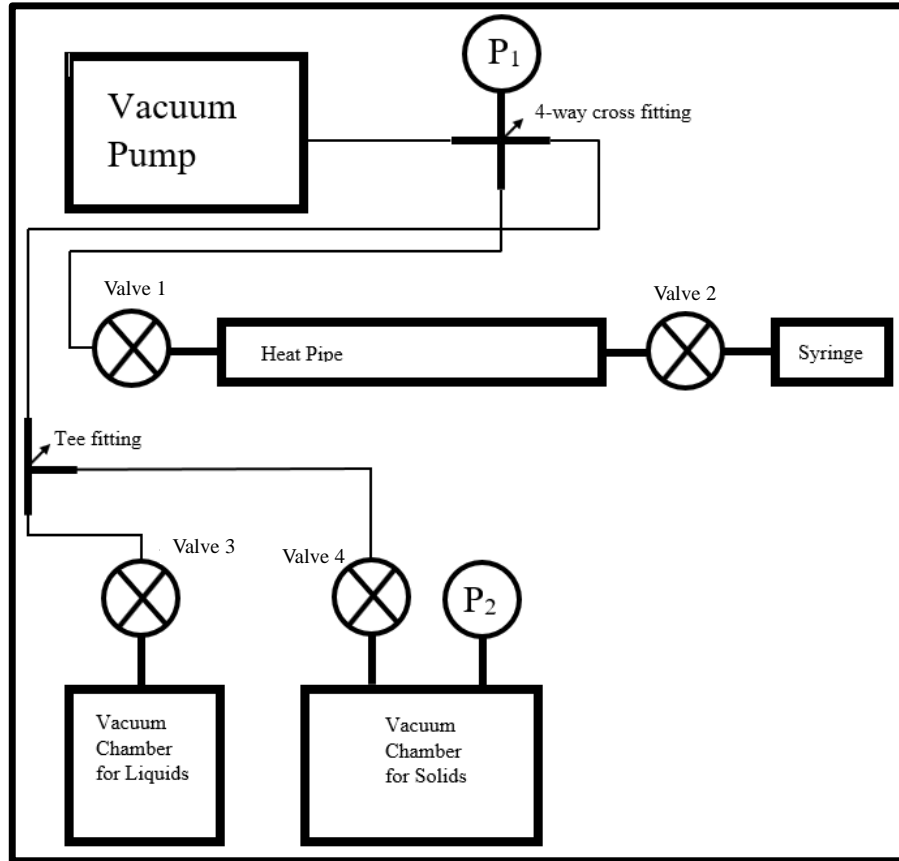
Figure 3.8: Schematic description of experimental setup construction

There are two vacuum chambers in the experimental setup, one of which is

used for degassing the working liquid and the other one for degassing of solids. Vacuum chamber for solids is larger and has more space on the cover —where a pressure gauge and a valve are placed— compared to the vacuum chamber for liquids. Therefore, pressure gauge is not attached to the liquid vacuum chamber due to limited space, but the pressure level is controlled by the pressure gauge at the inlet of the vacuum pump. The pressure inside the vacuum chambers is controlled by valves; and after vacuuming, valves are kept closed during the experiments in order not to affect the rest of the experimental setup.

The last branch of the 4-way cross fitting is connected to the heat pipe itself, and there are two valves at both ends of the heat pipe. Valve-1 and valve-2 are connected to the vacuum line and the charging syringe that contains working fluid, respectively. While vacuuming, valve-2 is closed and valve-1 is opened. After a desired level of vacuum is established, valve-1 is closed. With the opening of valve-2, the heat pipe is filled with the working fluid. Final form of the experimental setup is given in Figure 3.9.
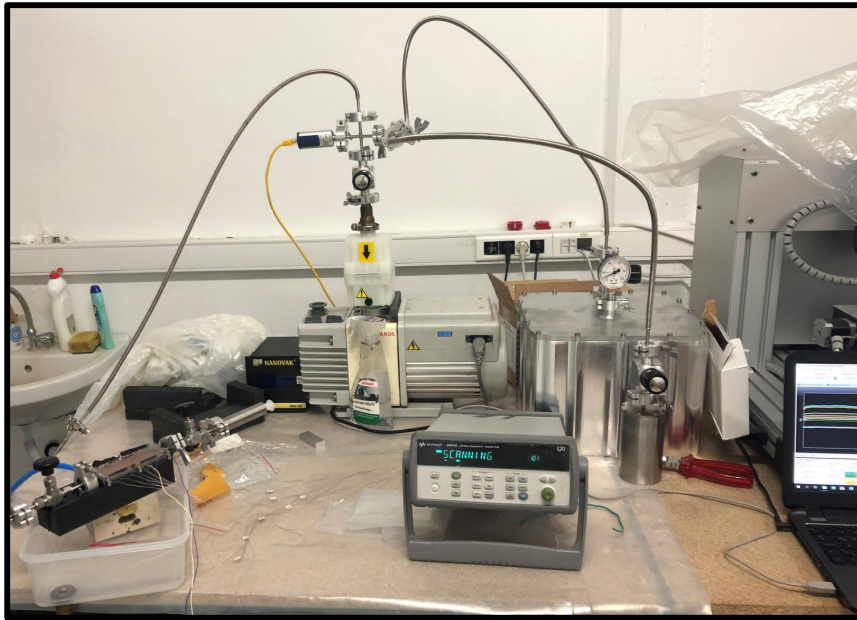
Figure 3.9: Experimental setup with all components connected

3.2.5 Vacuum tightness of the heat pipe

The effects of an inappropriate vacuum were studied in [91], and it was reported that thermal resistance of the heat pipe increases with leakage. Therefore, in the current study, before the heat pipe is filled with the working fluid and the experiments are started, it have been checked whether there is any leakage or not. For this purpose, while valves 2, 3 and 4 are closed, the pressure of the heat pipe and the rest of the system is reduced to 0.03 Torr (4 Pa). After 24 hours, the system pressure is checked. This process is repeated three times and the following results are obtained (Table 3.1). These results indicate that there is a problem with the sealing of the heat pipe or there is a higher outgassing that cannot be covered with vacuum chambers. A fourth trial is made to determine if this increase in pressure is due to outgassing or leakage. In this trial, the waiting time is eight days. At the end of the eight days, pressure became 750 Torr which is atmospheric pressure. Therefore, it is concluded that there is a leakage on this configuration; in other words, vacuum seal is not proper.

Table 3.1: Pressure variation inside the heat pipe

	Initial Pressure (Torr)	Final Pressure (Torr)
1st Trial	0.033	53.6
2nd Trial	0.029	53.0
3rd Trial	0.034	52.7

It is presumed that the leakage might be a the locations where the assembled parts of the heat pipe are joined or the points where the valves are connected to the vacuum line and charging syringe; so, all those points are connected with Viton o-rings and gaskets. After investigating how to achieve a better sealing in o-rings and gaskets, Dow Corning's high vacuum grease is found to solve this problem. Then, all the parts are disassembled, and reassembled by applying the high vacuum grease. The same procedure is repeated to ensure the tightness of the heat pipe, and the following results are obtained (see Table 3.2).

The results show that the source of the leakage in the system is eliminated; but

Table 3.2: Pressure variation inside the heat pipe after applying high vacuum grease

	Initial Pressure (Torr)	Final Pressure (Torr)
1st Trial	0.026	0.55
2nd Trial	0.035	0.46
3rd Trial	0.033	0.24

still, the vacuumed heat pipe is left at the atmospheric pressure for eight days for confirmation and it is observed that the pressure remained below 1 Torr. Thus, the vacuum tightness of the heat pipe is achieved.

3.3 Commissioning of the Experimental Setup

3.3.1 Thermocouple calibration

Before starting the experiments, thermocouple calibration is done to obtain the correct temperature distribution along the heat pipe. For calibration, the heat pipe is kept in an insulated environment for 24 hours without any intervention, during which measurements from thermocouples are collected within 5 minutes with 10-second intervals, and averaged temperature is calculated using the measured values from all thermocouples. This temperature is taken as the reference value, and thermocouples in the rest of the experiments are calibrated according to this reference temperature.

Calibration example for the preliminary experiments of aluminum flat plate heat pipe with IPA can be listed as follows:

$T_1 = T_{ref} - 0.25°C$

$T_2 = T_{ref} - 0.09°C$

$T_3 = T_{ref} + 0.03°C$

$T_4 = T_{ref} + 0.04°C$

$$T_5 = T_{ref} + 0.08°C$$

$$T_6 = T_{ref} + 0.10°C$$

$$T_7 = T_{ref} + 0.16°C$$

$$T_8 = T_{ref} + 0.19°C$$

$$T_9 = T_{ref} + 0.14°C$$

According to manufacturers, uncertainty of the T-type thermocouple is $\pm0.5°C$. After the calibration the accuracy of the temperature difference measurements is estimated to be $\pm0.1°C$.

3.3.2 Charging the heat pipe with working fluid

Before charging the heat pipe with the working liquid, it is necessary to make sure that all the air inside the heat pipe is evacuated and that no air enters the heat pipe during the filling process, for obtaining the maximum performance from the heat pipe. A syringe system is designed and manufactured to ensure that no substances other than working fluid enters the heat pipe (see Figure 3.10). The charging syringe is made of stainless steel and the KF-16 vacuum flange is attached to the outlet.

Figure 3.10: Charging syringe system to fill the heat pipe with working fluid

The steps of the charging procedure of the heat pipe is as follows:

- Syringe is detached the from heat pipe at the flange near the heat pipe body. Simultaneously, the heat pipe is exposed to ambient pressure and is totally dry (i.e., no working fluid or any other substance inside the heat pipe).
- Vane is opened.
- Working fluid that was kept in the vacuum chamber for outgassing is filled into the syringe.
- Vane is closed.
- Since the region between the vane center and the flange is exposed to vacuum, working fluid that remains between vane center and flange is removed from the syringe system.
- Syringe is attached to the heat pipe by using KF-16 flange, Viton o-ring, and high vacuum grease.
- Both the heat pipe and the connections are vacuumed until reaching 0.03 Torr.
- Vane connected to the charging syringe is opened slowly and the heat pipe is filled with the working fluid.

3.3.3 Filling ratio definition, calculation and measurement

Previous studies [90–92] showed that there is an optimum amount of working fluid for the heat pipes to operate at the maximum heat transfer rate with minimum temperature differences. The amount of the working fluid is defined using the filling ratio. In the current study, the filling ratio, ψ, is defined as the proportion of the volume of the working fluid inside the heat pipe to the total groove volume (see Equation 3.1).

$$\psi = \frac{V_l}{V_{tot}} \tag{3.1}$$

The total volume of the heat pipe is calculated easily because height, width, length and total number of grooves in the heat pipe are known. The volume of

the working fluid inside the heat pipe is calculated by using cross section area of the liquid region in the heat pipe and the height of the working fluid inside the heat pipe.

To determine the height of the working fluid, the heat pipe is placed vertical and the level of the working fluid is marked. Then, a caliper is used to measure the height of the working fluid, and multiplication of the height and the cross section resulted in working fluid volume. Moreover, the amount of the liquid in the heat pipe is also obtained with the distance that the syringe system travels horizontally while filling the liquid. In this way, the accuracy of the amount of the liquid in the heat pipe is double checked.

3.3.4   Preliminary experiments

Preliminary experiments are conducted to ensure that the device which is designed and manufactured in the current study operates as a heat pipe. The base material of the heat pipe is aluminum and the working fluid is isopropyl alcohol (IPA). Total length of the heat pipe is 100 mm with 26 mm evaporator and 26 mm condenser regions. At the beginning, two experiments are conducted at 2.1 W/cm^2 (13.7 W). One of these experiments is performed with no IPA (i.e., heat transfer with conduction only), whereas the other one is done with IPA (i.e., heat transfer mechanism is phase change and conduction together) which is charged into the system as explained in the previous section. Filling ratio of the heat pipe was 4.5–5.0.

Figure 3.11 shows the results of these two experiments. The horizontal axis shows the length of the aluminum heat pipe starting from the evaporator, and the vertical axis shows the temperatures measured from the heat pipe. Red and dark blue regions at the horizontal axis indicate evaporator and condenser regions, respectively.
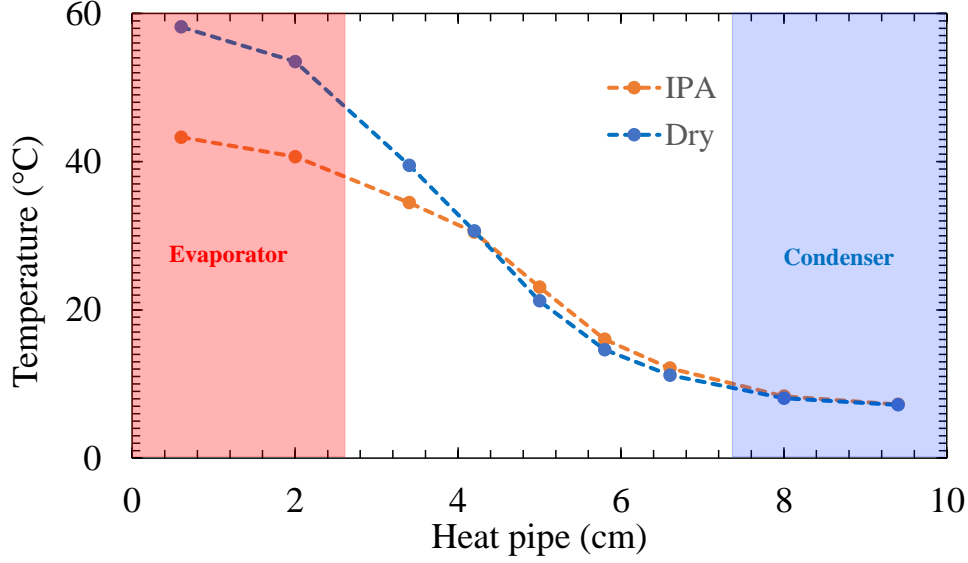
Figure 3.11: Aluminum flat plate heat pipe preliminary experiment

For the aluminum flat plate heat pipe with no IPA, the maximum temperature that is measured at the evaporator is 58.2°C and it decreased to 43.3°C after injecting IPA to the heat pipe by using the syringe system. By doing that, a decrease of 14.9°C was achieved for the maximum temperature. Therefore, it was deduced that the modular heat pipe experimental setup is working. However, the measured temperature for the case with IPA is higher compared to the similar conditions in [57]. Thus, the working condition that is illustrated in Figure 3.11 is not the optimum point for this configuration. In addition, the minimum temperatures which are measured from the condenser in both experiments were equal (i.e., 7.2°C). This is one of the most important outcomes of this experiment because obtaining exactly the same results from condensers indicated that insulation of the experimental setup is proper.

3.3.5 Capillary condensation and the minimum intrusion modification

While conducting preliminary experiments, inconsistent experimental results of the working fluid height in the heat pipe are observed. For example, at the beginning of the experiment, height of the IPA is 25.9 mm. Then, a series

of experiments are conducted on heat fluxes starting from low and increasing. During these experiments, temperature of the evaporator reached 80°C. After completing the series of experiments, IPA height is measured again, and it is found to be 19.0 mm. It was concluded that 6.9 mm (i.e. approximately 1.1 cm^3) IPA disappeared from the heat pipe. However, it is not possible because sealing of the heat pipe is tested, and it is observed that there is no leakage. To understand the vanishing liquid, the heat pipe is cooled with 6°C cooling water which is sufficient to drop the temperature along the heat pipe below the ambient temperature. Then, IPA is measured again, and it is found as 25.8 mm which is approximately the amount measured at the beginning of the experiment.

Our explanation regarding that circumstance is the condensation of IPA between the heat pipe and the valves at two ends of the heat pipe with higher temperature inside it. To overcome this condensation problem, IPA should be retained inside the heat pipe. Therefore, a stainless steel pin shown in Figure 3.12 is designed as a solution to this problem. Dimensions of the pin are found by using dimensions of the gap between the side wall and the valves at the two ends of the heat pipe. Dimensions of the gap are 0.94 mm at side walls and 3.55 mm at valves of the heat pipe. To find the best configuration, five different pins are manufactured and tested (see Table 3.3).

Figure 3.12: Minimum intrusion modification

Table 3.3: Pins manufactured for minimum intrusion modification

Pins No:	Valve Side Diameter (mm)	Wall Side Diameter (mm)
1	3.3	0.7
2	3.4	0.8
3	3.4	0.9
4	3.5	0.8
5	3.5	0.9

The first experiment is conducted by Pin 1, and the insertion of the pin is shown in Figure 3.12. Then, the same filling and the measurement procedures are repeated for this configuration. After heating the heat pipe, the measurement is repeated, and it is found that condensation between the heat pipe and the valves occurred again. Therefore, a reliable filling ratio could not be obtained for Pin 1. Therefore, Pin 1 is replaced by Pin 2, and the filling ratio measurement procedure is repeated. The results show that the filling ratios before and after heating are not equal, but close to each other compared to Pin 1. According to the results of Pin 1 and 2, Pin 3 is tried for a better performance. However, it is noticed that 0.9 mm diameter at the wall side of the pin blocks the aspiration of the liquid from the heat pipe. Therefore, the next experiment is conducted by Pin 4, and the filling ratios before and after heating are equal. In addition, the aspiration of the liquid is completed successfully with Pin 4. These results indicated that condensation problem is solved.

3.3.6 Experiments of copper flat heat pipe to find the optimum point

After solving the condensation problem, sets of experiments are conducted with the flat plate heat pipe to find the optimum working point similar in [57]. The groove frame of the heat pipe is copper and the working fluid in it is IPA. The length of the heat pipe is 100 mm including the evaporator, the adiabatic, and the condenser regions as 26 mm, 48 mm, and 26 mm, respectively. Note that lengths of the evaporator, adiabatic and condenser regions depend on the problem that is managed thermally with heat pipes. The dimensions that is

chosen in this thesis are both have measurable temperature difference according to numerical model and close to electronic components to be thermally managed. In addition, 15 square grooves are machined on the groove frame, and both the height and width of each groove were 0.8 mm.

For recording the temperature from the surface of the heat pipe, nine thermocouple slots are machined under the groove frame with the dimensions of 0.6 mm × 0.6 mm (see Figure 3.13). Then, T-type thermocouples are bonded to these locations using 2-component metal epoxy as explained in Section 3.2.2. The evaporator, the adiabatic and the condenser regions have two, five and two thermocouples, respectively (Figure 3.13).
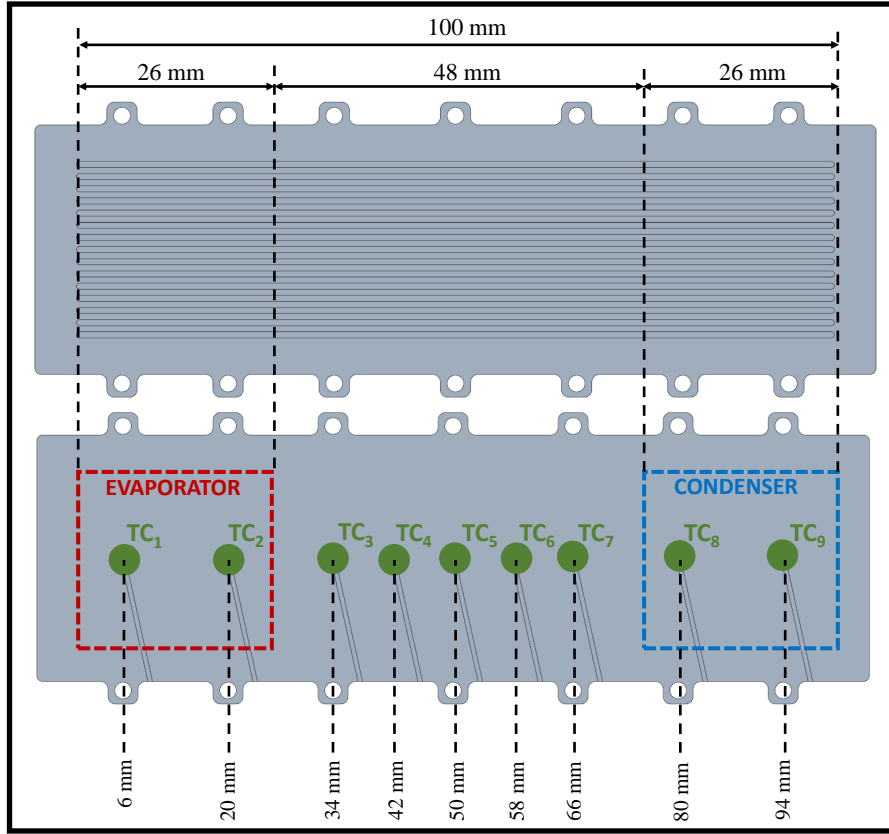
Figure 3.13: Details of the evaporator, adiabatic, condenser regions and the thermocouple locations of the copper flat grooved heat pipe

Then, the air inside the heat pipe is evacuated, and the working fluid IPA is injected into the vacuumed heat pipe until the filling ratio reaches 12.9. After that, the heat pipe is operated for the heat input of 2.1 W/cm^2 (13.7 W) until it

reaches steady state which requires approximately 40 minutes. The same heat input test is repeated 14 times, with some liquid aspirated from the heat pipe each time, effectively reducing the filling ratio. Figure 3.14 shows the results of these experiments. The horizontal axis indicates the filling ratio that was defined in the Section 3.3.3, and the vertical axis specifies the temperature differences at both the adiabatic region and evaporator-condenser regions. Temperature differences are calculated as follows:

$$\Delta T_{ad} = T_7 - T_3 \tag{3.2a}$$

$$\Delta T_{ev-con} = \frac{T_1 + T_2}{2} - \frac{T_8 + T_9}{2} \tag{3.2b}$$
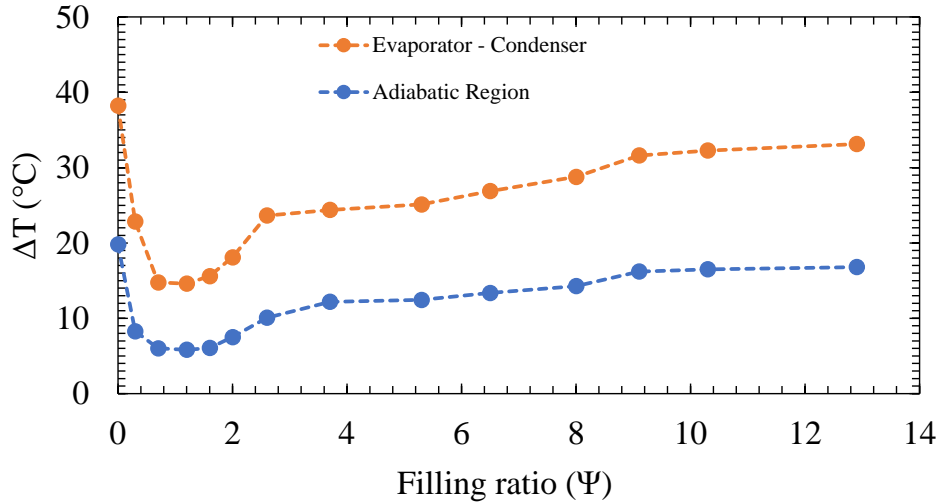
Figure 3.14: Variation of temperature difference at adiabatic and evaporator-condenser regions of copper flat plate heat pipe with filling ratio at 2.1 W/cm^2 (13.7 W) heat load

The results show that the temperature differences first decreases with the amount of fluid aspirated from the system and increases after a certain point. In addition, the temperature change is at its minimum value and remains constant for a certain range (filling ratio is between 0.7 and 1.6). This range reveals the optimum filling ratios of the flat heat pipe for this configuration.

3.4 Validation of the Numerical Model with Current Experiments

The predictions of the numerical model are used to design the experiments in the modular experimental setup of the current study. Therefore, after conducting the experiment for the flat plate heat pipe with rectangular grooves, the results of the simulations are compared to the experimental results to validate the numerical model.

For validation of the numerical model, exactly the same configuration that is tested in the Section 3.3.6 is compared. After assembling the groove frame to the base frame of the experimental setup, the evaporator and the condenser (see Figure 3.2) are mounted to this setup and the thermal interface material is applied to the interfaces between the groove frame and the evaporator, and also between the groove frame and the condenser to prevent the formation of high thermal resistances on these surfaces. The lengths of both the evaporator and the condenser are 26 mm. Since the total length of the groove frame is 100 mm, the adiabatic region becomes 48 mm. The dimensions of the experimental setup are given in Table 3.4.

Table 3.4: Physical properties of heat pipe in the current study

Heat pipe material	Copper
Working fluid	Isopropyl Alcohol (IPA)
Evaporator length (mm)	26
Adiabatic length (mm)	48
Condenser length (mm)	26
Total length (mm)	100
Groove height (mm)	0.8
Groove width (mm)	0.8
Base thickness (mm)	1.2
Number of grooves	15
Heat input (W/cm^2)	2.1

Temperatures from the wall of the groove frame are measured by placing T-type

thermocouples under the groove frame. In order to place the thermocouples, square grooves of 0.6 mm×0.6 mm are machined and thermocouples are attached to the thermocouple grooves by a two-component metal epoxy. The details of the groove frame that was tested are illustrated in Figure 3.13.

The heat pipe—details of which are given above—is tested under 2.1 W/cm^2 heat flux that is provided by the DC power supply. At the beginning of the experiment, the heat pipe is filled with the working fluid, IPA. Then, the heat pipe is operated until it reaches the steady state. After that, some amount of IPA is aspirated from the heat pipe and testing commenced. This procedure is repeated until no IPA remains in the heat pipe. Finally, the minimum temperature difference point that is obtained from these experiments is taken as an optimum working point of the heat pipe.

Figure 3.15-a shows the variation of the wall temperature along the heat pipe. According to the results of the present study, blue dots refer to the experimental results, yellow line is the calculated results using the 100-slice thermal model, and purple dots are calculated results using the two-node thermal model. Since the two-node thermal network model consists of only evaporator, condenser and vapor temperatures, evaporator and condenser temperatures are assumed to be constant in these regions. In the adiabatic region, a linear temperature variation is assumed between evaporator and condenser temperatures. On the other hand, 100-slice thermal model simulates the entire heat pipe including the evaporator, the adiabatic and the condenser regions. Therefore, no assumption is necessary for the results of the 100-slice thermal model. Results indicate that the predictions of both the two-node and the 100-slice thermal models match the results of the experiment.

Figure 3.15-b shows the variation of the radius of curvature along the heat pipe. Yellow line and purple dots are calculated results using 1000-slice and 200-slice flow models respectively. Although the number of slices in one pattern is one-fifth of the other, results indicate that both flow models predict the same radius of curvature along the heat pipe. The experimental setup that is developed in the present study cannot measure the radius of curvature. Therefore, the results

of the radius of curvature in the present numerical models cannot be compared with the experiments.
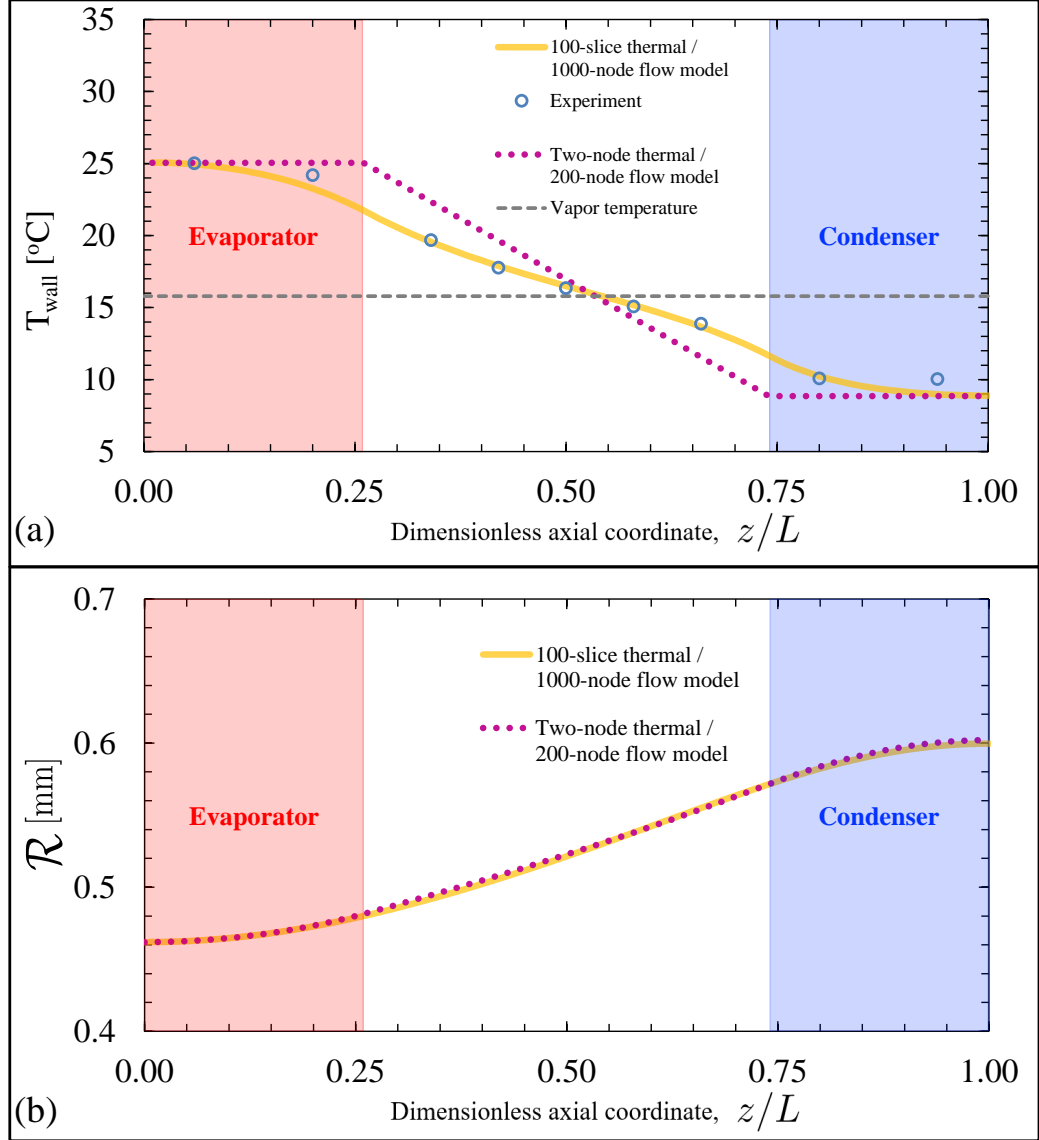
Figure 3.15: Wall temperature of the heat pipe and radius of curvature, $q'' = 2.1$ W/cm^2: **(a)** 100-slice thermal model, two-node thermal model and experimental results **(b)** 200-slice flow model and 1000-slice flow model results.

Note that both two-node thermal/200-slice flow model (2-T/200-F) and 100-slice thermal/1000-slice flow model (100-T/1000F) give the same results in terms of radius of curvature and temperature difference between the two ends of the heat pipe. However, 2-T/200-F cannot simulate the temperature variation along the heat pipe. On the other hand, although 100-T/1000F solves for more unknowns

compared to 2-T/200-F, the computational time is still in the order of seconds. Therefore, in the rest of the study 100-T/1000F (multi-slice thermal resistance network with fluid flow model) is used in simulations.

CHAPTER 4

DEVELOPMENT OF INNOVATIVE GROOVE GEOMETRIES

The capillary pressure which is created by wick structures on the heat pipe walls provides the flow of the condensed liquid from the condenser to the evaporator. Also, by means of the capillary pressure, heat pipes can operate without the necessity of any external force such as gravity or a pump and the pumping force that originates from capillary pressure is called the capillary pumping. Since the driven heat transfer mechanism for the heat pipe is phase change at the evaporator, the liquid flow from the condenser to the evaporator created by the capillary pressure must continue in order for the heat pipe to operate. Therefore, the heat transport capacity of the heat pipe is directly related to the capillary pressure that occurs in the wick structure [15, 30, 84].

The capillary pressure in the grooved heat pipes depends on the groove width, the contact angle between the liquid inside the heat pipe and the solid material at the top of the fin and the surface tension of the liquid so that the capillary pressure can be increased by decreasing the groove width. However, even increased capillary pressure may not be sufficient for the operation of the heat pipe, because there might be an increase in pressure losses in the fluid due to increased friction along the heat pipe with reducing width.

A grooved heat pipe provides the maximum capillary pumping while operating at the onset of the dryout, where the contact angle, θ_{ca}, at the beginning of the evaporator has its minimum value depending on the solid–liquid pair. Under these circumstances, if the heat input is increased, dryout occurs. As a result of dryout, the temperature difference between the evaporator and the condenser increases which means that the heat pipe cannot operate correctly. Briefly, a

81

design with the minimum friction losses and the maximum capillary pumping is required to obtain a high-performance heat pipe.

In this section of the present study, innovative groove geometries will be proposed for thermal performance enhancement. Then, simulations of these proposed geometries will be run by using the numerical model that was developed in the present study, and will be compared with the standard straight groove geometries. Finally, experiments of some of these geometries will be conducted, and compared with the simulations.

4.1 Converging Grooves

The first proposed innovative groove geometry is the rectangular grooves with variable cross section. Grooves with decreasing cross sectional area from the condenser to the evaporator region will be named as converging grooves in this thesis. In addition to converging groove, a standard constant cross section rectangular grooves, namely straight grooves, are also studied in this section for the comparison of thermal performance enhancement. These two grooves are illustrated in Figure 4.1.
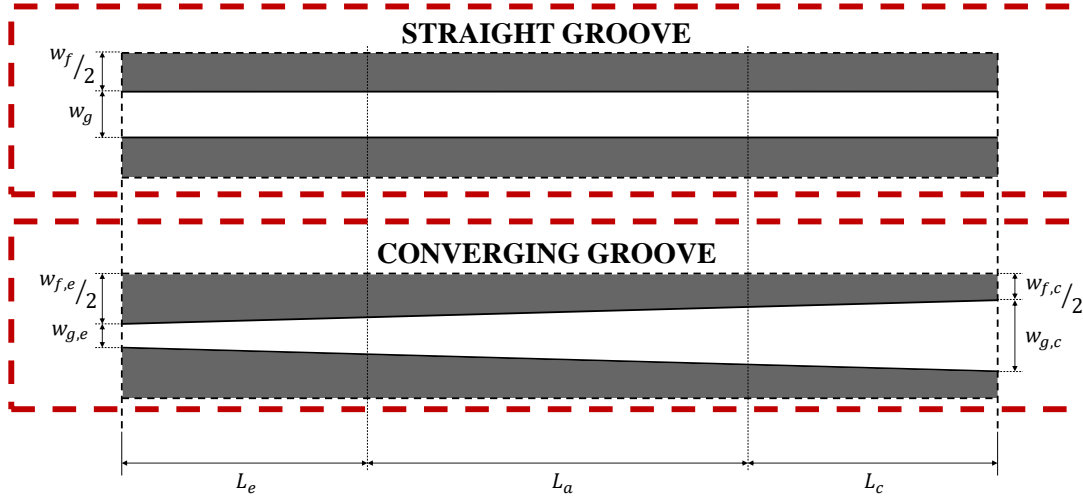
Figure 4.1: Straight and converging groove geometries

The reasoning behind the thermal performance enhancement of a converging groove is the reduction of the groove width from the condenser to the evaporator

region. This reduction provides two benefits: increasing the capillary pumping by decreasing the groove width and decreasing the axial conduction resistance at the evaporator region by increasing the fin width.

4.1.1 Case study for a converging groove

A case study is defined and simulated in order for the characterization of the thermal performance of converging grooves. In this case study, six different heat pipes are simulated. The first heat pipe has straight grooves with 600 μmm groove and fin widths and 400 μmm groove height. The width of these straight grooves is taken as the nominal width of the grooves.

Table 4.1: Details of the dimensions of the simulated heat pipes for the straight and converging grooves

	HP-600	HP-575	HP-550	HP-500	HP-400	HP-300
L_e(mm)	26	26	26	26	26	26
L_a(mm)	48	48	48	48	48	48
L_c(mm)	26	26	26	26	26	26
L_{total}(mm)	100	100	100	100	100	100
W_{hp}(mm)	25	25	25	25	25	25
$w_{g,e}(\mu$m)	600	575	550	500	400	300
$w_{f,e}(\mu$m)	600	625	650	700	800	900
$w_{g,c}(\mu$m)	600	625	650	700	800	900
$w_{f,c}(\mu$m)	600	575	550	500	400	300
$h_g(\mu$m)	400	400	400	400	400	400
h_b(mm)	1.6	1.6	1.6	1.6	1.6	1.6
Groove type	Straight	Conv.	Conv.	Conv.	Conv.	Conv.
# of grooves	19	19	19	19	19	19

The remaining five heat pipes have converging grooves. Widths of these converg-

ing grooves are 4%, 8%, 17%, 33% and 50% less compared to the groove width of the straight grooved heat pipe at the end of the evaporator. On the contrary, widths of these converging grooves are 4%, 8%, 17%, 33% and 50% higher compared to the straight grooved heat pipe at the beginning of the condenser region. Thus, the width of the grooves in the middle of these six heat pipes are equal to each other, which is equal to the nominal groove width. Details of the dimensions of these heat pipes are shown in Table 4.1.

4.1.2 Simulation results for converging grooves

Simulations are run to find the maximum heat transfer capacity of each heat pipe. To calculate the maximum heat transfer capacity, the minimum contact angle throughout the heat pipe is assumed to be the material contact angle between copper and IPA. On the other hand, the maximum contact angle approaches 90° at the condenser. Under these circumstances, the maximum heat carrying capacity of each heat pipe, the pressure differences, the temperature differences, and the thermal resistances that occur while carrying this heat from the evaporator to the condenser region are given in Table 4.2.

Table 4.2: Simulation results of straight and converging grooved heat pipes at their maximum heat loads

	Q(W)	ΔP (Pa)	ΔT (°C)	R (K/W)	Type
HP-600	13.6	61.9	12.5	0.92	Straight
HP-575	13.3	66.4	12.0	0.90	Converging
HP-550	12.6	69.1	11.4	0.91	Converging
HP-500	11.2	75.3	10.2	0.91	Converging
HP-400	7.9	87.1	7.7	0.97	Converging
HP-300	4.4	94.3	5.0	1.13	Converging

The maximum amount of heat that is carried in the straight grooved heat pipe (HP-600) is calculated as 13.6 W and it decreases to 4.4 W gradually with

decreasing groove width at the evaporator of the converging heat pipes. On the other hand, the maximum capillary pumping provided by the heat pipe increases with decreasing groove width at the evaporator of the converging heat pipes.

However, when thermal resistances at the maximum heat are compared, it is seen that they are approximately the same for relatively wide heat pipes, and increase with narrower grooves (HP-400 and HP-300). Therefore, it is concluded that the effect of converging grooves on the thermal resistance of the heat pipes at its maximum heat load was not significantly effective.

To conclude, converging groove geometry in order to increase the heat pipe performance is not useful without increasing the evaporation performance and decreasing the frictional losses.

4.2   Hierarchical Groove Architecture

Simulations of the converging grooved heat pipes show that narrow grooves increase the capillary pumping power of the heat pipes. On the other hand, friction losses also increase in the converging grooved heat pipes. Therefore, while decreasing the groove width to increase the capillary pumping, the adverse effect of friction should be considered. Another conclusion of the converging groove simulations is the unfavorable effect of these type of grooves on the thermal resistance of the heat pipes for the narrowest grooves. It should be noted that the number of grooves in the converging grooved heat pipes are the same compared to straight grooved heat pipes. Therefore, evaporating regions that occur at the contact line are similar for all the heat pipes that are simulated in Section 4.1.

In this section of the present study, another innovative groove type, named as *Hierarchical Groove Architecture* (HGA) will be proposed. In the HGA, widths of the grooves and the fins are constant from the condenser to a point of the evaporator, afterwards branching into narrower grooves. Sudden narrowing of the grooves increases the contact angle between the working fluid and the walls of the heat pipe. Therefore, an extra capillary pumping capacity is provided to the heat pipe. Since the number of grooves increases at the branched region of the

hierarchical grooved heat pipes, number of the contact lines are increased, and evaporation resistances can be decreased by increasing the number of contact lines. Briefly, the proposed HGA has two important effects on the heat pipe, namely boosting capillary pumping and enhancing evaporation.

4.2.1 Boosting capillary pumping

The proposed HGA allows boosting of the capillary pumping to transport more heat compared to the same size standard straight grooved heat pipes. In order to boost the capillary pumping, the number of grooves in the HGA is increased at the specified point of the heat pipe to increase the contact angle, θ_{ca}, at the contact line.

The aim of using a HGA is shown in Figure 4.2. If the heat input is higher than the capillary pumping limit of the heat pipe, two phenomena might occur inside the heat pipe. The first is the pool region formation at the condenser region. In this case, the contact angle, θ_{ca}, is at its minimum value, equal to material contact angle, at the beginning of the evaporator, and approaches 90° before reaching to the end of the condenser. In this case, pool region formation occurs at the remaining part of the condenser, and the overall thermal resistance at the condenser increases because its effective length decreases. This phenomenon is illustrated in Figure 4.2-a.

The second phenomenon is the dryout. In this case, the contact angle, θ_{ca}, reaches its minimum value before reaching to the end of the evaporator although the contact angle, θ_{ca}, is close to 90° at the beginning of the condenser. Therefore, liquid cannot reach the remaining part of the evaporator and dryout occurs. Since the effective length of the evaporator decreases, the temperature difference between the evaporator and the condenser increases. This phenomenon is illustrated in Figure 4.2-b.

The groove architecture in Figure 4.2-c is the proposed HGA, which causes an increase in the contact angle from the wide side, θ_w, to the narrow side, θ_n, by decreasing the groove width. Increasing the contact angle at the narrow

side provides an extra capillary pumping capacity to the heat pipe, so that the heat pipe can carry more heat compared to straight grooves without pool region formation or dryout. Since the radius of curvatures at both narrow and wide sides are equal due to equality of pressures, the relation between these two contact angles is calculated as follows:

$$\Theta_n = \cos^{-1}\left(\frac{\cos\Theta_w}{d}\right) \tag{4.1}$$

where d is the number of branches per groove.
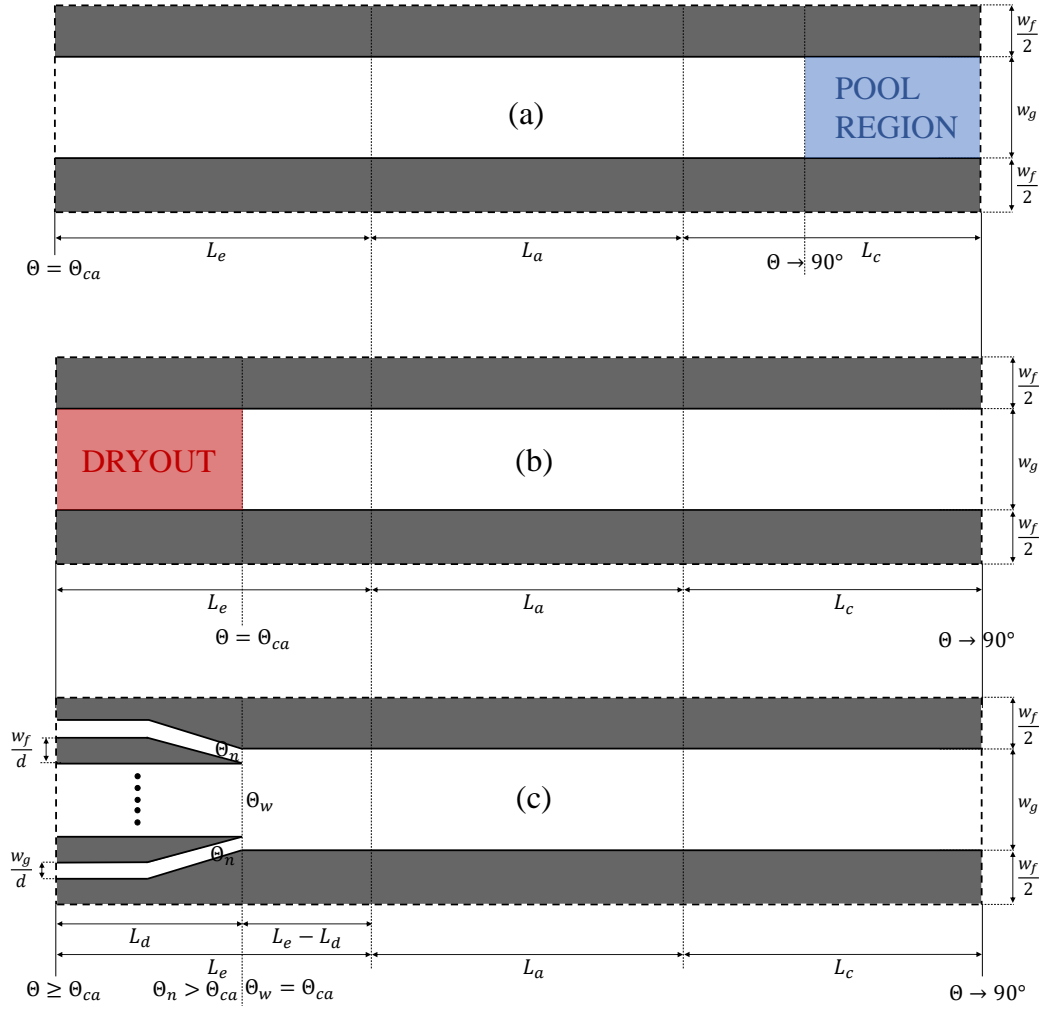
Figure 4.2: Hierarchical groove architecture (HGA) for boosting capillary pumping

4.2.2 Enhanced evaporation

As it was mentioned in the Section 2.4.2.1, most of the liquid evaporates from the top of the fin where the contact line occurs, which means that the resistance in this region is at a minimum. The calculations that are performed in the current study also support this interpretation. Therefore, increasing the number of grooves in the heat pipe increases the number of contact lines and results in decreasing the overall thermal resistance at the evaporator region of the heat pipe. In other words, the same amount of heat can be transported with lower temperature differences throughout the heat pipe including more grooves, which was shown in the experimental study of [59].

However, because of increasing friction forces that was mentioned at the beginning of this section with increasing number of grooves for the same size heat pipes, transporting the same amount of heat with lower temperature differences is limited by the capillary pumping limit of the heat pipe including more grooves.

The proposed HGA increases the number of grooves especially at the evaporator; therefore, evaporation regions are also increased. The red lines in the Figure 4.3 show the contact line regions at the evaporator regions of both the regular straight (upper figure) and the proposed HGA (lower figure) heat pipes. It is obvious that evaporation regions increase with increasing number of branches at the hierarchical part of the heat pipe. Therefore, it is aimed to reduce the overall thermal resistance of the heat pipe by using the HGA. To sum up, the proposed HGA increases not only the capillary pumping but also enhances the evaporation by decreasing the thermal resistance in the branched region of the heat pipe.
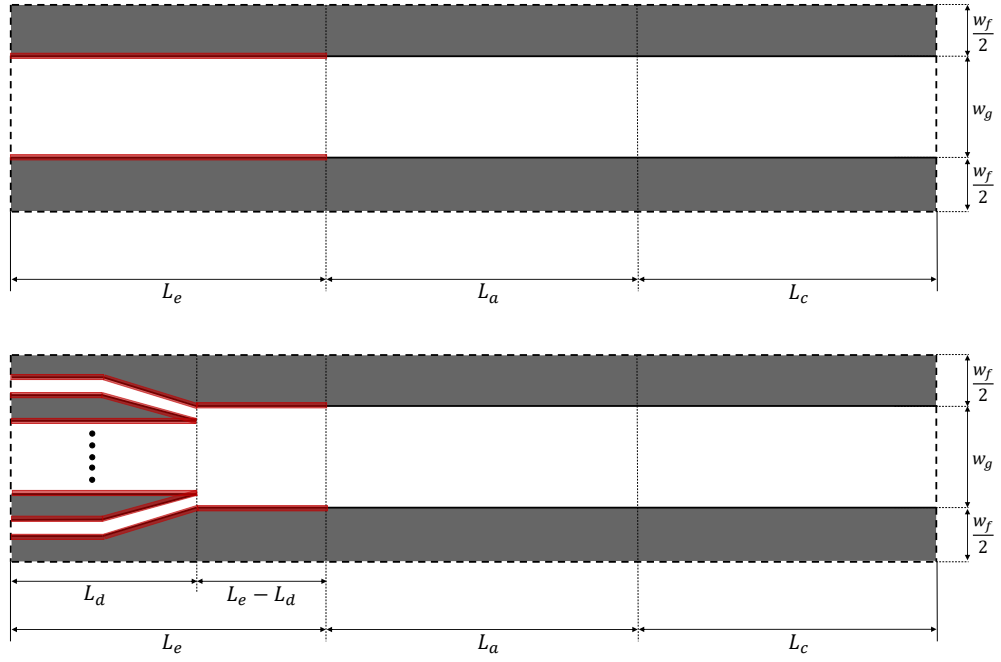
Figure 4.3: Hierarchical groove architecture (HGA) for enhancing evaporation

4.2.3 Produced groove frames for the experiments of hierarchical groove architecture

In order for the experimental validation of the proposed HGA, three different groove frames are designed, manufactured and mounted to the modular experimental setup. Conventional machining processes are used to manufacture these groove frames. While designing these groove frames, the numerical model that is developed in the present study was exercised.

Due to the limitations of the milling cutter substructure, which is used for machining the groove frames, the minimum width of the groove could only be 0.3 mm. Another limitation of it is the aspect ratio of the grooves which is 1.5 for the 0.3 mm cutter. Therefore, in order for getting a precise production, the height of the groove is specified as 0.4 mm. Thus, the minimum groove is a rectangle 0.3 mm in width and 0.4 mm in height. According to the dimensions of the experimental setup, 38 grooves are machined to the first groove frame in these dimensions.

In order to compare the effect of the groove size on the capillary limit, the width

of the groove is doubled in the second groove frame. Therefore, the second groove frame has 19 rectangular grooves 0.6 mm in width and 0.4 mm in height.

Grooves in the third groove frame starts with the 0.6 mm width at the condenser, and branch into two grooves at the specified location of the heat pipe. In other words, the third groove frame has the proposed HGA.

After determining the dimensions of the grooves in these groove frames, the lengths of the evaporator, the condenser, the branched and the adiabatic regions are determined by conducting simulations using the numerical model developed in this thesis as listed in Table 4.3. Three manufactured grooved frames are shown in Figure 4.4, and detailed views of the branching of the *Hierarchical Groove Architecture* under microscope is shown in Figure 4.5.

Table 4.3: Details of the manufactured groove frames

	Frame #1	Frame #2	Frame #3
L_e(mm)	26	26	26
L_a(mm)	48	48	48
L_c(mm)	26	26	26
L_d(mm)	-	-	25
w_g(mm)	0.3	0.6	$0.6 \to 0.3$
w_f(mm)	0.3	0.6	$0.6 \to 0.3$
h_g(mm)	0.4	0.4	0.4
h_b(mm)	1.6	1.6	1.6
Number of grooves	38	19	$19 \to 38$
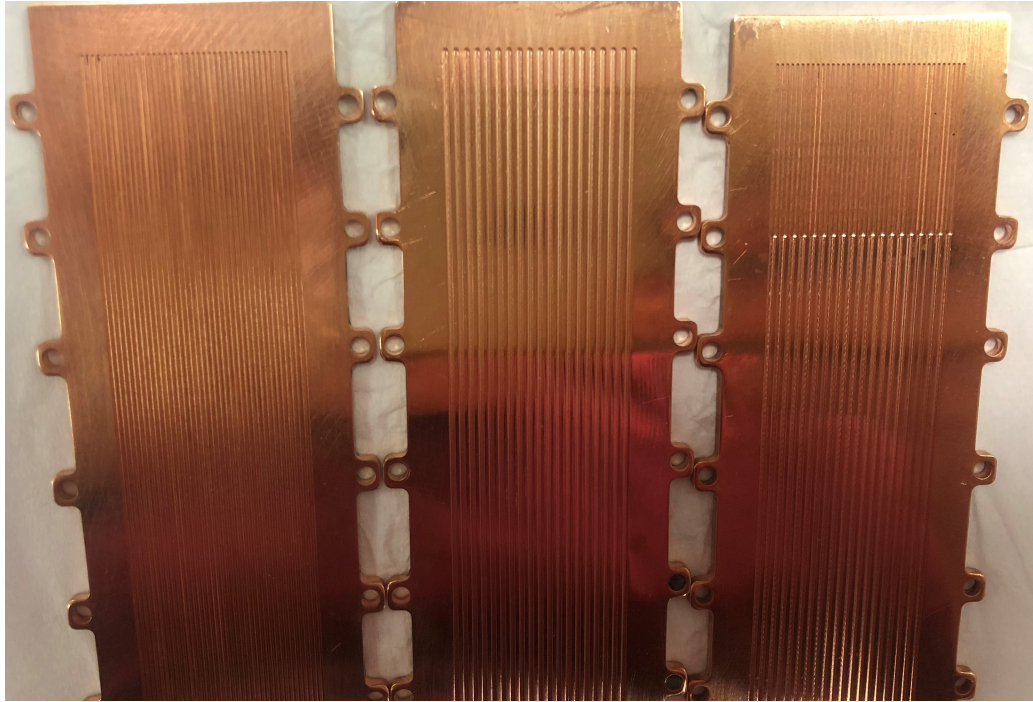
Figure 4.4: Manufactured grooved frames for the experimental study for HGA
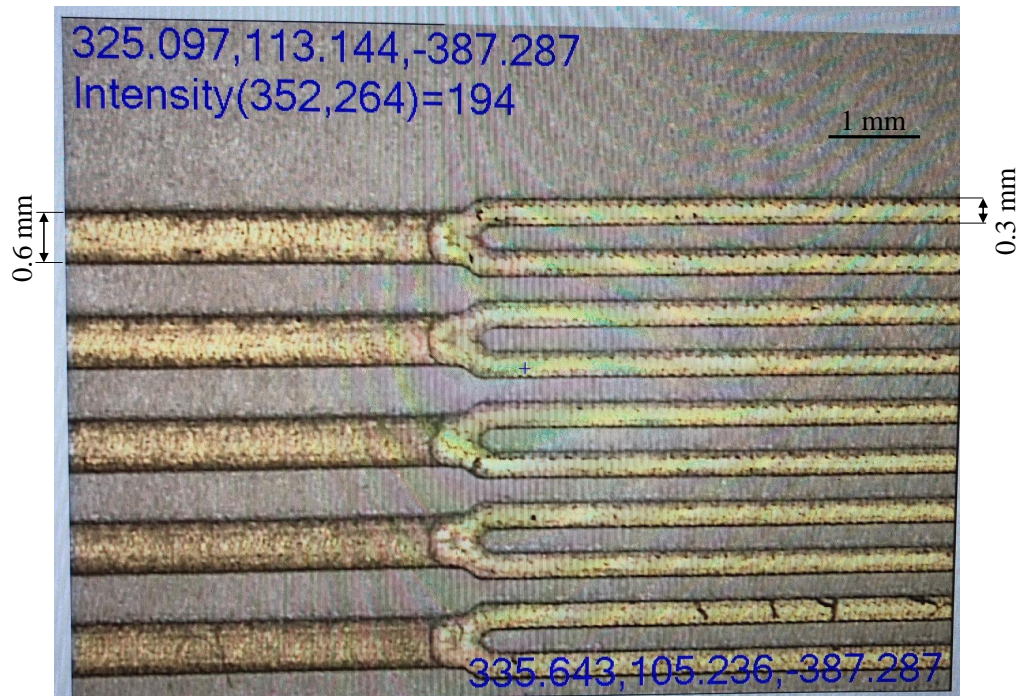
Figure 4.5: Detailed view of the branching of the HGA under microscope

4.2.4 Simulation results for capillary pumping enhancement

It was mentioned that the proposed HGA increases the capillary pumping. In other words, by using HGA, the heat pipe can transport more heat compared to the same size heat pipes. In this section of the current study, the results of the simulations will be presented. The produced groove frames to observe the boosting capillary pumping are introduced in Section 4.2.3, and the details of the geometric parameters of these groove frames are listed in Table 4.3. The heat pipes that are simulated in this section are named as HP–300×400 (heat pipe with 300 μm groove width and 400 μm groove height), HP–600×400 (heat pipe with 600 μm groove width and 400 μm groove height) and HP–600/2×400 (hierarchical heat pipe with 600 μm groove width and branched into two and 400 μm groove height) with respect to groove frames #1, #2, and #3 explained in Section 4.2.3.

First simulations are run to determine the maximum heat transfer capacity of the heat pipes. The maximum capillary pumping for the grooved heat pipes occur when the contact angle at the triple line varies between the material contact angle and 90° from the evaporator to the condenser. Therefore, the maximum heat transfer capacities of the HP–300×400 and the HP–600×400 are calculated by running the numerical model between these two limits.

On the other hand, the contact angle variation is not continuous along the hierarchical heat pipe because of the branching of the grooves and the relation between the two sides of the branching point is calculated by Eqn. 4.1. Therefore, in order for obtaining the maximum capillary pumping for the hierarchical grooved heat pipes, the contact angle at the triple line is assumed to vary between the material contact angle and 90° at the wide side of the grooves as illustrated in Figure 4.2. Finally, the maximum heat transfer capacity of the HP-600/2×400 was calculated by running the numerical model by integrating these assumptions.

The results of the simulations of the numerical model for the heat pipes (HP–300×400, HP–600×400, and HP–600/2×400) are given in Table 4.4. As pre-

92

dicted before, the hierarchical heat pipe HP–600/2×400 carries 20% more heat compared to standard grooved heat pipe with 600 μm grooves, HP–600×400. Moreover, even if the narrower grooves have more capillary pumping theoretically, because of the increasing friction forces in the narrower grooves, the HP–300×400 carries less heat compared to both the HP–600×400 and the HP–600/2×400.

Table 4.4: The results of the simulations of HP–300×400, HP–600×400, and HP–600/2×400 for maximum heat transport

	Q_{max} (W)	ΔT (°C)	R (K/W)
HP–300×400	9.5	5.2	0.55
HP–600×400	13.6	12.5	0.92
HP–600/2×400	16.9	14.4	0.85

Although it is calculated that the HP–600/2×400 carries more heat than the HP–600×400, when the temperature differences between the evaporator and the condenser of the heat pipes are examined, it is seen that the temperature differences increase with the heat carrying capacity. In order to show that the HP–600/2×400 can carry more heat with a lower temperature difference compared to the HP–600×400 (i.e., the HP–600/2×400 is more efficient), the maximum heat transport calculated for the HP–600/2×400 (16.9 W) is applied to the HP–600×400.

Two phenomena occur when the heat pipe is forced to carry more heat than the maximum amount of heat that it can carry. One of these is the dryout and the other is the pool region formation. Which of these two situations will occur depends on the amount of liquid in the heat pipe. If the filling ratio is low, then the contact angle at the end of the condenser approaches 90°, and the contact angle, θ_{ca}, reaches its minimum value before reaching to the end of the heat pipe. Therefore, part of the evaporator becomes ineffective, in other words, dryout occurs. If, on the contrary, the filling ratio is high, then the contact angle, θ_{ca}, starts with its minimum value at the evaporator and approaches 90° before reaching at the end of condenser. In this case, the remaining condenser

region after the contact angle, θ_{ca}, reaches 90° becomes useless, in other words, pool region formation occurs.

Table 4.5 shows the comparison between the HP–600×400 and the HP–600/2×400 when the pool region formation occurs in the HP–600×400. To get these results, the numerical model is modified to estimate the pool region formation, and the effective length of the condenser, $L_{c,eff}$, was calculated as 12 mm over 26 mm. Therefore, the thermal resistance in the condenser region increased due to the shortening of the effective condenser length as in the case of pool region formation. As a result of this, the temperature difference in the HP–600×400 at the same heat input is higher approximately 17% compared to HP–600/2×400.

Finally, the simulation results in Tables 4.4 and 4.5 show that the proposed HGA increases the capillary pumping power in grooved heat pipes. Therefore, a heat pipe with a HGA can carry more heat without any dryout or pool region formation compared to the heat pipe that has the same volume and standard grooves.

Table 4.5: Summary results of the simulations of HP-600×400 and HP-600/2×400 for 16.9 W heat input for the pool region formation

	Q_{in} (W)	ΔT (°C)	R (K/W)	$L_{c,eff}$ (mm)
HP-600×400	16.9	17.5	1.04	12
HP-600/2×400	16.9	14.4	0.85	26

4.2.5   Experiment results for capillary pumping enhancement

The simulated heat pipes, HP-300×400 (heat pipe with 300 μm groove width and 400 μm groove height), HP-600×400 (heat pipe with 600 μm groove width and 400 μm groove height) and HP-600/2×400 (hierarchical heat pipe with 600 μm groove width and branched into two and 400 μm groove height) are also tested in the modular experimental setup that is designed and constructed in the present study. Figure 4.6 shows the details of the evaporator, the adiabatic, the condenser regions and the thermocouple locations of the tested heat pipes.

In these heat pipes, number of thermocouples is increased to 15 to get better temperature distribution resolution along the heat pipe wall. T-type thermocouples are assembled using the same two-component metal epoxy that was used in the previous experiment. Exactly the same experimental procedures explained in Section 3.3.6 are applied. First, the heat pipe is filled with IPA and the specified heat flux is applied to the heat pipe until the system reached steady state. Then, some IPA is aspirated from the heat pipe and exactly the same heat flux is tested again. This procedure is continued until no IPA remained in the heat pipe. Finally, the minimum temperature difference that is occurred during the experiments is taken as the optimum operating point of the heat pipe at the specified heat flux.
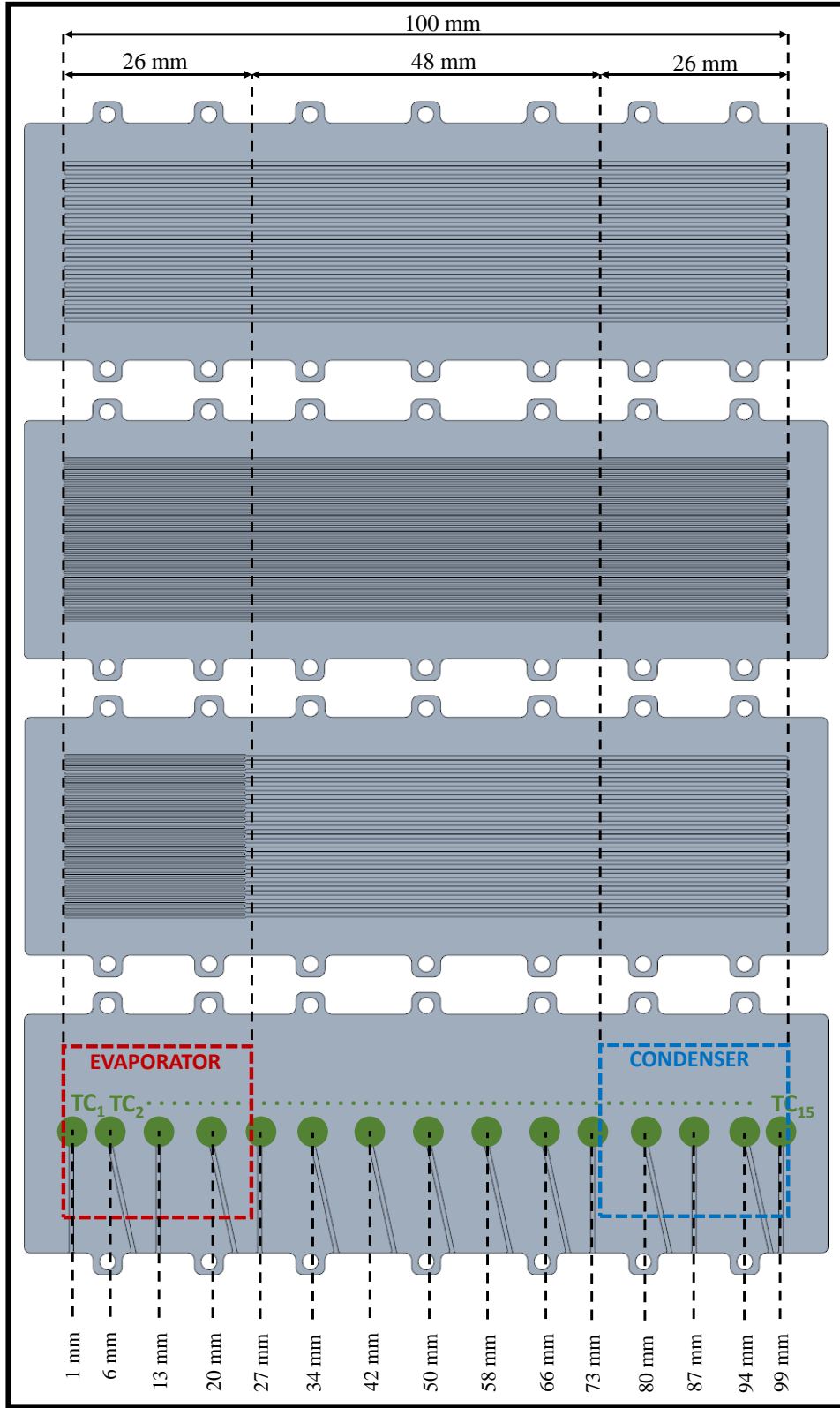
Figure 4.6: Details of the evaporator, adiabatic, condenser regions and the thermocouple locations of the HP-300×400, HP-600×400, and HP-600/2×400

96

Experiments are started with the HP–600×400 for three different heat inputs, namely 9.5 W (1.5 W/cm^2), 13.6 W (2.1 W/cm^2) and 16.9 W (2.6 W/cm^2). According to the simulations, 1.5 W/cm^2 is the moderate heat flux for HP-600×400; therefore, the heat pipe can transport this amount of heat easily from the evaporator to the condenser region. On the other hand, 2.1 W/cm^2 is the highest heat load that HP-600 can carry from the evaporator to the condenser region for this configuration. Finally, pool region formation is expected to occur at 2.6 W/cm^2 for HP-600×400.

Figure 4.7 shows the results of the experiments to find the optimum operating point of the HP-600×400 for 9.5 W heat load. The vertical axis shows the maximum temperature difference that occurred throughout the heat pipe during the experiments and the horizontal axis shows the order of the experiment. The filling ratio in experiment #1 is higher than the optimum value. In other words, the heat pipe was fully-flooded. In this case, the system did not operate as a heat pipe and the temperature difference is high.
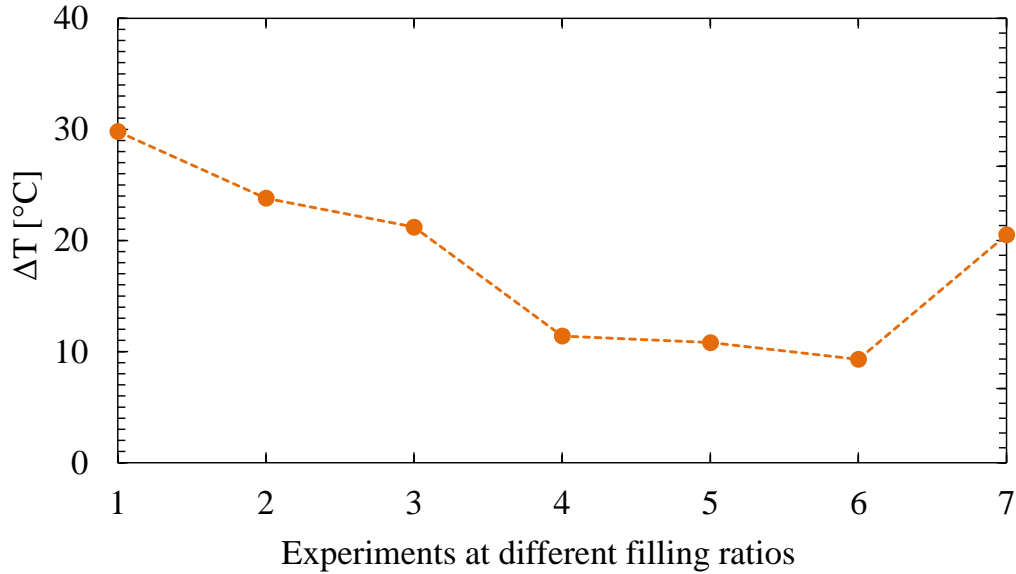
Figure 4.7: Temperature differences of the HP–600×400 in the present study for different filling ratios, $q =$ 9.5 W ($q'' =$ 1.5 W/cm^2).

Then, some amount of IPA is aspirated from the heat pipe and the experiment is repeated. The result of this experiment corresponds to the experiment #2 in Figure 4.7. In this case, the temperature difference between the two ends of the

heat pipe decreases compared to experiment #1. This procedure is continued until the decrease in temperature difference stops and then starts to increase (see Figure 4.7 for experiments #6 and #7). After seven experiments, it is observed that the temperature differences are almost equal in the experiments #4, #5, and #6. Since the heat load (9.5 W) is lower than the maximum heat load that HP–600×400 can carry, the minimum temperature differences at different filling ratios are expected. Finally, the result of experiment #6 is the optimum operating point of the HP–600×400 under 9.5 W heat load and it is used for comparison with the simulation results.

Figure 4.8 shows the results of the experiments of the HP–600×400 under 13.6 W heat load at different filling ratios. Exactly the same procedure is repeated to find the optimum operating point of the heat pipe (experiment #1 is fully-flooded operation and dryout occurs in experiment #10). However, in this case, it is expected that the optimum operating point of the heat pipe should be unique and not a range since the 13.6 W is the maximum heat that HP–600×400 can carry for this configuration. Results of the experiments prove this prediction, and it is found that the minimum temperature difference occurred at experiment #6 only.
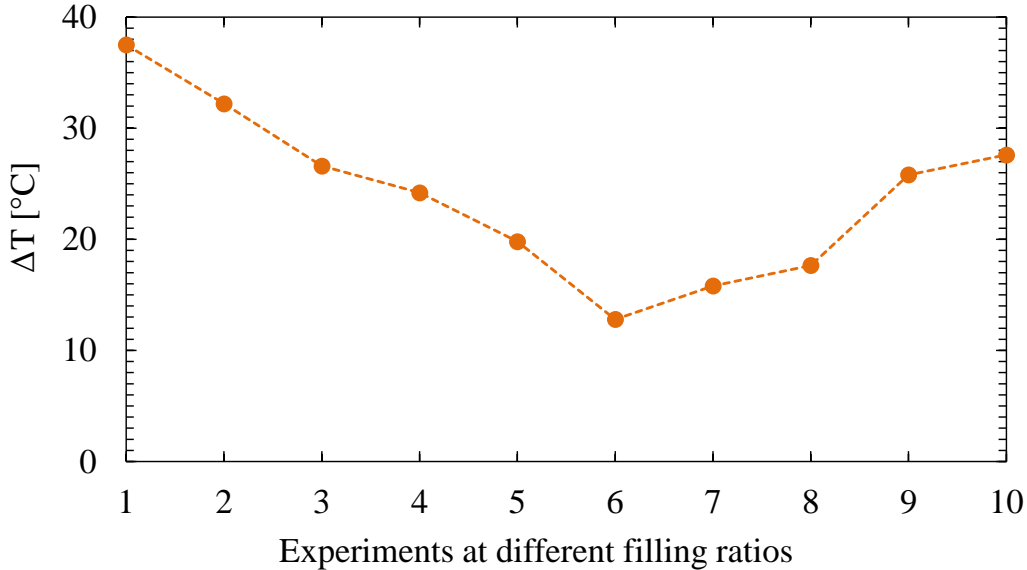
Figure 4.8: Temperature differences of the HP–600×400 in the present study for different filling ratios $q = 13.6$ W ($q'' = 2.1$ W/cm^2).

Figures 4.9–4.11 show both the wall temperature and the radius of curvature variations of the HP-600×400 for three different heat loads (9.5 W, 13.6 W and 16.9 W). Blue dots and yellow lines are wall temperature results of experiments and simulations, respectively. Gray dashed lines are vapor temperatures. Purple lines are numerical results of radius of curvature. Numerical model with multi-slice thermal resistance network that is developed during the present study is run to find the temperature and radius of curvature variations. The thermal resistance network has 100-slice and the flow model has 1000 slices (100-T/1000-F) in the simulations.

Figure 4.9: Wall temperature, radius of curvature, and vapor temperature of the HP–600×400, $q = 9.5$ W ($q'' = 1.5$ W/cm^2).

Figure 4.10: Wall temperature, radius of curvature, and vapor temperature of the HP–600×400, $q = 13.6$ W ($q'' = 2.1$ W/cm^2).
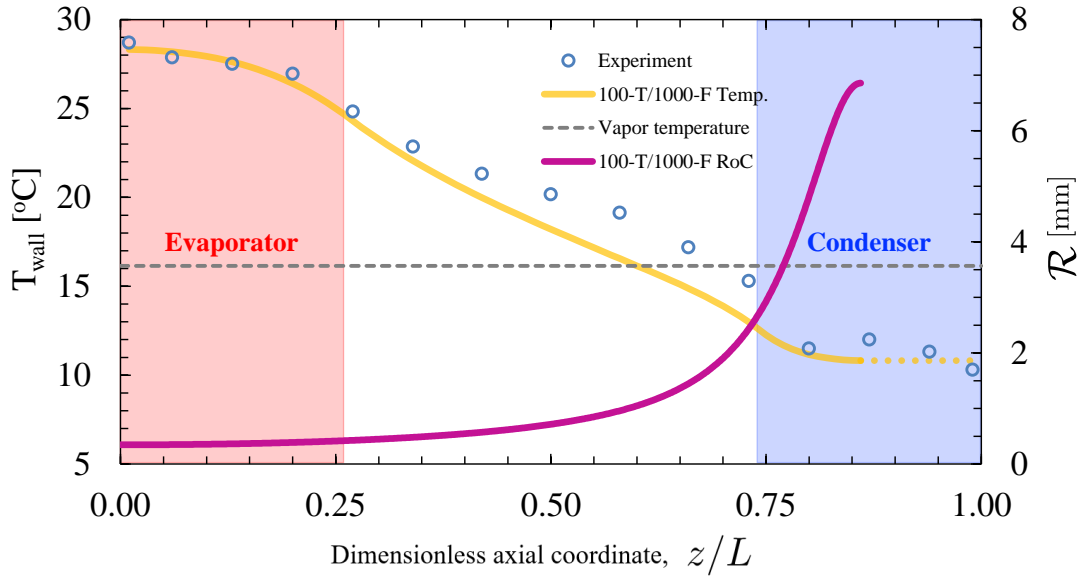
Figure 4.11: Wall temperature, radius of curvature, and vapor temperature of the HP–600×400, $q = 16.9$ W ($q'' = 2.6$ W/cm^2).

It is found that the increase of the radius of curvature is small in 1.5 W/cm^2 compared to 2.1 W/cm^2 and 2.6 W/cm^2 since the required capillary pumping is low for 1.5 W/cm^2. In addition, radius of curvature reaches its maximum value before reaching the end of the heat pipe for 2.6 W/cm^2 since this heat load is higher than its maximum heat transfer capacity. Therefore, only 12 mm of the condenser over 26 mm is effectively operated and the remaining 14 mm of condenser is pool region (see Figure 4.11). As a result of this, the overall resistance and the temperature difference between the two ends of the heat pipe increases.

Figures 4.9–4.11 show that the results of the experiments and the simulations match. The largest deviations between the results of the numerical model and the experiments are in the section of the adiabatic region neighboring the condenser region, which is common in all results. The reason of these deviations is attributed to the use of the 4th order polynomial approach for condensation since this approach may not define film thickness variation at the top of the fins adequately especially at the transition region between evaporation and condensation.

After the experiments of the HP–600×400 are completed, a new set of experiments are conducted with the HP–600/2×400 for the same three heat inputs. Figures 4.12–4.14 show both the wall temperature and the radius of curvature variations of the HP–600/2×400 for three different heat loads (9.5 W, 13.6 W and 16.9 W). Blue dots and yellow lines are wall temperature results of experiments and simulations, respectively. Gray dashed lines are vapor temperatures. Purple lines are numerical results of radius of curvature. Numerical model with multi-slice thermal resistance network that is developed during the present study is run to find the temperature and radius of curvature variations. The thermal resistance network has 100 and the flow model has 1000 slices (100-T/1000-F) in the simulations.
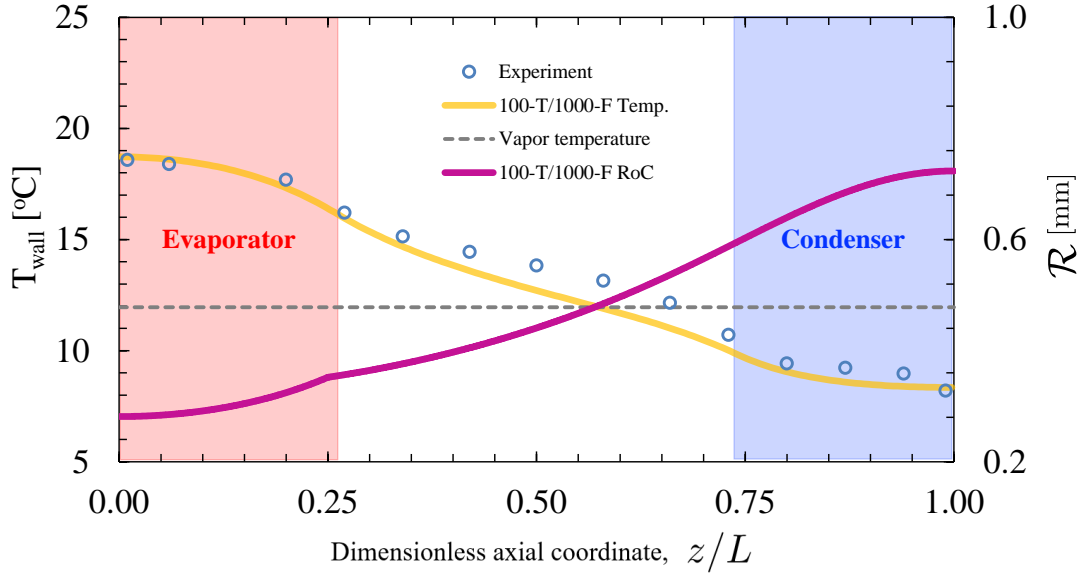
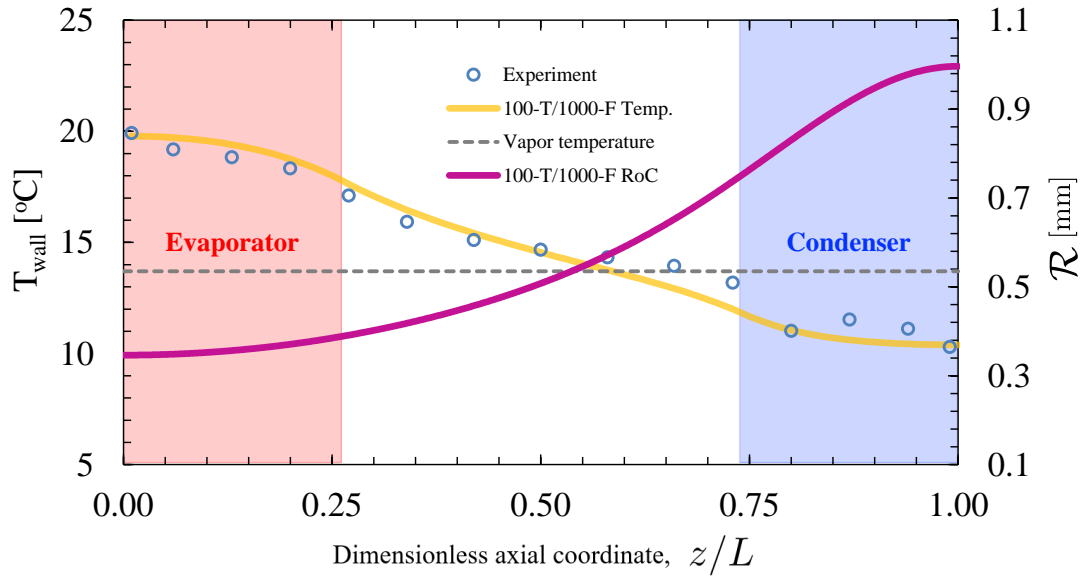Figure 4.12: Wall temperature, radius of curvature, and vapor temperature of the HP–600/2×400, $q = 9.5$ W ($q'' = 1.5$ W/cm^2).
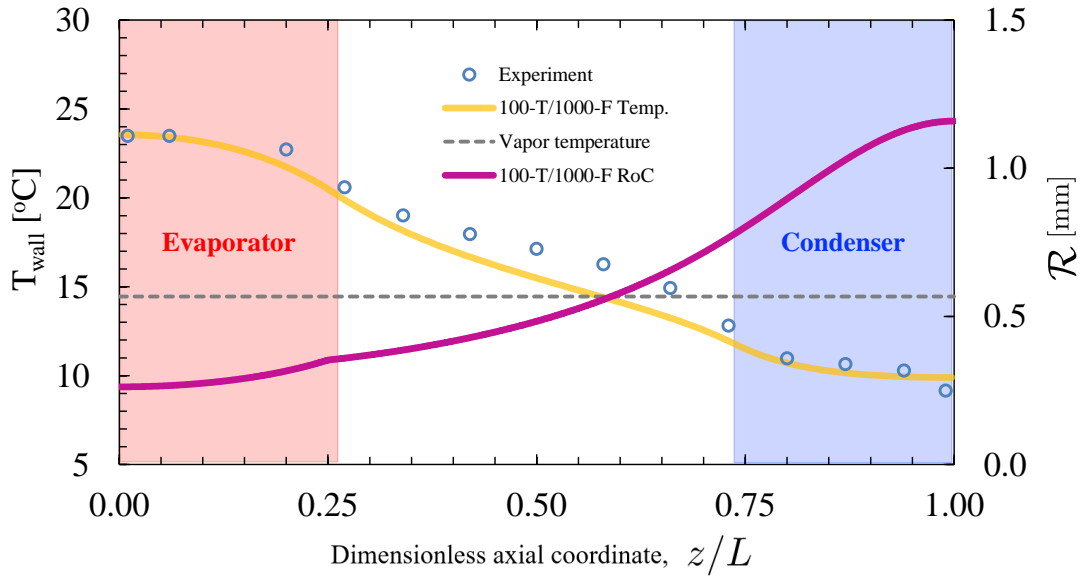
Figure 4.13: Wall temperature, radius of curvature, and vapor temperature of the HP–600/2×400, $q = 13.6$ W ($q'' = 2.1$ W/cm^2).
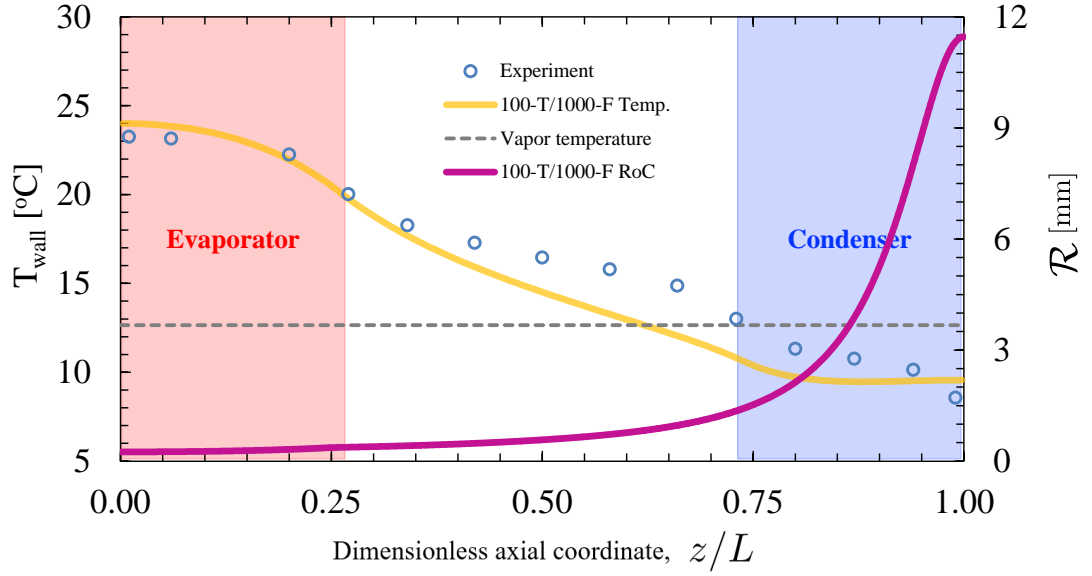
Figure 4.14: Wall temperature, radius of curvature, and vapor temperature of the HP–600/2×400, $q = $ 16.9 W ($q'' = $ 2.6 W/cm^2).

Figure 4.14 shows both the wall temperature and the radius of curvature variations of the HP–600/2×400 for 16.9 W heat load. Results show that the heat pipe with the HGA increases the capillary pumping and decreases temperature difference between the two ends of the heat pipe compared to HP–600×400. According to experiments of HP-600×400 and HP-600/2×400 for 16.9 W heat load, the temperature difference in the HP-600/2×400 is 20% lower compared to HP-600×400. Therefore, comparison of results of these cases prove the boosting capillary pumping of the HGA.

After the experiments of the HP–600/2×400 are completed, a new set of experiments are conducted with the HP–300×400 for the same three heat inputs. Figures 4.15 and 4.16 show both the wall temperature and the radius of curvature variations of the HP–300×400 for two different heat loads (9.5 W and 13.6 W. Blue dots and yellow lines are wall temperature results of experiments and simulations, respectively. Gray dashed lines are vapor temperatures. Purple lines are numerical results of radius of curvature.
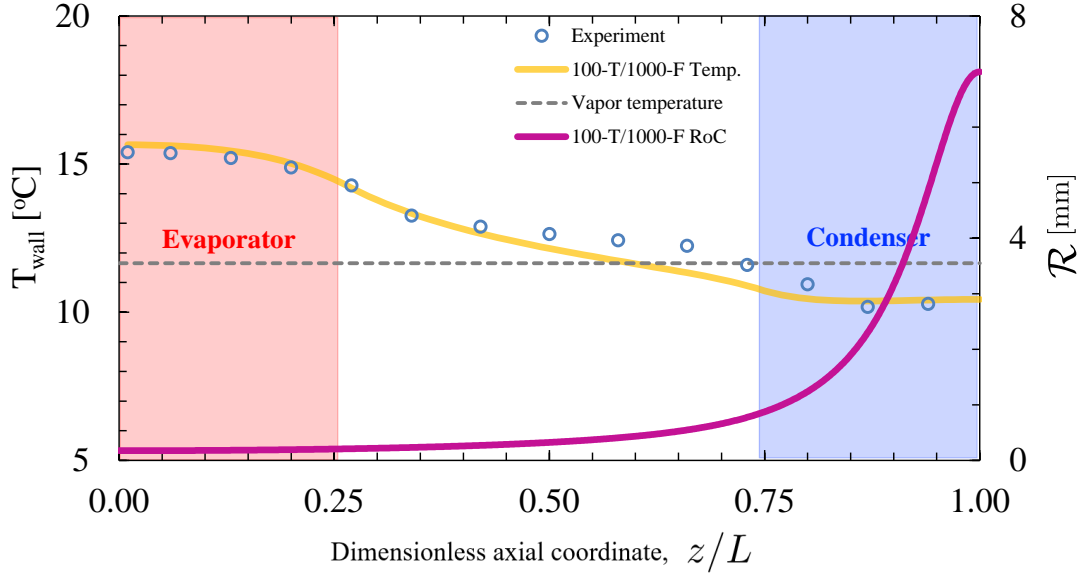
Figure 4.15: Wall temperature, radius of curvature, and vapor temperature of the HP–300×400, $q = 9.5$ W ($q'' = 1.5$ W/cm^2).
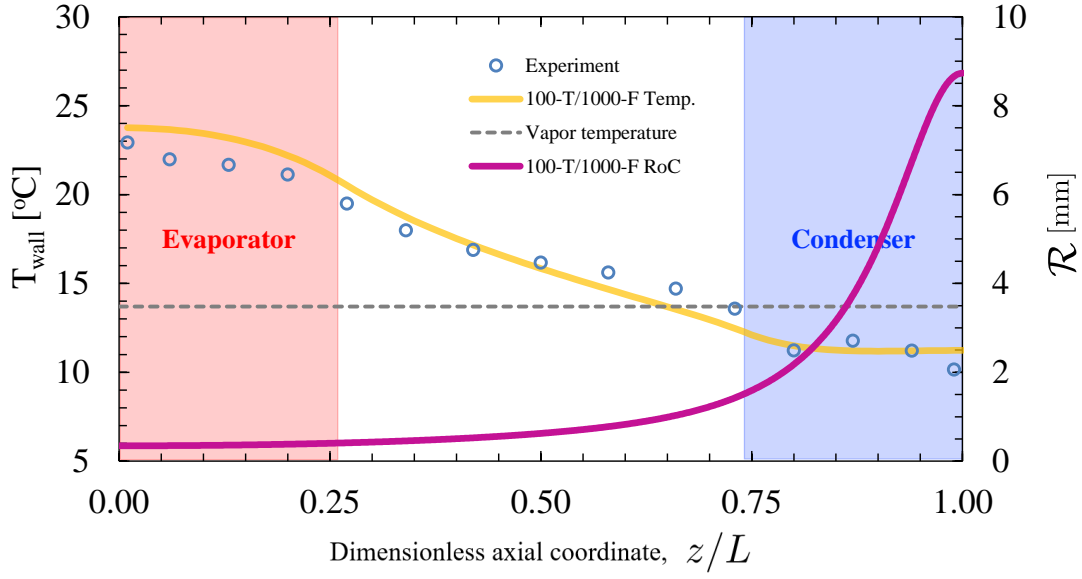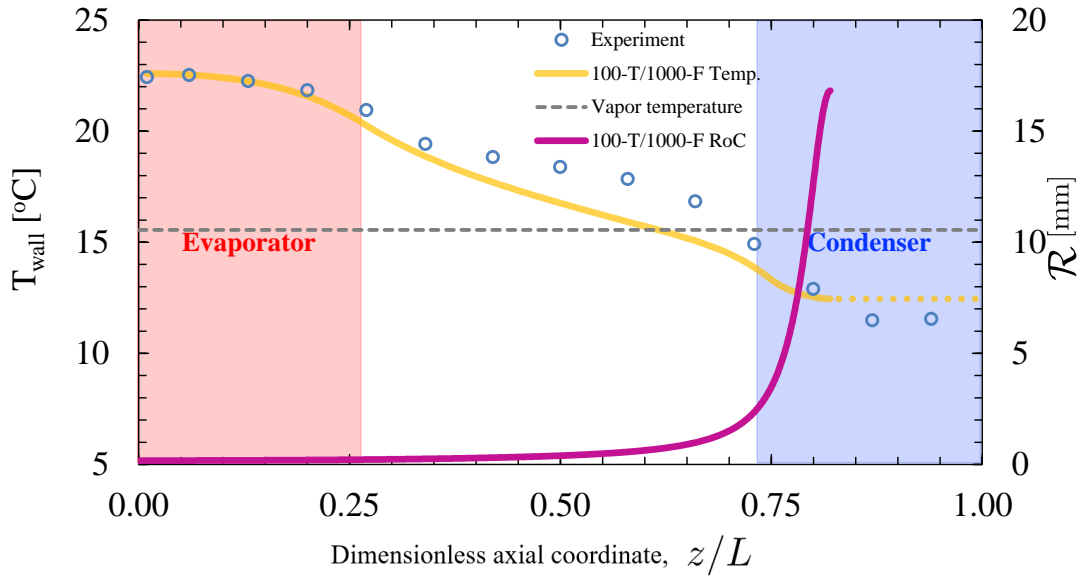

Figure 4.16: Wall temperature, radius of curvature, and vapor temperature of the HP–300×400, $q = 13.6$ W ($q'' = 2.1$ W/cm^2).

It is found that temperature difference to carry 9.5 W heat load by using HP–300×400 is lower compared to the HP–600×400 and HP–600/2×400 as predicted in the simulations. For the case of 13.6 W heat load, pool region formation occur in the HP–300×400 and the effective length of the condenser become 8 mm. On the other hand, simulations for 16.9 W heat load is not applicable since pool region formation covers the entire condenser region according to numerical model.

Finally, the temperature differences between the two ends of the heat pipes that are simulated by the code developed in this thesis and experimentally measured are shown in Table 4.6. Results show that the numerical model that is developed in the present study simulated the heat pipes sufficiently close in the order of seconds.

Table 4.6: The results of the simulations and the experiments of HP-300×400, HP-600×400 and HP-600/2×400 for different heat loads

	9.5 W		13.6 W		16.9 W	
	ΔT (°C)		ΔT (°C)		ΔT (°C)	
	Exp.	Sim.	Exp.	Sim.	Exp.	Sim.
HP-300×400	5.1	5.2	10.9	10.1	21.0	NA
HP-600×400	9.6	9.4	12.8	12.5	18.4	17.5
HP-600/2×400	10.4	10.4	14.3	13.7	14.7	14.4

4.2.6 Simulation results for enhancing evaporation

The decreasing effect of increasing number of grooves on the thermal resistance of the heat pipe is introduced in Section 4.2.2. In order to show that the the numerical model is able to simulate this effect, a different set of simulations was performed by the the numerical model using HP–300×400, HP–600×400 and HP–600/2×400. For this simulation, the minimum heat input among the results of the maximum heat transport of these three heat pipes, which is 9.5 W, is applied for both HP–600×400 and HP–600/2×400 and the results of these simulations are given in Table 4.7. Results show that the HP-300×400 can

transfer the same amount of heat with smaller temperature differences compared to HP–600×400 and HP–600/2×400.

Table 4.7: The results of the simulations of HP–300×400, HP–600×400 and HP–600/2×400 for 9.5W heat input

	Heat Input (W)	ΔT (°C)	R (K/W)
HP–300×400	9.5	5.2	0.55
HP–600×400	9.5	9.4	0.99
HP–600/2×400	9.5	10.4	1.09

However, contrary to expectations, although there are more grooves in the evaporator part of the HP–600/2×400, the same amount of heat is carried with higher temperature differences compared to the HP–600×400. The reason of this increase in the temperature difference is the increase of the contact angle at the triple line of the grooves in the branched part of the evaporator (see Eqn. 4.1). Although the number of grooves at the branched region is doubled, the increase in the thermal resistance due to an increase in contact angle at the triple line dominates the effect of increasing number of grooves.

Therefore, it is proposed that if the number of branches at the evaporator of the HGA is increased, then the effect of increasing thermal resistance due to increasing contact angle at the triple line becomes less significant and as a result the temperature difference decreases. In order to show that a new set of heat pipes are offered guided by the simulations using the numerical model. The aim of this set of simulations is to show that the HGA reduces the maximum temperature at the evaporator especially for high heat fluxes. Therefore, the length of the evaporator is kept short to increase the heat flux and evaporator region is fully branched to increase the effect of increasing number of grooves. The lengths of the evaporator, the adiabatic and the condenser regions of the heat pipe are 12 mm, 62 mm and 26 mm, respectively. The solid material of the heat pipe is chosen as copper, and the working fluid is IPA.

Five heat pipes are simulated in this case and the only difference between them is the number of branches of a groove at the evaporator. The first heat pipe

(HP–400) has standard straight grooves without any branching (the number of branches of a groove was taken as 1). Grooves in the HP–400/2, HP–400/4, HP–400/8, and HP–400/16 are branched into 2, 4, 8 and 16 grooves at the evaporator region of the heat pipe, respectively. The details of the dimensions of these heat pipes are given in Table 4.8.

The first simulation is conducted to calculate the maximum heat transfer capacity of HP–400 and it is found as 11.3 W by the numerical model. If the heat input is beyond the maximum heat transfer that can be carried by HP–400, it will operate with dryout condition or pool region formation. Therefore, the calculated heat input, 11.3 W, is applied to all heat pipes given in Table 4.8, although the maximum heat transfer capacity of the hierarchical heat pipes are higher than 11.3 W. In addition to simulations for 11.3 W heat load, the maximum heat transport capacities of these five heat pipes are also calculated by using the numerical method that is developed in the present study.

Table 4.8: Dimensions of the simulated heat pipes for the enhancing evaporation

	HP-400	HP-400/2	HP-400/4	HP-400/8	HP-400/16
L_e(mm)	12	12	12	12	12
L_a(mm)	62	62	62	62	62
L_c(mm)	26	26	26	26	26
L_d(mm)	-	12	12	12	12
L_{total}(mm)	100	100	100	100	100
W_{hp}(mm)	25	25	25	25	25
$w_g(\mu m)$	400	400 → 200	400 → 100	400 → 50	400 → 25
$w_f(\mu m)$	400	400 → 200	400 → 100	400 → 50	400 → 25
h_g(mm)	0.4	0.4	0.4	0.4	0.4
h_b(mm)	1.6	1.6	1.6	1.6	1.6
Branches	1	2	4	8	16
Grooves	30	30 → 60	30 → 120	30 → 240	30 → 480

Figure 4.17 shows the results of these simulations. The orange dots show the ratios of temperature difference between the two ends of the heat pipes (HP-400, HP-400/2, HP-400/4, HP-400/8 and HP-400/16) to the temperature difference of the heat pipe without any branches (HP-400). Blue dots show the maximum heat transport capacities of these heat pipes.

It is found that, first, the temperature difference ratio increases slightly with increasing number of branches per groove, then it decreases rapidly with increasing number of branch. The reason of the increase in the temperature difference ratios at low number of branches is the increase of the contact angle at the triple line of the grooves. Then, the increase of the number of branches of the groove at the evaporator—effectively the number of contact lines—dominates the effect of increasing thermal resistance due to increase of the contact angle at the triple line. As a result of this, the temperature difference and consequently the thermal resistance decreases as expected. For this case, for example, HP–400/16 can transport the same amount of heat with half the temperature difference compared to HP–400. Therefore, the HGA can be a powerful design option for cooling of hot-spots.
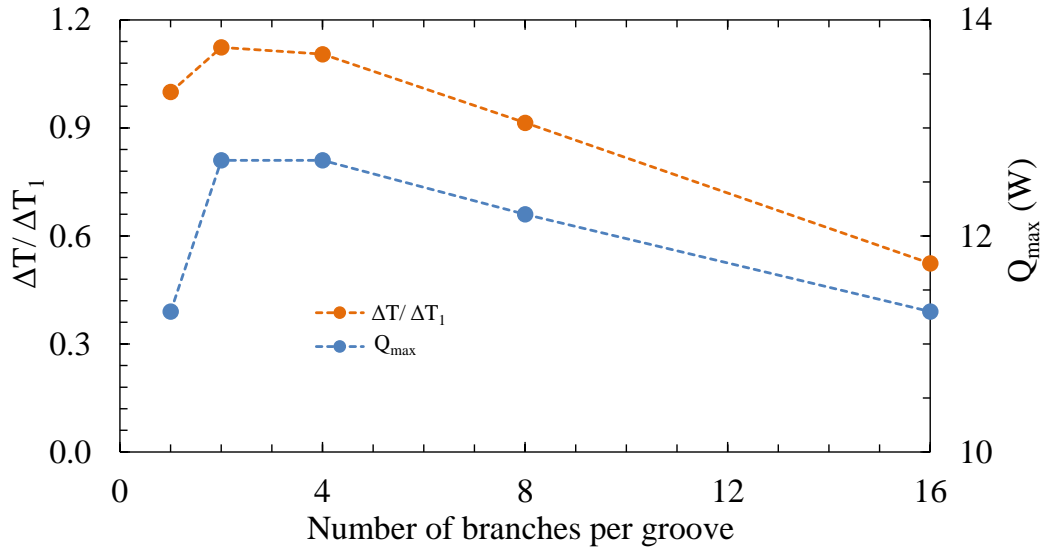
Figure 4.17: Variation of the maximum temperature difference and maximum heat transfer rate with the number of branches per groove.

Another result of these simulations is the variation of the maximum heat trans-

port capacity with the number of branches per groove. It is found that, first, the maximum heat transport capacity increases with increasing number of branches per groove, and then, it decreases with increasing branch number. The reason of this increase of the maximum heat transport capacity is the increased capillary pumping with branching. However, after a certain number of branch friction losses dominate the boosting capillary pumping, thus the maximum heat transport capacity decreases. For this case, after 16 branches, friction losses increase so much that the heat pipe cannot even carry this heat load without any dryout and pool region.

Finally, the HGA boosts the capillary pumping and enhances the evaporation as proposed. In addition, the numerical model that is developed in the current study allows to design heat pipes with the HGA.

CHAPTER 5

CONCLUSION AND RECOMMENDATIONS FOR FUTURE WORK

In this thesis work, first, a fast and accurate numerical model is developed as a design and diagnostic tool for the heat pipes. The numerical model is validated through available experiments in the literature conducted on the grooved heat pipes with constant and the variable cross sections. Although the predictions of the model are in a good agreement with the experimental results in terms of the axial distribution of both temperature and radius of curvature, temperature values predicted by the numerical tool are slightly higher. It is hypothesized that this difference arises due to the modeling of the condensation on the fin top, which is based on an approximate 4th order polynomial interface shape. Since this polynomial fitting approach was shown as a source of overestimation of film thicknesses in the literature, it is believed that the thicker film leading to larger thermal resistance, leads to the prediction of slightly overestimated temperatures.

Following the development of the numerical model, a modular experimental setup is designed and manufactured not only to assess the functionality of the numerical tool, but also test the performance of heat pipes with novel groove architectures. Similar to the comparisons with the experiments in the literature, numerical tool is successful in the performance prediction of heat pipes with straight grooves tested on the setup constructed. Other than heat pipes with straight grooves, heat pipes having wick structures with converging grooves are also simulated. The motivation behind the proposal of converging grooves is to increase the capillary pumping by decreasing the feature size at the evaporator.

However, reduction of the flow area inevitably leads to an increase in viscous losses. Overall effect observed is the decrease in the maximum heat transport capacity of the heat pipe. Consequently, converging grooves is shown to be less effective than their straight counterparts (as long as the number of the grooves is preserved in the wick) as opposed to common belief in the literature.

A elementary solution to this problem is undoubtedly the decoupling of viscous losses and high capillary pressure. To this effect, a novel Hierarchical Groove Architecture (HGA) is proposed. HGA utilizes wider grooves in the transport of the liquid along condenser and adiabatic regions and narrower grooves in the evaporator. Wider grooves regularly branch to narrower grooves such that total cross sectional liquid flow area remains approximately the same. Total liquid-wall contact area, on the other hand, increases moderately due to the increase in the evaporator region. However, capillary pumping also increases considerably due to linear decrease of the feature size, thereby increasing the Laplace pressure, with the number of branching. In addition, the number of three phase contact line, where evaporation intensifies, linearly increases with the number of branching. Thus, overall effect of HGA is expected to enhance the performance of the heat pipe significantly.

The HGA is first simulated by the numerical model to demonstrate the performance enhancement. Copper-IPA heat pipes with three different groove structures are considered. Two of them have standard straight grooves and one has a HGA with branching a groove into two is the evaporation section. The results of the simulations show that although the temperature difference between the two ends of the heat pipe also increases, the maximum heat transport capacity of the heat pipe increases. The increase of temperature difference may be seen as an unfavorable outcome; yet is should be kept in mind that it occurs for a higher heat load. When both HGA and its un-branched counterpart are subjected to the heating value corresponding to the maximum capacity of the HGA, the increase in the temperature is higher in the straight grooved heat pipe compared to the heat pipe with HGA due to the pool region formation in the former. The simulated heat pipes are also manufactured and tested. Experimental results show that predictions of the numerical model match with the experiments. As

a result, HGA is demonstrated to have an enhanced performance as proposed. In other words, an electronic component that dissipates high heat flux can be cooled with smaller temperature differences by using the HGA compared to the same size standard grooved heat pipes in which the capillary pumping power is not sufficient to transport this heat load.

Branching a groove into two is shown to slightly increase the temperature difference between evaporator and condenser. The reason of this slight increase can be explained by the increase of the contact angle at the transition (branching) point, since the increase in the contact angle increases the thermal resistance of the thin film at the side groove walls. Consequently, the doubling of the contact line, i.e. the thin film region, in the case of branching of a groove into two cannot dominate the effect of increased contact angle, or thermal resistance thereof.

A set of simulation is conducted to show the decreasing effect of the proposed HGA on the temperature difference between the two ends of the heat pipe. In these simulations, the evaporator length is short to increase the heat flux, and the HGA is applied along the whole evaporator to increase the total length of the thin film evaporation regions. Simulations show that the temperature difference ratio first increases then decreases with increasing number of branches per groove. Therefore, the HGA can be used to reduce the maximum temperature that occurs at the evaporator (i.e., electronic component in reality) especially at the high heat fluxes. In other words, while using hierarchical grooves in the heat pipe, an operating temperature of the electronic component can be reduced. Thus, a component that exceeds its maximum temperature limit can be usable by decreasing its operating temperature. Alternatively, even if a component operates at a temperature lower than its maximum limit, decreasing its operation temperature with the HGA increases its reliability.

To conclude, it is incorrect to claim that there is a common optimum design point for heat pipes. Instead, heat pipes should be designed according to the needs of the system to be thermally managed. The numerical model which is developed in this thesis allows researchers/designers to simulate the heat pipes in seconds and design heat pipes according to their requirements. In addition, the HGA

proposed in the current study provides both capillary boosting and evaporation enhancement. Therefore, by using this groove architecture, higher heat loads can be transported along the heat pipe without the occurrence of dryout and pool region formation. Finally, high local temperatures can be decreased which is extremely crucial for the thermal management of high heat dissipating miniature electronic components.

To sum up, in the current thesis, a numerical model is developed and verified, then, by using the simulations of the numerical model, a modular heat pipe experimental setup is designed and manufactured. This setup is also utilized to validate the numerical model. Then the setup is used to test the performance of heat pipes with the proposed HGA. Capillary pumping boosting and evaporation enhancement capabilities of HGA are verified both numerically and experimentally.

The issues suggested for future research are listed below:

- Fourth order polynomial approximation for the liquid thickness distribution on the fin top of the grooved heat pipes leads to the overestimation of the film thickness, or thermal resistance thereof. To overcome this problem, a proper thin film condensation model should be integrated to the numerical model. In addition, the accurate calculation of film thickness throughout the heat pipe would enable the precise estimation of filling ratio via numerical model.

- In the current numerical model, the vapor temperature is assumed to be constant along the heat pipe and liquid-gas interaction is neglected; and the validity of these assumption are shown by comparing results of experiments and simulations. However, the heat pipes used in these experiments are relatively short; and these assumptions may not hold for longer heat pipes. Therefore, modeling the vapor temperature variation and liquid-gas interaction along heat pipe can be developed and added to the numerical model.

- Numerical model predicts the temperature and pressure distributions as

long as the liquid meniscus is attached to the outer surface of the wick. Following the detachment of the meniscus, accommodation flow, corner flow and dry regions may be present at the evaporator of heat pipes and these conditions directly affect the heat pipe performance. Therefore, numerical model can be improved to account for these effects.

- In this thesis, heat source and sink regions in all heat pipes simulated and experimented are defined in a way to cover all of the grooves in the heat pipe. The numerical model can be developed to simulate cases where the heat source and/or sink is smaller than the grooves.

- Evaporation enhancement by the HGA was not tested due to the limitations of machining processes. Thin grooves (approximately up to 50 μm) can be engraved on the silicon wafer by etching technology. Thus, thermal performance improvement (i.e., transporting heat input with smaller temperature difference) can be experimentally verified.

- Currently the numerical model can simulate grooved heat pipes only. However, the algorithm developed in the current study allows the simulation of sintered and meshed wick structures. Therefore, by using fluid flow and thermal resistance models valid for sintered and meshed wicks, the numerical model will be available for simulating the entire family of available grooves.

REFERENCES

[1] G. E. Moore. "Cramming more components onto integrated circuits". In: *Electronics* Apr. 1965 (38/8).

[2] B. Agostini, M. Fabbri, J. E. Park, L. Wojtan, J. R. Thome, and B. Michel. "State of the art of high heat flux cooling technologies". In: *Heat Transfer Engineering* 2007 (28/4), pages 258–281.

[3] S. S. Murshed and C. N. De Castro. "A critical review of traditional and emerging techniques and fluids for electronics cooling". In: *Renewable and Sustainable Energy Reviews* 2017 (78), pages 821–833.

[4] A. Faghri. *Heat pipe science and technology.* Global Digital Press, 1995.

[5] D. A. Reay, R. J. McGlen, and P. A. Kew. *Heat pipes: theory, design and applications.* 6th edition. Butterworth-Heinemann, 2014.

[6] G. Grover, T. Cotter, and G. Erickson. "Structures of very high thermal conductance". In: *Journal of Applied Physics* 1964 (35/6), pages 1990–1991.

[7] G. P. Peterson. *An Introduction to Heat Pipes: Modeling, Testing, and Applications.* John Wiley & Sons Inc., 1994.

[8] Faghri, A. "Heat Pipes: Review, Opportunities and Challenges". In: *Frontiers in Heat Pipes* 2014 (5/1). DOI: `http://dx.doi.org/10.5098/fhp.5.1`.

[9] S. De Schampheleire, K. De Kerpel, T. Deruyter, P. De Jaeger, and M. De Paepe. "Experimental study of small diameter fibres as wick material for capillary-driven heat pipes". In: *Applied Thermal Engineering* 2015 (78), pages 258–267.

[10] *ThermoLab Co. Ltd.* [Online]. 2009. URL: http://thermolab.co.kr/3443. (Accessed: 25.10.2020).

[11] S. Rosler, M. Groll, W. Supper, and S. Konev. "Analysis and experimental investigation of a cryogenic methane heat pipe". In: *Proceedings of the 6th International Heat Pipe Conference*. 1987, pages 219–222.

[12] J. Alario, R. Haslett, and R. Kosson. "The monogroove high performance heat pipe". In: *16th Thermophysics Conference*. 1984, page 1156.

[13] A. Faghri and S. Thomas. "Performance Characteristics of a Concentric Annular Heat Pipe: Part I—Experimental Prediction and Analysis of the Capillary Limit". In: *Journal of Heat Transfer* Nov. 1989 (111/4), pages 844–850.

[14] R. Kempers, A. Robinson, D. Ewing, and C. Ching. "Characterization of evaporator and condenser thermal resistances of a screen mesh wicked heat pipe". In: *International Journal of Heat and Mass Transfer* 2008 (51/25-26), pages 6039–6046.

[15] R. Hopkins, A. Faghri, and D. Khrustalev. "Flat Miniature Heat Pipes With Micro Capillary Grooves". In: *Journal of Heat Transfer* Feb. 1999 (121/1), pages 102–109.

[16] A. Faghri and M. Buchko. "Experimental and Numerical Analysis of Low-Temperature Heat Pipes With Multiple Heat Sources". In: *Journal of Heat Transfer* Aug. 1991 (113/3), pages 728–734.

[17] D. Plesch, W. Bier, D. Seidel, and K. Schubert. "Miniature heat pipes for heat removal from microelectronic circuits". In: *Micromechanical Sensors, Actuators and Systems* 1991 (32), pages 303–313.

[18] M. S. El-Genk and H. Lianmin. "An experimental investigation of the transient response of a water heat pipe". In: *International Journal of Heat and Mass Transfer* 1993 (36/15), pages 3823–3830.

[19]   Y. Cao, M. Gao, J. Beam, and B. Donovan. "Experiments and analyses of flat miniature heat pipes". In: *Journal of Thermophysics and heat transfer* 1997 (11/2), pages 158–164.

[20]   M. Gao, Y. Cao, J. E. Beam, and B. Donovan. "Structural optimization of axially grooved flat miniature heat pipes". In: *Journal of Enhanced Heat Transfer* 2000 (7/6).

[21]   A. Faghri, R. Stewart, and C. Rainey. "Axial variation of local heat flux along the condenser section of a double wall artery high capacity heat pipe". In: *Proceedings of the 5th International Heat Pipe Conference.* 1984, pages 13–17.

[22]   H. Jouhara and A. J. Robinson. "An experimental study of small-diameter wickless heat pipes operating in the temperature range 200 C to 450 C". In: *Heat Transfer Engineering* 2009 (30/13), pages 1041–1048.

[23]   A. Faghri, M. Buchko, and Y. Cao. "A Study of High-Temperature Heat Pipes With Multiple Heat Sources and Sinks: Part I—Experimental Methodology and Frozen Startup Profiles". In: *Journal of Heat Transfer* Nov. 1991 (113/4), pages 1003–1009.

[24]   S. Yamawaki, T. Yoshida, M. Taki, and F. Mimura. "Fundamental Heat Transfer Experiments of Heat Pipes for Turbine Cooling". In: *Journal of Engineering for Gas Turbines and Power* July 1998 (120/3), pages 580–587.

[25]   R. Ponnappan. *Studies on the startup transients and performance of a gas loaded sodium heat pipe.* Technical report. UNIVERSAL ENERGY SYSTEMS INC DAYTON OH, 1989.

[26]   A. F. Vieira da Cunha and M. B. Mantelli. "Analytical and experimental analysis of a high temperature mercury thermosyphon". In: *Journal of Heat Transfer* 2009 (131/9).

[27] W. G. Anderson and C. Tarau. "Variable conductance heat pipes for radioisotope stirling systems". In: *AIP Conference Proceedings*. Volume 969. 1. American Institute of Physics. 2008, pages 679–688.

[28] J.-M. Tournier and M. S. El-Genk. "Startup of a horizontal lithium–molybdenum heat pipe from a frozen state". In: *International Journal of Heat and Mass Transfer* 2003 (46/4), pages 671–685.

[29] Y. F. Maydanik. "Loop heat pipes". In: *Applied Thermal Engineering* 2005 (25/5-6), pages 635–657.

[30] B. Xiao and A. Faghri. "A three-dimensional thermal-fluid analysis of flat heat pipes". In: *International Journal of Heat and Mass Transfer* 2008 (51/11-12), pages 3113–3126.

[31] T. Cotter. *Principles and prospects for micro heat pipes*. Technical report. Los Alamos National Lab., NM (USA), 1984.

[32] M. Zaghdoudi, S. Maalej, J. Mansouri, and M. Sassi. "Flat miniature heat pipes for electronics cooling: State of the art, experimental and theoretical analysis". In: *International Journal of Mechanical and Mechatronics Engineering* 2011 (5/3), pages 714–737.

[33] K. Vafai and W. Wang. "Analysis of flow and heat transfer characteristics of an asymmetrical flat plate heat pipe". In: *International Journal of Heat and Mass Transfer* 1992 (35/9), pages 2087–2099.

[34] F. Lefevre and M. Lallemand. "Coupled thermal and hydrodynamic models of flat micro heat pipes for the cooling of multiple electronic components". In: *International Journal of Heat and Mass Transfer* 2006 (49/7-8), pages 1375–1383.

[35] M. Aghvami and A. Faghri. "Analysis of flat heat pipes with various heating and cooling configurations". In: *Applied Thermal Engineering* 2011 (31/14-15), pages 2645–2655.

[36] C. Ferrandi, F. Iorizzo, M. Mameli, S. Zinna, and M. Marengo. "Lumped parameter model of sintered heat pipe: Transient numerical analysis and

validation". In: *Applied Thermal Engineering* 2013 (50/1), pages 1280–1290.

[37] J. J. Kolliyil, N. Yarramsetty, and C. Balaji. "Numerical Modeling of a Wicked Heat Pipe Using Lumped Parameter Network Incorporating the Marangoni Effect". In: *Heat Transfer Engineering* 2020 (), pages 1–15.

[38] K. Vafai. "Convective flow and heat transfer in variable-porosity media". In: *Journal of Fluid Mechanics* 1984 (147), pages 233–259.

[39] N. Zhu and K. Vafai. "The effects of liquid-vapor coupling and non-Darcian transport on asymmetrical disk-shaped heat pipes". In: *International Journal of Heat and Mass Transfer* 1996 (39/10), pages 2095–2113.

[40] N. Zhu and K. Vafai. "Vapor and liquid flow in an asymmetrical flat plate heat pipe: a three-dimensional analytical and numerical investigation". In: *International Journal of Heat and Mass Transfer* 1998 (41/1), pages 159–174.

[41] N. Zhu and K. Vafai. "Analysis of cylindrical heat pipes incorporating the effects of liquid–vapor coupling and non-Darcian transport—a closed form solution". In: *International Journal of Heat and Mass Transfer* 1999 (42/18), pages 3405–3418.

[42] R. Sonan, J. Pelle, D. Leger, and M. Fakes. "Transient thermal and hydrodynamic models of a flat heat pipe for the cooling of electronic components". In: *Proceedings of CHT-08 ICHMT International Symposium on Advances in Computational Heat Transfer*. Begel House Inc. 2008.

[43] M. H. Elnaggar, M. Abdullah, and M. A. Mujeebu. "Characterization of working fluid in vertically mounted finned U-shape twin heat pipe for electronic cooling". In: *Energy Conversion and Management* 2012 (62), pages 31–39.

[44] N. Thuchayapong, A. Nakano, P. Sakulchangsatjatai, and P. Terdtoon. "Effect of capillary pressure on performance of a heat pipe: Numerical ap-

proach with FEM". In: *Applied Thermal Engineering* 2012 (32), pages 93–99.

[45] Y. Huang and Q. Chen. "A numerical model for transient simulation of porous wicked heat pipes by lattice Boltzmann method". In: *International Journal of Heat and Mass Transfer* 2017 (105), pages 270–278.

[46] A. Gholami, M. Ahmadi, and M. Bahrami. "A new analytical approach for dynamic modeling of passive multicomponent cooling systems". In: *Journal of Electronic Packaging* 2014 (136/3).

[47] D. Jafari, W. Wits, and B. Geurts. "Phase change heat transfer characteristics of an additively manufactured wick for heat pipe applications". In: *Applied Thermal Engineering* Mar. 2020 (168), page 114890. DOI: `10.1016/j.applthermaleng.2019.114890`.

[48] Y. Wang and K. Vafai. "Transient characterization of flat plate heat pipes during startup and shutdown operations". In: *International Journal of Heat and Mass Transfer* 2000 (43/15), pages 2641–2655.

[49] S. Khandekar, M. Groll, V. Luckchoura, W. Findl, and J. Zhuang. "Micro heat pipes for stacked 3D microelectronic modules". In: *International Electronic Packaging Technical Conference and Exhibition*. Volume 36908. 2003, pages 245–251.

[50] R. S. Prasher. "A Simplified Conduction Based Modeling Scheme for Design Sensitivity Study of Thermal Solution Utilizing Heat Pipe and Vapor Chamber Technology ". In: *Journal of Electronic Packaging* Sept. 2003 (125/3), pages 378–385. DOI: `10.1115/1.1602479`.

[51] L. Huang and M. S. El-Genk. "Experimental investigation of transient operation of a water heat pipe". In: *AIP Conference Proceedings*. Volume 271. 1. American Institute of Physics. 1993, pages 365–374.

[52] J.-M. Tournier and M. El-Genk. "A heat pipe transient analysis model". In: *International Journal of Heat and Mass Transfer* 1994 (37/5), pages 753–762.

[53] Z. Zuo and A. Faghri. "A network thermodynamic analysis of the heat pipe". In: *International Journal of Heat and Mass Transfer* 1998 (41/11), pages 1473–1484.

[54] B. R. Babin, G. P. Peterson, and D. Wu. "Steady-State Modeling and Testing of a Micro Heat Pipe". In: *Journal of Heat Transfer* Aug. 1990 (112/3), pages 595–601. DOI: https://doi.org/10.1115/1.2910428.

[55] S. J. Kim, J. K. Seo, and K. H. Do. "Analytical and experimental investigation on the operational characteristics and the thermal optimization of a miniature heat pipe with a grooved wick structure". In: *International Journal of Heat and Mass Transfer* 2003 (46/11), pages 2051–2063.

[56] K. H. Do, S. J. Kim, and S. V. Garimella. "A mathematical model for analyzing the thermal characteristics of a flat micro heat pipe with a grooved wick". In: *International Journal of Heat and Mass Transfer* 2008 (51/19-20), pages 4637–4650.

[57] H. Alijani, B. Çetin, Y. Akkuş, and Z. Dursunkaya. "Effect of design and operating parameters on the thermal performance of aluminum flat grooved heat pipes". In: *Applied Thermal Engineering* 2018 (132), pages 174–187.

[58] A. Anand, A. Vedamurthy, S. Chikkala, S. Kumar, D. Kumar, and P. Gupta. "Analytical and experimental investigations on axially grooved aluminum-ethane heat pipe". In: *Heat Transfer Engineering* 2008 (29/4), pages 410–416.

[59] A. N. Desai, V. Singh, and R. N. Patel. "Effect of Geometrical Parameters on the Thermal Performance of Ammonia-Based Trapezoidal-Shaped Axial Grooved Heat Pipe". In: *Journal of Heat Transfer* 2019 (141/12).

[60] G. P. Peterson and H. B. Ma. "Theoretical Analysis of the Maximum Heat Transport in Triangular Grooves: A Study of Idealized Micro Heat Pipes". In: *Journal of Heat Transfer* Aug. 1996 (118/3), pages 731–739. DOI: 10.1115/1.2822693.

[61] S. K. Thomas, R. C. Lykins, and K. L. Yerkes. "Fully developed laminar flow in trapezoidal grooves with shear stress at the liquid–vapor interface". In: *International Journal of Heat and Mass Transfer* 2001 (44/18), pages 3397–3412.

[62] S. Anand, S. De, and S. Dasgupta. "Experimental and theoretical study of axial dryout point for evaporation from V-shaped microgrooves". In: *International Journal of Heat and Mass Transfer* 2002 (45/7), pages 1535–1543.

[63] H. B. Ma and G. P. Peterson. "Experimental Investigation of the Maximum Heat Transport in Triangular Grooves". In: *Journal of Heat Transfer* Aug. 1996 (118/3), pages 740–746. DOI: 10.1115/1.2822694.

[64] R. M. Castle, S. K. Thomas, and K. L. Yerkes. "The effect of working fluid inventory on the performance of revolving helically grooved heat pipes". In: *Journal of Heat Transfer* 2001 (123/1), pages 120–129.

[65] D. Khrustalev and A. Faghri. "Thermal Analysis of a Micro Heat Pipe". In: *Journal of Heat Transfer* Feb. 1994 (116/1), pages 189–198. DOI: 10.1115/1.2910855.

[66] J. P. Longtin, B. Badran, and F. M. Gerner. "A One-Dimensional Model of a Micro Heat Pipe During Steady-State Operation". In: *Journal of Heat Transfer* Aug. 1994 (116/3), pages 709–715. DOI: 10.1115/1.2910926.

[67] S. Launay, V. Sartre, and M. Lallemand. "Hydrodynamic and thermal study of a water-filled micro-heat-pipe array". In: *Journal of Thermophysics and Heat Transfer* 2004 (18/3), pages 358–363.

[68] B. Suman, S. De, and S. DasGupta. "A model of the capillary limit of a micro heat pipe and prediction of the dry-out length". In: *International Journal of Heat and Fluid Flow* 2005 (26/3), pages 495–505.

[69] B. Suman, S. De, and S. DasGupta. "Transient modeling of micro-grooved heat pipe". In: *International Journal of Heat and Mass Transfer* 2005 (48/8), pages 1633–1646.

124

[70] Y. M. Hung and K.-K. Tio. "Analysis of microheat pipes with axial conduction in the solid wall". In: *Journal of Heat Transfer* 2010 (132/7).

[71] Y. M. Hung and K.-K. Tio. "Thermal analysis of optimally designed inclined micro heat pipes with axial solid wall conduction". In: *International Communications in Heat and Mass Transfer* 2012 (39/8), pages 1146–1153.

[72] F. L. Chang and Y. M. Hung. "The coupled effects of working fluid and solid wall on thermal performance of micro heat pipes". In: *International Journal of Heat and Mass Transfer* 2014 (73), pages 76–87.

[73] K.-K. Tio and Y. M. Hung. "Analysis of overloaded micro heat pipes: Effects of solid thermal conductivity". In: *International Journal of Heat and Mass Transfer* 2015 (81), pages 737–749.

[74] E. G. Jung and J. H. Boo. "A numerical modeling for the steady-state performance of a micro heat pipe using thin liquid film theory". In: *International Journal of Heat and Mass Transfer* 2018 (126), pages 557–566.

[75] M. Singh. "Capillarity enhancement of micro heat pipes using grooves with variable apex angle". In: *International Journal of Thermal Sciences* 2020 (150), page 106239.

[76] D. Khrustalev and A. Faghri. "Thermal Characteristics of Conventional and Flat Miniature Axially Grooved Heat Pipes". In: *Journal of Heat Transfer* Nov. 1995 (117/4), pages 1048–1054. DOI: 10.1115/1.2836280.

[77] Y. Chen, C. Zhang, M. Shi, J. Wu, and G. Peterson. "Study on flow and heat transfer characteristics of heat pipe with axial "Ω"-shaped microgrooves". In: *International Journal of Heat and Mass Transfer* 2009 (52/3-4), pages 636–643.

[78] R. Zhang. "Capillary driven thermal and hydrodynamic characteristics of axial swallow-tailed micro-grooved heat pipe". In: *Energy Sources,*

Part A: Recovery, Utilization, and Environmental Effects 2019 (41/21), pages 2573–2587.

[79] R. Rullière, F. Lefèvre, and M. Lallemand. "Prediction of the maximum heat transfer capability of two-phase heat spreaders–Experimental validation". In: *International Journal of Heat and Mass Transfer* 2007 (50/7-8), pages 1255–1262.

[80] D. Wu and G. Peterson. "Investigation of the transient characteristics of a micro heat pipe". In: *Journal of Thermophysics and Heat Transfer* 1991 (5/2), pages 129–134.

[81] S. H. Moon, G. Hwang, S. C. Ko, and Y. T. Kim. "Experimental study on the thermal performance of micro-heat pipe with cross-section of polygon". In: *Microelectronics Reliability* 2004 (44/2), pages 315–321.

[82] L. Lin, R. Ponnappan, and J. Leland. "High performance miniature heat pipe". In: *International Journal of Heat and Mass Transfer* 2002 (45/15), pages 3131–3142.

[83] F. Lefèvre, R. Rullière, G. Pandraud, and M. Lallemand. "Prediction of the temperature field in flat plate heat pipes with micro-grooves–experimental validation". In: *International Journal of Heat and Mass Transfer* 2008 (51/15-16), pages 4083–4094.

[84] S. Lips, F. Lefèvre, and J. Bonjour. "Physical mechanisms involved in grooved flat heat pipes: experimental and numerical analyses". In: *International Journal of Thermal Sciences* 2011 (50/7), pages 1243–1252.

[85] W. W. Wits and G. J. te Riele. "Modelling and performance of heat pipes with long evaporator sections". In: *Heat and Mass Transfer* 2017 (53/11), pages 3341–3351.

[86] S. W. Chi. *Heat pipe theory and practice : a sourcebook*. Hemisphere Pub. Corp, 1976.

[87] W.-Z. Fang, Y.-Q. Tang, C. Yang, and W.-Q. Tao. "Numerical simulations of the liquid-vapor phase change dynamic processes in a flat micro

heat pipe". In: *International Journal of Heat and Mass Transfer* 2020 (147), page 119022.

[88] Y. Cao, J. Beam, and B. Donovan. "Air-cooling system for metal oxide semiconductor controlled thyristors employing miniature heat pipes". In: *Journal of Thermophysics and Heat Transfer* 1996 (10/3), pages 484–489.

[89] G. P. Peterson, A. B. Duncan, and M. H. Weichold. "Experimental Investigation of Micro Heat Pipes Fabricated in Silicon Wafers". In: *Journal of Heat Transfer* Aug. 1993 (115/3), pages 751–756. DOI: 10.1115/1.2910747.

[90] B. Badran, F. M. Gerner, P. Ramadas, T. Henderson, and K. W. Baker. "Experimental results for low-temperature silicon micromachined micro heat pipe arrays using water and methanol as working fluids". In: *Experimental Heat Transfer* 1997 (10/4), pages 253–272. DOI: 10.1080/08916159708946547.

[91] J.-S. Chen and J.-H. Chou. "Cooling performance of flat plate heat pipes with different liquid filling ratios". In: *International Journal of Heat and Mass Transfer* 2014 (77), pages 874–882.

[92] G. Wang, Z. Quan, Y. Zhao, and H. Wang. "Performance of a flat-plate micro heat pipe at different filling ratios and working fluids". In: *Applied Thermal Engineering* 2019 (146), pages 459–468.

[93] H. Lim, S. Kim, H. Im, K. H. Oh, and S. Jeong. "Fabrication and evaluation of a copper flat micro heat pipe working under adverse-gravity orientation". In: *Journal of Micromechanics and Microengineering* 2008 (18/10), page 105013.

[94] S. Lips, F. Lefèvre, and J. Bonjour. "Nucleate boiling in a flat grooved heat pipe". In: *International Journal of Thermal Sciences* 2009 (48/7), pages 1273–1278.

[95] J.-S. Chen and J.-H. Chou. "The length and bending angle effects on the cooling performance of flat plate heat pipes". In: *International Journal of Heat and Mass Transfer* 2015 (90), pages 848–856.

[96] Y. Wang and K. Vafai. "An experimental investigation of the transient characteristics on a flat-plate heat pipe during startup and shutdown operations". In: *Journal of Heat Transfer* 2000 (122/3), pages 525–535.

[97] P. Mistry, F. Thakkar, S. De, and S. DasGupta. "Experimental validation of a two-dimensional model of the transient and steady-state characteristics of a wicked heat pipe". In: *Experimental Heat Transfer* 2010 (23/4), pages 333–348.

[98] W. W. Wits and J. B. Kok. "Modeling and validating the transient behavior of flat miniature heat pipes manufactured in multilayer printed circuit board technology". In: *Journal of heat transfer* 2011 (133/8).

[99] G. Odabasi. "Modeling of multidimensional heat transfer in a rectangular grooved heat pipe". In: *Ph.D. Thesis, Middle East Technical University* 2014 ().

[100] Y. Akkuş and Z. Dursunkaya. "A new approach to thin film evaporation modeling". In: *International Journal of Heat and Mass Transfer* 2016 (101), pages 742–748.

[101] M. Sujanani and P. C. Wayner Jr. "Microcomputer-enhanced optical investigation of transport processes with phase change in near-equilibrium thin liquid films". In: *Journal of Colloid and Interface Science* 1991 (143/2), pages 472–488.

[102] F. Lefèvre, R. Rullière, S. Lips, and J. Bonjour. "Confocal microscopy for capillary film measurements in a flat plate heat pipe". In: *Journal of heat transfer* 2010 (132/3).

CURRICULUM VITAE

PERSONAL INFORMATION

Surname, Name: Saygan, Samet

Nationality: Turkish (TC)

Date and Place of Birth: 1988, Bursa

Marital Status: Married

Email sametsaygan@gmail.com

EDUCATION

Degree	Institution	Year of Graduation
M.Sc.	METU Mechanical Engineering	2014
B.Sc.	METU Mechanical Engineering	2011
High School	T.C. Ziraat Bankası Balıkesir Science High School	2006

PROFESSIONAL EXPERIENCE

Year	Place	Enrollment
2010-Present	ASELSAN Inc., Ankara	Senior Engineer